AN ABSTRACT OF THE THESIS OF

Yeon-Chang Hahm for the degree of Doctor of Philosophy in Electrical and Computer Engineering presented on January 27, 2000. Title: Field Theoretic Analysis of a Class of Planar Microwave and Opto-Electronic Structures.

Abstract approved: Redacted for Privacy

Vijai K. Tripathi

Redacted for Privacy

Andreas Weisshaar

With increasing operating frequencies in CMOS RF/microwave integrated circuits, the performance of on-chip interconnects is becoming significantly affected by the lossy substrate. It is the purpose of the first part of this thesis to develop a rigorous field theoretic analysis approach for efficient characterization of single and multiple coupled interconnects on silicon substrate, which is applicable over a wide range of substrate resistivities. The frequency-dependent transmission line parameters of a microstrip on silicon are determined by a new formulation based on a quasi-electrostatic and quasi-magnetostatic spectral domain approach. It is demonstrated that this new quasi-static formulation provides the complete frequency-dependent interconnect characteristics for all three major transmission line modes of operation. In particular, it is shown that in the case of heavily doped CMOS substrates, the distributed series inductance and series resistance parameters are significantly affected by the presence of longitudinal substrate currents giving rise to the substrate skin-effect. The method is further extended to multiple coupled single and multi-level interconnect structures with ground plane and multiple coupled co-planar stripline structures without ground plane. The finite conductor thickness is taken into account in terms of a stacked conductor model. The new quasi-static approach is validated by comparison with results obtained with a full-wave spectral

domain method and the commercial planar full-wave electromagnetic field solver HP/Momentum®, as well as published simulation and measurement data.

In the second part of this thesis, coupled planar optical interconnect structures are investigated based on a rigorous field theoretic analysis combined with an application of the normal mode theory for coupled transmission lines. A new transfer matrix description for a general optical directional coupler is presented. Based on this transfer matrix formulation, the wavelength-dependent characteristics of multi-section optical filters consisting of cascaded asymmetric optical directional coupler sections are investigated. It is shown that by varying the asymmetry factors of the cascaded coupled waveguide sections, optical wavelength filters with different passband properties can be achieved.

Field Theoretic Analysis of a Class of Planar Microwave and Opto-Electronic Structures

by

Yeon-Chang Hahm

A THESIS

submitted to

Oregon State University

in partial fulfillment of
the requirements for the
degree of

Doctor of Philosophy

Presented January 27, 2000
Commencement June 2000

Doctor of Philosophy thesis of Yeon-Chang Hahm presented on January 27, 2000

APPROVED:

Redacted for Privacy

Co-Major Professor, representing Electrical and Computer Engineering

Redacted for Privacy

Co-Major Professor, representing Electrical and Computer Engineering

Redacted for Privacy

Head of Department of Electrical and Computer Engineering

Redacted for Privacy

Dean of Graduate School

I understand that my thesis will become part of the permanent collection of Oregon State University libraries. My signature below authorizes release of my thesis to any reader upon request.

Redacted for Privacy

Yeon-Chang Hahm, Author

ACKNOWLEDGMENTS

The completion of this thesis was possible by numerous persons with their incessant guidance, encouragement, and discussion. First of all, I am profoundly grateful to my major professors, V.K. Tripathi and A. Weisshaar. They shared a great deal of their precious time and ideas during the researches, and contributed to the fulfillment of my Ph.D program at Oregon State University. Also, they guided me not only as scholars, but also as seniors of life. In addition, they provided me financial supports via the research funds from HP Eesof, and NSF/CDADIC.

I am also grateful to the professors in my committee members, Dr. T.K. Plant, Dr. R.K. Settaluri, Dr. B. Lee, Dr. U. Moon, and Dr. Solomon Yim, for their time and advice. Also, special thanks are given to J. Zheng, C. Lim, K. Remley, A. Tripathi, R. Lutz, and other colleagues in Microwave and Optics group, who have shared precious idea and time during the numerous discussions.

In addition, I sincerely thank to my wife, So-Yeon, and two daughters, Stephanie and Jasmine, for their continuous devotions during the school years. Especially, I am profoundly grateful to my parents in Korea who have supported me with their all possible ways for the time being.

TABLE OF CONTENTS

TABLE OF CONTENTS (Continued)

LIST OF FIGURES

LIST OF FIGURES (continued)

LIST OF FIGURES (continued)

LIST OF FIGURES (continued)

LIST OF FIGURES (continued)

LIST OF APPENDICES

FIELD THEORETIC ANALYSIS OF A CLASS OF PLANAR MICROWAVE AND OPTO-ELECTRONIC STRUCTURES

1 INTRODUCTION

1.1 General Background of Metallic and Dielectric Interconnects

Semiconductor integrated circuit technologies play a critical role in most of today's high-speed MMIC, VLSI and RFIC systems. Since the invention of the first bipolar junction transistor (BJT) in the 1960's, a great deal of work has been carried out to achieve cost-effective and fast-speed semiconductor integrated circuit systems with stable performance [1,2]. For the faster-speed applications of today, new IC technologies have been developed yielding a faster time response with lower bias voltage and higher integration density. Thus, the latest typical commercial CPUs are composed of more than 10 million transistors, and the operating core clock speed already has reached the 1 [GHz] range. It has been predicted that by the year 2005, most of the CPU's will be featuring a 3 [GHz] clock speed with integration of more than 100 million transistors. [3]

With increasing clock speeds and integration densities, the interconnections between components and devices also play an increasingly important role in the entire circuit performance. Today's various types of metallic on- and off-chip interconnects illustrated in Figure 1.1 have become a major bottleneck in the performance of high-speed digital ICs [3,33,34]. In general, interconnects can lead to significant signal delay and noise through crosstalk as well as power dissipation in the metallization and lossy substrate.

Most high-speed passive and active devices are constructed by various shapes of planar transmission line structures as a whole or parts of the components. These planar transmission lines such as strip lines and microstrip lines with or without ground plane are the most important configurations in VLSI, RFIC and mixed signal applications.

Thus, it is desirable to characterize planar interconnects using accurate modeling techniques, which in addition to the distributed resistance, capacitance and inductance associated with the interconnect, include the capacitive and inductive coupling effects between the lines.

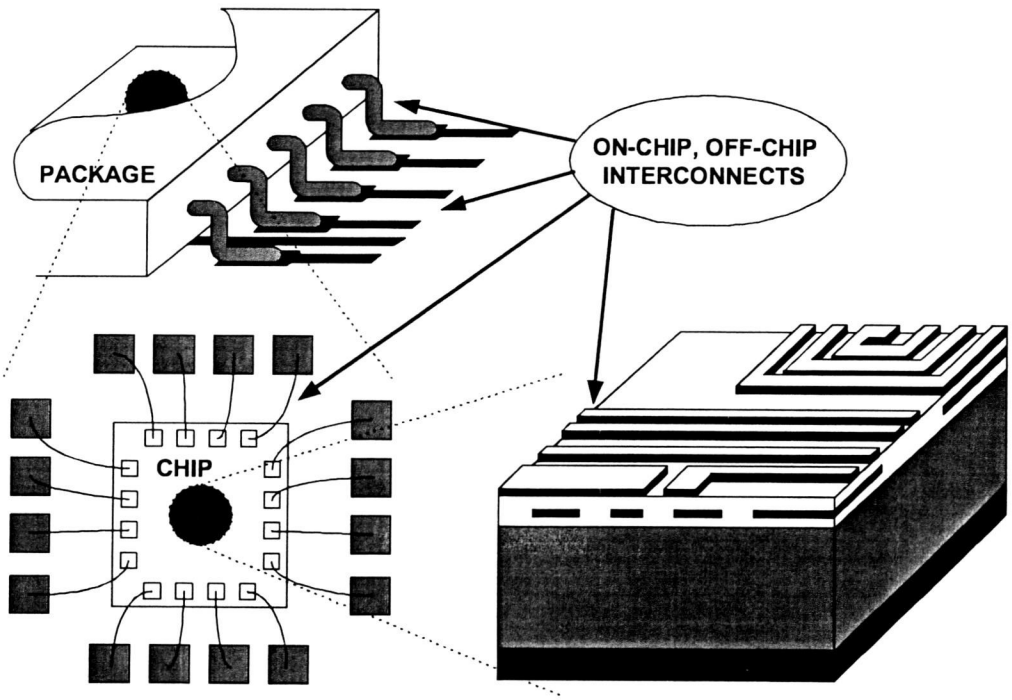

Figure 1.1 Typical microwave planar transmission lines and passive components

In general, planar transmission lines are realized in inhomogeneous media, and no simple closed form equations characterizing such structures are available. Particularly, the characterization becomes even more complicated when lossy substrate media such as doped semiconductors in integrated circuit structures are present since the effect of the lossy substrate layers at high operating frequencies need to be appropriately included in the modeling procedures. In heavily doped substrate materials such as in typical CMOS processes, substrate losses can be very important and significantly influence the performance of integrated circuits.

In order to characterize the frequency- and conductivity-dependent properties of interconnects on semiconductor substrates, various types of methodologies have been developed [4~12]. In general, the modeling techniques are based on analyzing the field distributions by solving the wave equation subject to given boundary conditions. Various 3D/2D full-wave microwave modeling techniques such as the Method of Moment (MoM), Finite Element Method (FEM), Finite Difference Time Domain Method (FDTD) and full-wave Spectral Domain Methods are known as appropriate strategies for analyzing microwave passives [5]. In particular, it is recommended to use these methods when accurate frequency-dependent characterization of structures on lossy silicon substrates is needed, even though full-wave methods typically lead to long computation times. As a 2D electromagnetic solver, the full-wave spectral domain method is a very suitable technique for planar stripline-like on-chip or off-chip interconnects [5~7]. The full-wave spectral domain method is able to yield fundamental and higher order mode eigen-solutions, and is capable of calculating the corresponding dispersion characteristics.

On the other hand, the complexity and computation time of the characterization procedure can be drastically reduced if the solution to the Laplace equation can adequately approximate the properties of the structures in the frequency range of operation. These approaches, categorized as electric potential-based quasi-static methods, include various techniques such as the Finite Difference Method (FDM), the Transverse Resonant Technique, and the quasi-static Spectral Domain Method (SDM), etc. [5]. Among the quasi-static approaches, the quasi-static SDM is especially well suited for analyzing planar transmission line structures [11~17].

Although conventional electric potential-based quasi-static approaches typically are significantly faster than full-wave methods, they are, in general, not suitable for analyzing high frequency and high speed interconnects on lossy silicon substrates due to the frequency-dependent effects of the lossy semi-conducting substrate. It is one of the goals of this dissertation to develop a new efficient quasi-static electromagnetic approach for analyzing high frequency and high-speed on-chip interconnects on lossy silicon substrates.

In recent years, optical on-chip interconnects have been proposed to overcome some of the drawbacks of the conventional electrical interconnects. Optical Interconnects have the potential to provide shorter signal delays, higher signal bandwidth, reduced power loss, and to occupy less chip area [34]. Today's integrated optic technology used in modern communication systems and signal processing takes advantage of these properties of optical waveguides, as well as improved performances of optical fibers and semiconductor lasers [32~36].

In general, optical interconnects include signal conversion interfaces (i.e., O-E and E-O), and waveguide structures, which might be glass fiber or dielectric waveguide, or free space structures. The typical optical waveguide configuration consists of core (guiding) and cladding materials, as illustrated in Figure 1.2. Especially, planar (slab) and rectangular (e.g., rib) dielectric waveguides are the most common components used in modern opto-electronic and optical integrated circuits such as semiconductor lasers, optical power dividers and combiners, and optical modulators, switches and filters, etc.

Over the years, numerous computation techniques have been developed to determine the modal characteristics of optical waveguides [e.g., 34,35]. Specifically, for slab waveguides the Matrix Method for step index profiles and the Impedance Boundary Method of Moments for arbitrary index profiles [38,39] enable efficient and accurate computation of the slab waveguide modes. If the structure involves more than one core region (i.e., consists of two or more waveguides), the propagating mechanism of lightwaves becomes more complicated due to the mutual interactions.

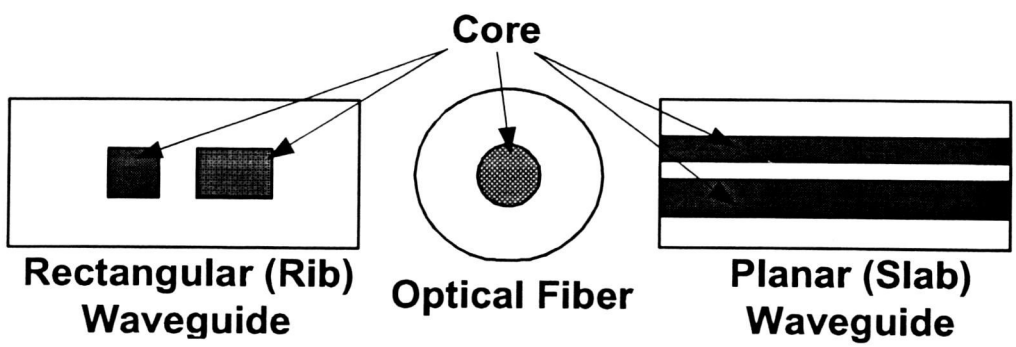

Figure 1.2 Typical optical waveguide configurations

Hence, coupled mode theory and normal mode theory [14,15,36,40] are widely used to analyze the relations between input and output lightwaves of the structure.

As one of the fundamental interconnect components used in integrated optics, the optical directional coupler plays an important role in linking two separate optical paths. Optical couplers are also used as basic building blocks for optical wavelength [69] and frequency filters [56]. The typical configuration of these filters consists of cascaded couplers and uncoupled connecting waveguide sections of unequal lengths, which together form cascaded Mach-Zehnder interferometers. This configuration can be realized in optical integrated circuits with rectangular waveguide interconnects and waveguide bends, resulting in an increase in occupied chip area. On the other hand, no simple solution for implementing the uncoupled connecting waveguide sections of unequal length with planar (slab) waveguides is available.

In this thesis, an alternate approach for realizing an optical filter without the use of waveguide bends is proposed. In this approach, sections of asymmetric coupled waveguides with various degrees of asymmetry are cascaded. The new configurations can be directly implemented with rectangular or slab waveguides.

1.2 Organization of the Study

Metallic planar transmission line structures on semiconductor and optical dielectric waveguide couplers are the main focus of this thesis. An overview of the research and background is given in this chapter.

Chapters 2~5 investigate various types of metallic planar transmission lines fabricated on silicon substrate. In the second chapter, previous modeling techniques for microstrip transmission lines fabricated on semiconductor substrate are briefly introduced. In the first two sections, the general transmission line characteristics in terms of semiconductor conductivity and frequency are investigated by a parallel plate waveguide model as well as by a full-wave 2D spectral domain method. Also, the conventional quasi-static SDM is described in the following section, showing its invalidity for the characterization of typical interconnects in current CMOS technology with increasing frequency-range of operation.

Chapter 3 introduces a new quasi-static spectral domain approach, which is valid for interconnects used in CMOS technology. In this new approach, the shunt capacitance and shunt conductance of the interconnect are determined with the conventional quasi-static SDM based on the electric potential. The interconnect's frequency-dependent distributed series inductance and series resistance representing substrate loss are determined with a new magnetic-potential based quasi-static SDM. The combined solutions are compared with full-wave solutions in order to show the validity and accuracy of the proposed method.

In chapter 4, various multi-conductor interconnect structures with bottom ground plane are investigated using the new quasi-static approach. These include single level as well as multilevel, multiple coupled line configurations. The quasi-static simulation results are compared with full-wave solutions. In addition, this chapter introduces a technique to include the effects of finite conductor thickness in the interconnect model.

In chapter 5, planar interconnects without bottom ground plane are studied using a new Green's function. These structures are used in particular in VLSI integrated circuits where ground lines are located in the interconnect layers together with the signal lines. For accurate analysis of these structures, the conventional Green's function, which is systematically unstable, is replaced by a new stable Green's function. In addition, an inductance matrix reduction methodology is presented. To validate the approach, coplanar stripline and coplanar waveguide structures are investigated, and results are compared with published simulated and measured data.

In chapter 6, general cascaded asymmetric coupled optical interconnect structures are studied. A new closed-form transfer matrix approach is described to analyze the power transfer in this general coupled interconnect structure. Using the new transfer matrix formulation, the feasibility of optical wavelength filter based on cascaded sections of symmetric and asymmetric coupled waveguide (interconnect) sections is demonstrated.

In the last chapter, final conclusions of this research work are presented together with suggestions for future work.

2 MICROSTRIP TRANSMISSION LINES ON SEMICONDUCTOR

2.1 Introduction

Planar transmission lines are an integral part of integrated circuits in form of interconnections as well as components such as spiral inductors and matching networks. With the increasing interest in recent years in silicon-based integrated circuits for RF/microwave applications at several GHz and the rapidly increasing operating speeds of high performance digital integrated circuits, the effect of the lossy silicon substrate (especially in CMOS technology) on the interconnect performance is becoming more and more important.

Over many years, transmission lines on lossless and on low loss substrates, such as Alumina and Si-GaAs, have been characterized using a variety of quasi-static and full-wave electromagnetic techniques. In 1971, Hasegawa studied the influence of silicon semiconducting substrate on the transmission line characteristics over a wide range of silicon conductivities using a simple parallel-plate model and experimental data [4]. Even though this article provided for the first time the main concepts of the three major operating modes for these types of metal-insulator-semiconductor (MIS) structures, the parallel-plate model was shown to be appropriate for only wide conducting strips as compared to substrate height. In general, more rigorous modeling approaches are needed for narrower conducting strips. More recently, MIS structures have been characterized using a full-wave spectral-domain approach (SDA) [12,64,65,66]. The full-wave SDA introduced by Mittra and others in the early 1970's is recognized as a powerful and accurate method for analyzing microstrip-like planar transmission line structures [5-10]. In general, however, full-wave methods, including full-wave SDA, require substantially longer computation times as compared with quasi-static solutions. More recently, the broad-band transmission line behavior of single MIS configurations has been characterized by a more efficient quasi-TEM space domain approach [71] as well as in

terms of approximate closed-form expressions for the frequency-dependent transmission line parameters [72,73].

The focus of this chapter is, first, to describe the three main operating modes of MIS structures based on full-wave solutions, and second, to discuss the short-comings of conventional quasi-static approaches for analyzing MIS structures, especially for high substrate conductivities at high frequencies such as RF/microwave interconnects on CMOS substrate. Following this chapter, a new quasi-static spectral domain approach for a large class of single and multiple coupled MIS interconnects, having the accuracy of full-wave methods, is described.

2.2 MIS(Metal-Insulator-Semiconductor) Structures

According to Hasegawa's studies [4], the interactions of the electromagnetic fields with the lossy substrate can be categorized by three major modes of operation, i.e., quasi-TEM, slow-wave and skin-effect mode, as illustrated in the frequency-conductivity diagram in Figure 2.1. Since each mode has a complicated wave propagation mechanism, it is helpful to consider the physical behavior of the corresponding modes in terms of the distributed shunt and series transmission line parameters as a function of frequency and σ_{Si}.

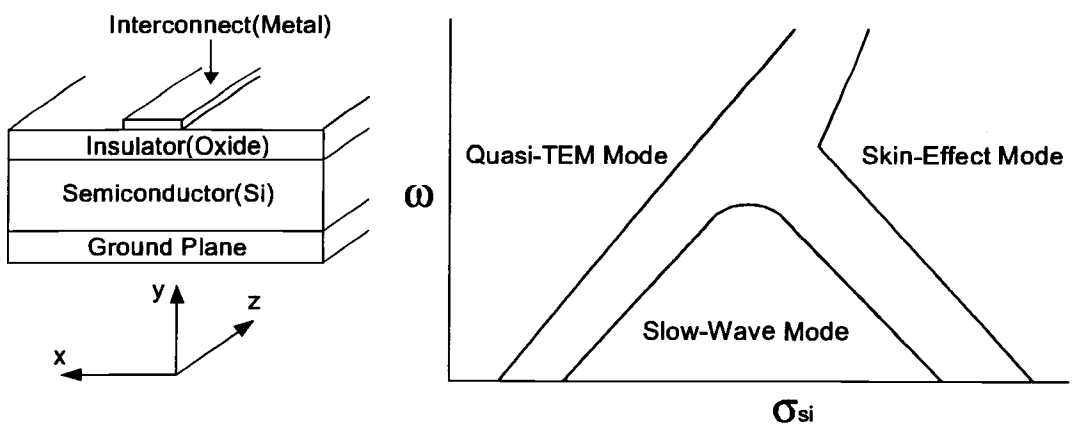

Figure 2.1 MIS structure and the three major operating modes [4]

The quasi-TEM mode is defined as the region for which the frequency-conductivity product ($\omega\sigma_{Si}$) stays in the low range. In this mode, the substrate media can be simply treated as a single silicon layer since the physical height of Si and its dielectric constant are relatively greater than the thickness of the insulator (oxide) layer. Also, the physical height of the substrate media is much smaller than the wavelength. Thus, most of the field is concentrated in the Si layer, and the fundamental operation is very similar to a TEM mode for which the static wave equation is adequately applicable with acceptable accuracy.

On the contrary, only a small amount of field exists in the Si layer with a small penetration depth when $\omega\sigma_{Si}$ reaches very high values. In this operation, called skin-effect mode, the silicon layer can be treated as a lossy ground plane. In addition, most of the waves are propagating in the oxide layer due to wave reflection at the silicon layer. Consequently, the wave propagating mechanism is dominated by the interactions between the lossy penetration depth in the silicon layer and the conducting strip separated by the oxide layer.

If $\omega\sigma_{Si}$ stays in the intermediate range, the behavior of the silicon layer is between that of a lossy conductor and a lossless dielectric (i.e., semiconductor). This operating condition yields a slow wave propagation velocity due to dielectric dispersion associated with strong interfacial polarization at the silicon substrate, as described by Hasegawa. Hence, it is called Slow-wave mode.

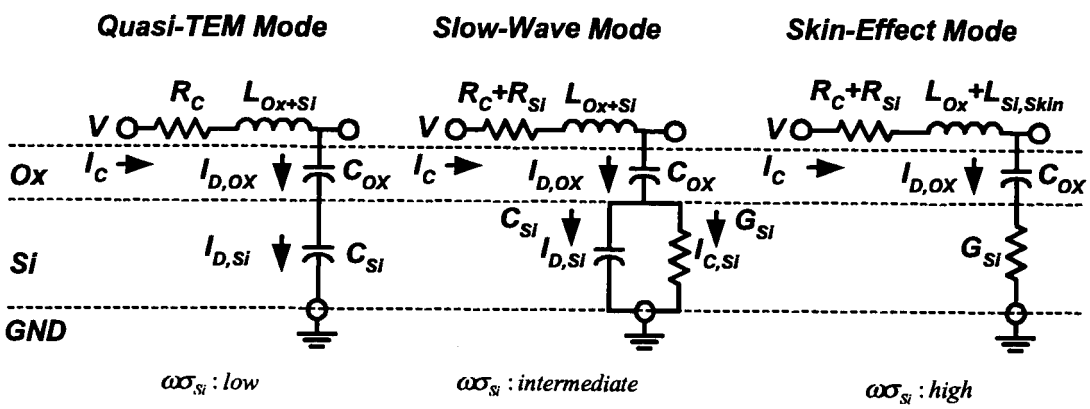

Figure 2.2 Equivalent circuit for MIS structure

The three different mode regions can be qualitatively represented and explained in terms of the equivalent circuits for a short section of an MIS structure, as shown in Fig. 2.2. In the quasi-TEM mode, σ_{Si} is small compared to $\omega\varepsilon_{Si}$ and, hence, the shunt conduction current in the silicon substrate is negligible compared to the shunt displacement current. The series inductance L_{Ox+Si} corresponds to the flux linkage between the strip and the ground plane through the oxide and silicon substrate, and the series resistance R_C represents the conductor loss in the strip. In the slow-wave mode, the shunt conduction current in the silicon substrate becomes significant and is represented in terms of the shunt conductance G_{Si}. Furthermore, due to the penetration of the magnetic flux in the lossy silicon substrate, additional energy is dissipated by the non-negligible longitudinal substrate current, which is represented as additional series resistance term R_{Si}. Finally, in the skin-effect mode for high substrate conductivities, the magnetic field penetration into the silicon substrate is significantly reduced (substrate skin effect). This leads to smaller series inductance reduced to a value corresponding to the flux linkage in the thin oxide layer and penetration depth into the silicon substrate.

2.3 Consideration of MIS via Full-wave Spectral Domain Approach

In this section, the different mode characteristics of MIS structures are illustrated in more detail using a full-wave spectral domain method. This method calculates the p.u.l line parameters by obtaining the eigenmode solutions to the wave equation for the **E** and **H** fields subject to the boundary conditions. The tangential current distributions on the conductor representing **H**, and the corresponding **E** field are computed by the well-known Galerkin's procedure. In general, a root-seeking procedure is applied to calculate the non-trivial eigen-solutions of the linear equation, and a corresponding unknown coefficient vector of the basis functions can be obtained. Once the tangential current components are obtained, the **E** and **H** fields and corresponding characteristic impedance are readily calculated using various numerical analysis approaches. The detailed procedure is described in the literature [5~9] and summarized in Appendix 6.

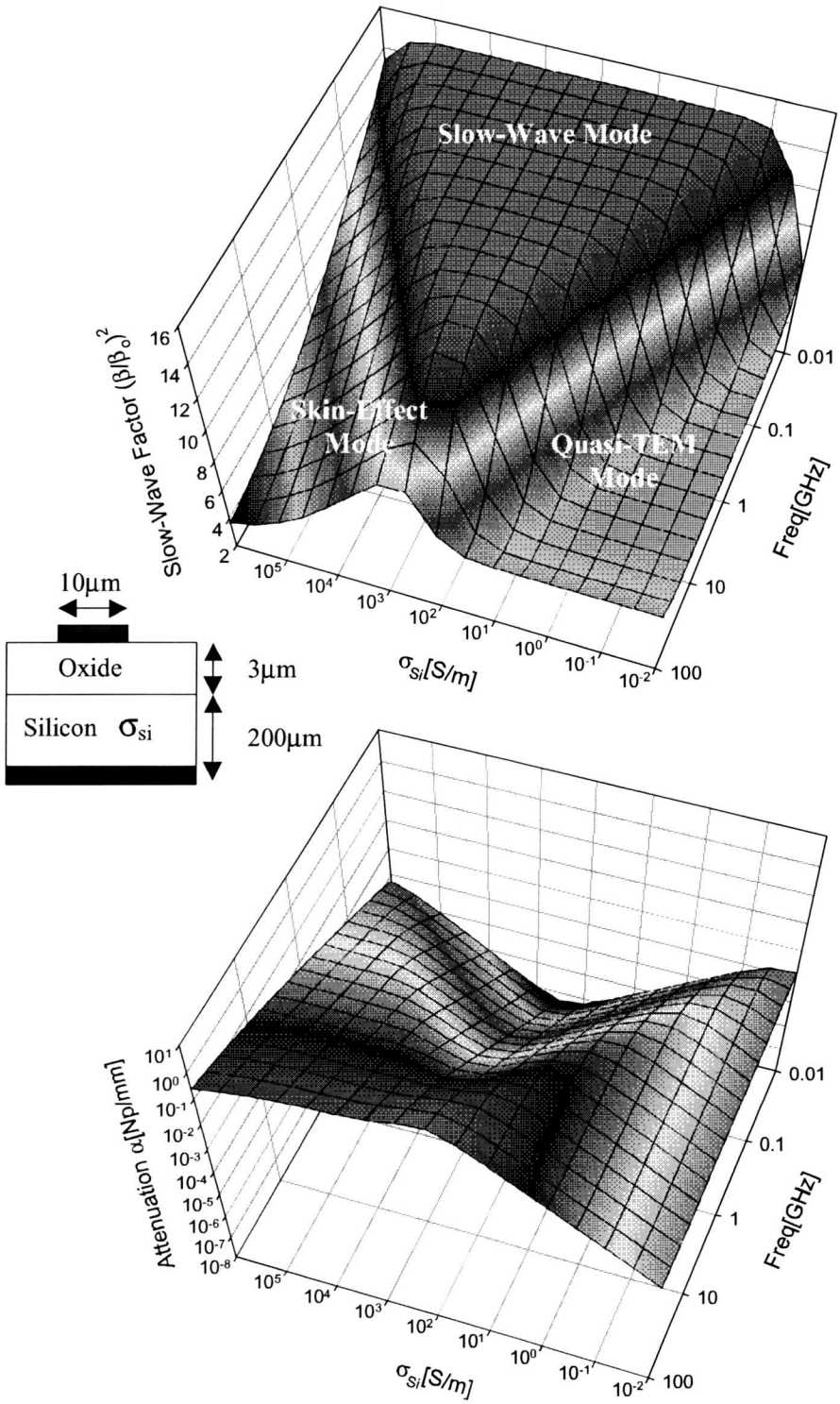

Figure 2.3 Slow-wave factor and attenuation in MIS generated by full-wave SDM.

By aid of this comprehensive approach, the transmission characteristics of a typical MIS structure are shown in Figure 2.3. As seen in the figure the three major modes as a function of frequency and semiconductor conductivity are clearly visible. If the frequency increases for a given a conductivity, the attenuation increases and the propagating speed changes abruptly. Thus, this phenomenon could result in distortion of the waveform if the operating frequency band in an analog system is not carefully chosen. Moreover, the characteristic impedance is another characteristic affected by the operating condition. The characteristic impedance has significant changes not only in the real part, but also in the imaginary part. Therefore, the next stage of a circuit can be seriously influenced by impedance mismatch.

Using the full-wave SDM, MIS structures can be successfully characterized as demonstrated in the Figure 2.3. This method, however, has some drawbacks in the calculating procedures. First, finding the appropriate line parameters may be difficult due to the coexistence of many non-trivial eigen-solutions representing higher order modes together with multiple fundamental modes if the structure consists of multiple coupled interconnects. Second, the full-wave method consumes a long computation time and large computing resources. In particular, all the calculations are to be done in complex domain without knowing approximate ranges of anticipated solutions for lossy semiconductor materials. Third, additional procedures are still needed in order to take into account other physical parameters such as attenuation due to the conductor and conductor thickness effects.

2.4 Conventional Quasi-TEM Characterization

In general, using the quasi-TEM approach, the fundamental line mode parameters are obtained by calculating the eigen-solutions to the characteristic linear equation formed by the frequency-dependent equivalent shunt and series lumped components, p.u.l. $C_{eq}(\omega)$, $L_{eq}(\omega)$. The distributed series inductance, and resistance and shunt capacitance and conductance are given in the form of

$$C_{eq}(\omega) = C(\omega) - j\frac{G(\omega)}{\omega} \tag{2.1}$$

$$L_{eq}(\omega) = L(\omega) - j\frac{R(\omega)}{\omega} \tag{2.2}$$

The frequency-dependent shunt admittance component, $C_{eq}(\omega)$, is accurately estimated by applying a known potential to the conductors, and calculating the total electric charges accumulated on the conductors for example with Galerkin's method as a modified form of the Rayleigh-Ritz method [11~12]. The detailed procedure for this approach is described in the next chapter.

Under the quasi-TEM approximation, the series inductance, $L(\omega)$, can be conveniently determined from the distributed capacitance of the structure, C_{air}, if all dielectric materials are removed. In this case, the velocity of propagation is given by

$$c_o = \frac{1}{\sqrt{\mu_o \varepsilon_o}} = \frac{1}{\sqrt{L_{air} \cdot C_{air}}} \tag{2.3}$$

If the dielectric material that was removed has small loss, the inductance, L_{air}, is approximately the same as L of the actual structure. Thus, L is determined as

$$L = L_{air} = \frac{\mu_o \varepsilon_o}{C_{air}} \tag{2.4}$$

for a single line, and

$$[L] = \mu_o \varepsilon_o [C_{air}]^{-1} \tag{2.5}$$

for coupled lines.

This simple approach is quite accurate even for substrates with intermediate range of conductivity (i.e., quasi-TEM and/or slow-wave mode of operations [12]). By using this approach, an exemplary MIS structure is analyzed, and results are shown in Figure 2.4 as a function of conductivity. As seen in the figure, it is clear that the conventional

quasi-TEM is appropriate only when the operating mode is restricted in quasi-TEM or to slightly lossy cases.

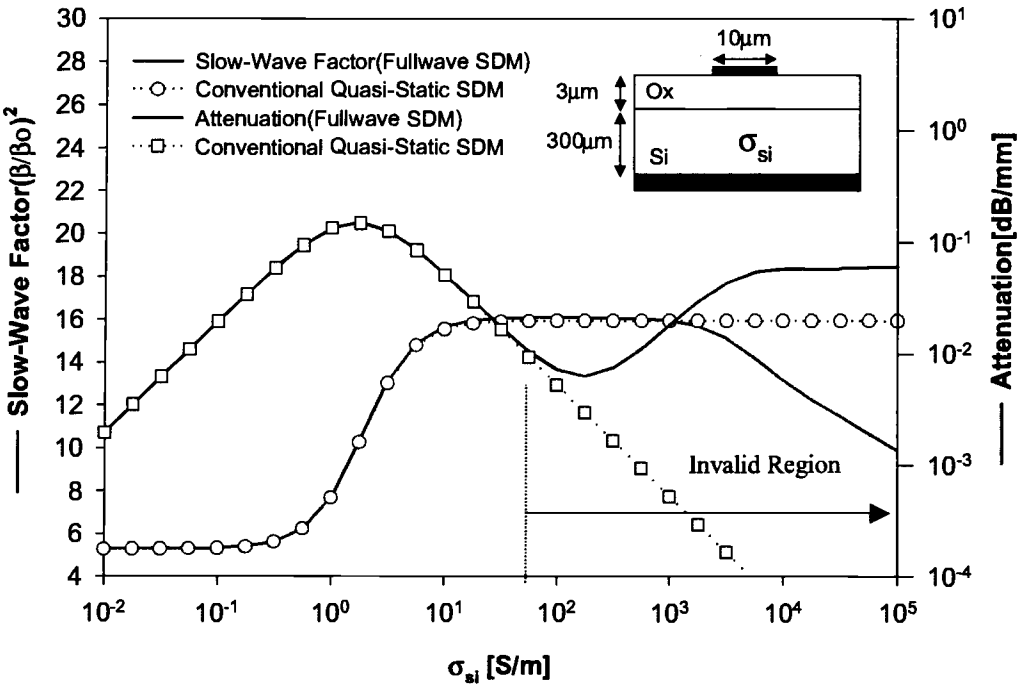

Figure 2.4 Invalidity of the conventional electric potential-based quasi-TEM SDM

This result is obvious considering that the equivalent inductance obtained by the conventional approach is always a constant regardless of the operating frequency and substrate conductivity. However, the equivalent transmission line parameters including inductance representing the physical behavior of semiconductor substrate change both in terms of frequency and silicon conductivity as explained in the previous section.

If frequency or conductivity increases in the slow-wave mode region, the operation condition enters the skin-effect mode with a faster propagation velocity and increased attenuation. In this mode region, the line parameters can not be correctly determined by the conventional quasi-TEM approach. Moreover, the region where the conventional

quasi-TEM approach becomes invalid already starts at about the middle of the slow-wave mode region, considering the change in attenuation.

2.5 Conclusion

In order to accurately characterize planar transmission lines on semiconductor substrate using the quasi-static approach, it is necessary to obtain correct frequency-dependent distributed circuit elements, $L(\omega)$, $R(\omega)$, $C(\omega)$, $G(\omega)$. The conventional quasi-TEM approximation, however, only provides a constant (static) value for the series inductance $L(\omega)$ and ignores any contributions to $R(\omega)$ due to longitudinal substrate currents. In general, rigorous full-wave approaches should be applied, and one should face the potential problems explained in the section 2.3. As an alternative to full-wave methods, the series impedance components can be calculated in a more rigorous and theory-based approach, that is, a quasi magnetostatic approach for determining the equivalent inductance, $L_{eq}(\omega)$ (i.e., $L_{eq}(\omega)=L(\omega)+R(\omega)/j\omega$). In the next chapter, a new method to extract correct values of line parameters using a magnetic-vector-potential-based spectral domain method is introduced.

3 CHARACTERIZATION OF MICROSTRIP ON SEMICONDUCTOR BY A NEW QUASI-STATIC SPECTRAL DOMAIN APPROACH

3.1 Introduction

Figure 3.1a illustrates a general microstrip on a lossy substrate. The propagation characteristics of this transmission line can be accurately described in terms of the distributed *R, L, G, C* transmission line parameters (Fig. 3.1b). Since the substrate is lossy, both shunt and series parameters are frequency-dependent, as was briefly discussed in the previous chapter. In general, the full-wave problem must be solved to accurately obtain the frequency-dependent propagation characteristics of this structure. On the other hand, quasi-static techniques typically are preferred because they are computationally much more efficient compared to full-wave techniques. For frequencies of up to at least several [GHz], the shunt capacitance and shunt conductance (or, complex capacitance) can be accurately obtained by solving the corresponding quasi-electrostatic problem. However, the conventional quasi-TEM approach for determining the series inductance fails for large substrate conductivities, as shown in the previous chapter.

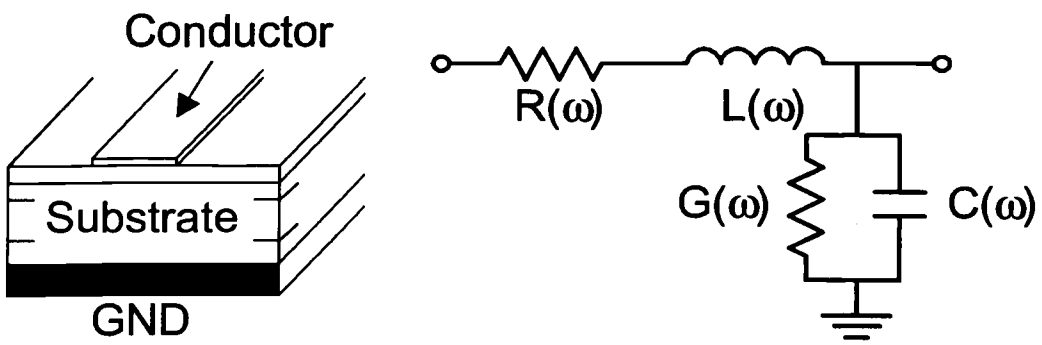

Figure 3.1 Equivalent circuit for microstrip transmission line on Si-SiO_2

In this chapter, a new comprehensive quasi-static spectral domain approach for determining the complete transmission line parameters is described. A new quasi-magnetostatic formulation in terms of the vector magnetic potential is given to determine the frequency-dependent series inductance and conductance. The quasi-electrostatic and quasi-magnetostatic problems are efficiently solved in the spectral domain. Only a single line structure is considered in this chapter in order to focus more on the mathematical description of the two quasi-static spectral domain approaches as well as conceptual explanations. In the following chapters, more complicated multiple coupled line structures are investigated.

3.2 Electric Potential (ϕ) Based Quasi-static SDM

The shunt capacitance can be evaluated by obtaining the total electric charges accumulated on the conductor when excited with a known electric potential. The total charges on the conductor are calculated by integrating the surface charge density on the strip over the strip width (see Fig.3.2).

$$Q = \int_{-\frac{W}{2}}^{+\frac{W}{2}} \rho(x)dx = C_{eff}(\omega)V \qquad (3.1)$$

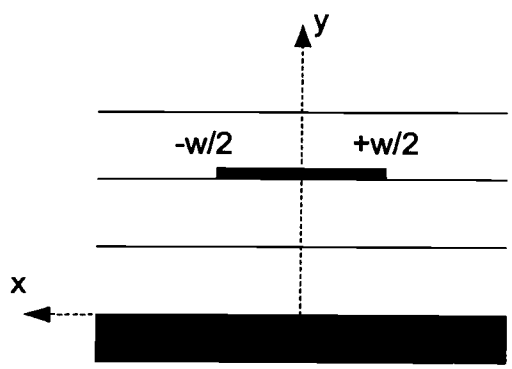

Figure 3.2 Planar strip embedded in multilayered media

In order to simplify the whole procedure, the **x** axis is transformed into the spectral domain (α) since the media are homogeneous in that direction. This approach greatly reduces the entire computation since the convolution with the spatial Green's function is changed to a simple multiplication in the spectral domain.

- Electric Potential Oriented Green's Function ($\widetilde{G}_{\phi}(\alpha)$)

The potential at an observation point due to a given source distribution can be represented in terms of Green's function $G_{\phi}(\hat{\mathbf{r}}_1)$ which represents the potential corresponding to a unit source $\delta(\hat{\mathbf{r}}_2)$ at location $\hat{\mathbf{r}}_2$.

$$\nabla^2\phi(\hat{\mathbf{r}}_1) = -\frac{\rho(\hat{\mathbf{r}}_2)}{\varepsilon} \tag{3.2}$$

$$\nabla^2 G_{\phi}(\hat{\mathbf{r}}_1) = -\delta(\hat{\mathbf{r}}_2) \tag{3.3}$$

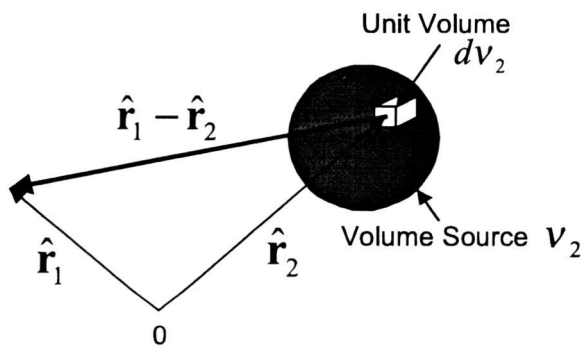

Figure 3.3 Electric potential representation in terms of electric potential oriented Green's function

If the charge distribution is inside an arbitrary volume, as depicted in Figure 3.3, the corresponding potential can be expressed by spatial convolution.

$$\phi(\hat{\mathbf{r}}_1) = \frac{1}{\varepsilon}\int_{v2} G_\phi(\hat{\mathbf{r}}_1 - \hat{\mathbf{r}}_2)\rho_{v2}(\hat{\mathbf{r}}_2)d(v2) \tag{3.4}$$

The corresponding spectral domain representation becomes

$$\tilde{\phi}(\alpha, y) = \frac{1}{\varepsilon}\tilde{G}_\phi(\alpha, y)\tilde{\rho}(\alpha, y) \tag{3.5}$$

Using this concept, the Green's function for a planar transmission line is derived by solving Poisson's equation for a unit point charge. If the wave is propagating in the **z** direction, the potential changes only in **x** and **y** directions. The Poisson equation and its spectral (α) domain representation are

$$\frac{\partial^2\phi(x,y)}{\partial x^2} + \frac{\partial^2\phi(x,y)}{\partial y^2} = -\frac{\rho(x)\delta(y-h)}{\varepsilon} \tag{3.6}$$

$$\downarrow$$

$$(j\alpha)^2\tilde{\phi}(\alpha,y) + \frac{d^2}{dy^2}\tilde{\phi}(\alpha,y) = -\frac{\tilde{\rho}(\alpha)}{\varepsilon} \tag{3.7}$$

As an example, the Green's function for a single conductor with single layered medium shown in Figure 3.4 is derived in this section. The solutions to the 2nd order differential equation (3.8) at each layer are given in the form of

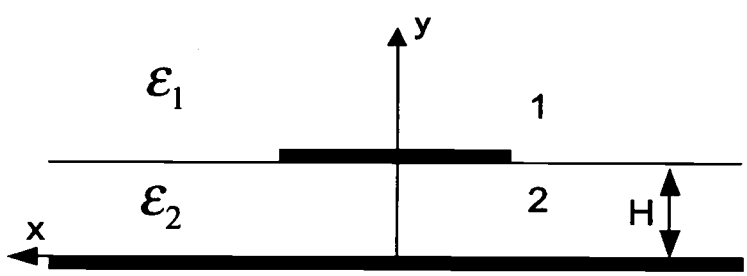

Figure 3.4 Single line structure consisting of two media

$$\tilde{\phi}_1(\alpha, y) = Ae^{-|\alpha|(y-H)} + Be^{|\alpha|(y-H)} = Ae^{-|\alpha|(y-H)} \text{ in medium 1} \quad (3.8)$$

$$\tilde{\phi}_2(\alpha, y) = C\cosh(|\alpha|y) + D\sinh(|\alpha|y) = D\sinh(|\alpha|y) \text{ in medium 2} \quad (3.9)$$

At the interface of the two media, the potentials for both media must be the same. Thus, two of the unknown coefficients are related as

$$\tilde{\phi}_1(\alpha, h) = \tilde{\phi}_2(\alpha, h) = A = D \cdot Sinh(|\alpha|h) \text{ at } y=H$$

$$\therefore D = \frac{A}{Sinh(|\alpha|h)} \quad (3.10)$$

Another boundary condition can be stated as $D_{n1} - D_{n2} = -\rho_s$ at $y=H$ from Gauss's law, which yields the other unknown coefficient, A, i.e.,

$$\varepsilon_1(-|\alpha| A) - \varepsilon_2\left(|\alpha| \frac{A}{Sinh(|\alpha|h)}\right) Cosh(|\alpha|h) = -\tilde{\rho}(\alpha)$$

$$\therefore A = \frac{\tilde{\rho}(\alpha)}{|\alpha|(\varepsilon_1 + \varepsilon_2 \cdot Coth(|\alpha|h))} \quad (3.11)$$

Inserting this coefficient into the potential function, the potential can be represented in terms of the Green's function and surface charge density.

$$\left.\frac{\tilde{\rho}(\alpha)}{|\alpha|(\varepsilon_1 + \varepsilon_2 \cdot Coth(|\alpha|h)} e^{-|\alpha|(y-H)}\right|_{y=H} = \tilde{\phi}_1(\alpha) = \tilde{\phi}_2(\alpha) = \tilde{\phi}(\alpha)$$

$$= \frac{\tilde{\rho}(\alpha)}{|\alpha|(\varepsilon_1 + \varepsilon_2 \cdot Coth(|\alpha|h))} = \frac{1}{\varepsilon_o} \tilde{G}_\phi(\alpha)\tilde{\rho}(\alpha)$$

$$\therefore \tilde{G}_\phi(\alpha) = \frac{1}{|\alpha|[\varepsilon_{r1} + \varepsilon_{r2} \cdot Coth(|\alpha|h)]} \quad (3.12)$$

The Green's function for multilayered media can be obtained in a similar fashion. Using Wheeler's transmission line approach [70], a generalized Green's function for an arbitrarily layered substrate can be obtained in the following manner, as illustrated in the Figure 3.5.

$$\tilde{G}_{\phi}(\alpha) = \frac{1}{|\alpha|(Y_H + Y_L)} \tag{3.13}$$

where

$$Y_L = Y_o \frac{Y_o + Y_L' \coth(|\alpha| H_1)}{Y_L' + Y_o \coth(|\alpha| H_1)}.$$

For instance, the Green's function for a microstrip line on two lossy substrate layers is

$$\tilde{G}_{\phi}(\alpha) = \frac{1}{|\alpha|\left(1 + \varepsilon_{c1} \dfrac{\varepsilon_{c1} + \varepsilon_{c2} \coth(|\alpha| H_2)\coth(|\alpha| H_1)}{\varepsilon_{c2} \coth(|\alpha| H_2) + \varepsilon_{c1} \coth(|\alpha| H_1)}\right)} \tag{3.14}$$

where

$$\varepsilon_{ci} = \varepsilon_i - j\frac{\sigma_i}{\omega \varepsilon_o}.$$

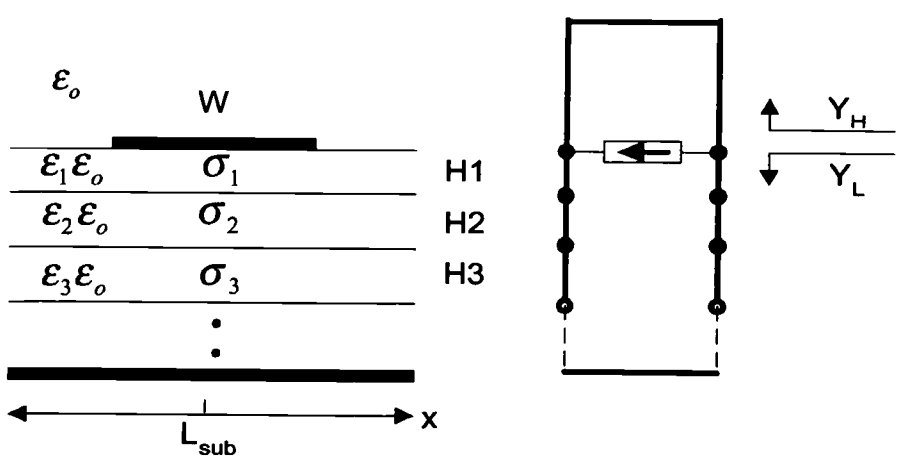

Figure 3.5 Layered media and its equivalent transmission line model

- Charge Distribution Function (Basis Function)

Suitably selected basis function can greatly reduce the computational procedure and provide faster convergence. Since Chebyshev polynomials adequately approximate the charge distribution on the conductor, Chebyshev polynomials associated with the edge condition are used in this work. The corresponding spectral domain expressions for these functions become Bessel functions. Here, only even functions are needed for a single line structure, and N_f+1 basis functions are used. The expansion of the charge density becomes

$$\rho(x)=\sum_{n=0}^{N_f} a_n \frac{T_{2n}\left(\frac{2x}{W}\right)}{\sqrt{1-\left(\frac{2x}{W}\right)^2}} \rightarrow \tilde{\rho}(\alpha)=\frac{\pi}{2}\sum_{n=0}^{N_f} a_n W(-j)^{2n} J_{2n}\left(\frac{|\alpha|W}{2}\right) \qquad (3.15)$$

where

a_n : unknown coefficient of *n-th* basis function

$T_n(\chi)$: *n-th* order Chebyshev polynomial [Appendix 3]

$J_n(\chi)$: *n-th* order Bessel Function of the 1st kind [Appendix 2].

- Galerkin's Procedure

The equations given in α domain can be re-written as

$$\tilde{\phi}(\alpha)=\frac{1}{\varepsilon_o}\tilde{G}_\phi(\alpha)\tilde{\rho}(\alpha)=\frac{\pi W}{2\varepsilon_o}\sum_{n=0}^{N_f} a_n(-j)^{2n}\tilde{G}_\phi(\alpha)J_{2n}\left(\frac{|\alpha|W}{2}\right). \qquad (3.16)$$

As a special case of the Rayleigh-Ritz method, the Galerkin's method uses the same basis functions as the weight functions. Multiplying both sides with orthogonal functions as

weight functions and taking the inner product (i.e., integrating over the entire domain) results in

$$\int_{-\infty}^{\infty} \tilde{\phi}(\alpha)(-j)^{2m} J_{2m}\left(\frac{|\alpha|W}{2}\right) d\alpha$$

$$= \frac{\pi W}{2\varepsilon_o} \sum_{n=0}^{N} a_n (-j)^{2n+2m} \int_{-\infty}^{\infty} \tilde{G}_{\phi}(\alpha) J_{2n}\left(\frac{|\alpha|W}{2}\right) J_{2m}\left(\frac{|\alpha|W}{2}\right) d\alpha . \qquad (3.17)$$

The left-hand side can be simplified using Parseval's theorem and the properties of Chebyshev polynomials as

$$L.H.S = 2\pi \frac{2}{\pi W} \int_{-\infty}^{\infty} \phi(x) \frac{T_{2m}\left(\frac{2x}{W}\right)}{\sqrt{1-\left(\frac{2x}{W}\right)^2}} dx = \frac{4}{W} \frac{W}{2} \int_{-1}^{1} \phi(x) \frac{T_{2m}(\chi)}{\sqrt{1-\chi^2}} d\chi$$

$$= \begin{cases} 2\pi V & if \quad m = 0 \\ 0 & Otherwise \end{cases} \qquad (3.18)$$

since $\phi(x)$ is assumed to be constant on the strip. The right-hand side becomes a matrix whose elements are calculated by integration. The resulting matrix equation is given by

$$\begin{bmatrix} S_{0,0} & \cdots & S_{0,N_f} \\ \vdots & & \vdots \\ S_{N_f,0} & \cdots & S_{N_f,N_f} \end{bmatrix} \begin{bmatrix} a_0 \\ \vdots \\ a_{N_f} \end{bmatrix} = \begin{bmatrix} b_0 \\ \vdots \\ b_{N_f} \end{bmatrix} = \begin{bmatrix} 2V\varepsilon_o/W \\ \vdots \\ 0 \end{bmatrix} \qquad (3.19)$$

where **a** is the unknown coefficient vector, and **b** is the known potential vector.

The linear equation (3.19) simply represented as

$$S_{nm}(-j)^{2m+2n}a_n = \left\{ \begin{array}{ll} \frac{2\varepsilon_o}{W}V & n=0 \\ 0 & Otherwise \end{array} \right\}.$$

The elements of the S matrix are

$$S_{nm} = \int_0^{\infty} \tilde{G}_{\phi}(\alpha) J_{2n}\left(\frac{\alpha W}{2}\right) J_{2m}\left(\frac{\alpha W}{2}\right) d\alpha \qquad (3.20)$$

To facilitate the integration in (3.20), the α variable is characterized by introducing electric walls at the right and left side of the structure. The walls are separated by a sufficiently large distance L_{sub} (here, taken as $L_{sub} \approx 10W$). The discretized α variable becomes

$$\alpha = \frac{k\pi}{L_{sub}}, \quad k = 0...\infty, \quad L_{sub} \cong 10 \cdot W. \qquad (3.21)$$

and the matrix element S_{nm} are given as

$$S_{nm} = \sum_{k=0}^{N_k} \left[\tilde{G}_{\phi}\left(\frac{\pi}{L_{sub}}k\right) J_{2n}\left(\frac{\pi W}{2L_{sub}}k\right) J_{2m}\left(\frac{\pi W}{2L_{sub}}k\right) \frac{k}{L_{sub}} \right] \qquad (3.22)$$

where N_k is a suitably chosen upper limit of the summation.

- Charges on the Conductor

After calculating the unknown coefficient vector, $\boldsymbol{a}$, the total charge can be determined by integrating the surface charge density over the strip width. This results in

$$Q = a_0 \int_{-W/2}^{W/2} \frac{T_0\left(\frac{2x}{W}\right)}{\sqrt{1-\left(\frac{2x}{W}\right)^2}} dx + \cdots + a_{2N_f} \int_{-W/2}^{W/2} \frac{T_{2N_f}\left(\frac{2x}{W}\right)}{\sqrt{1-\left(\frac{2x}{W}\right)^2}} dx + \cdots \qquad (3.23)$$

Analytically, each integration term is already known using the orthogonality property of Chebyshev functions. That is,

$$\int_{-1}^{1} \frac{T_m(x)}{\sqrt{1-x^2}} dx = \begin{cases} \pi & if \quad m = 0 \\ 0 & otherwise \end{cases} \qquad (3.24)$$

Thus, only the first term remains, which can be obtained from a simple transformation. The total charge is given by

$$Q = a_o \int_{-W/2}^{+W/2} \frac{T_0\left(\frac{2x}{W}\right)}{\sqrt{1-\left(\frac{2x}{W}\right)^2}} dx = a_o \frac{W}{2} \int_{-1}^{1} \frac{T_0(\chi)}{\sqrt{1-(\chi)^2}} d\chi = a_o \frac{W\pi}{2} \qquad (3.25)$$

The unknown coefficient vector is obtained as

$$\begin{bmatrix} a_0 \\ \vdots \\ a_N \end{bmatrix} = \begin{bmatrix} S_{0,0} & \cdots & S_{0,N_f} \\ \vdots & & \vdots \\ S_{N_f,0} & \cdots & S_{N_f,N_f} \end{bmatrix}^{-1} \begin{bmatrix} 2V\varepsilon_o/W \\ \vdots \\ 0 \end{bmatrix}$$

$$= \begin{bmatrix} T_{0,0} & \cdots & T_{0,N_f} \\ \vdots & & \vdots \\ T_{N_f,0} & \cdots & T_{N_f,N_f} \end{bmatrix} \begin{bmatrix} 2V\varepsilon_o/W \\ \vdots \\ 0 \end{bmatrix} = \begin{bmatrix} 2T_{0,0}V\varepsilon_o/W \\ \vdots \\ 2T_{N,0}V\varepsilon_o/W \end{bmatrix} \qquad (3.26)$$

If the applied voltage of the conductor is assumed to be 1 volt, the total charge directly gives the equivalent capacitance. It should be noted that the equivalent capacitance is complex and frequency-dependent if the substrate includes any lossy material.

- Examples

To illustrate the technique, the charge distributions on a microstrip are obtained for different substrate conductivities. As shown in Figure 3.6, the charge density is higher at the edges of the strip. Furthermore, the total charge on the conductor is larger for large substrate conductivities in comparison to small substrate conductivities. This can be explained with the help of the equivalent circuit shown in Figure 2.2.

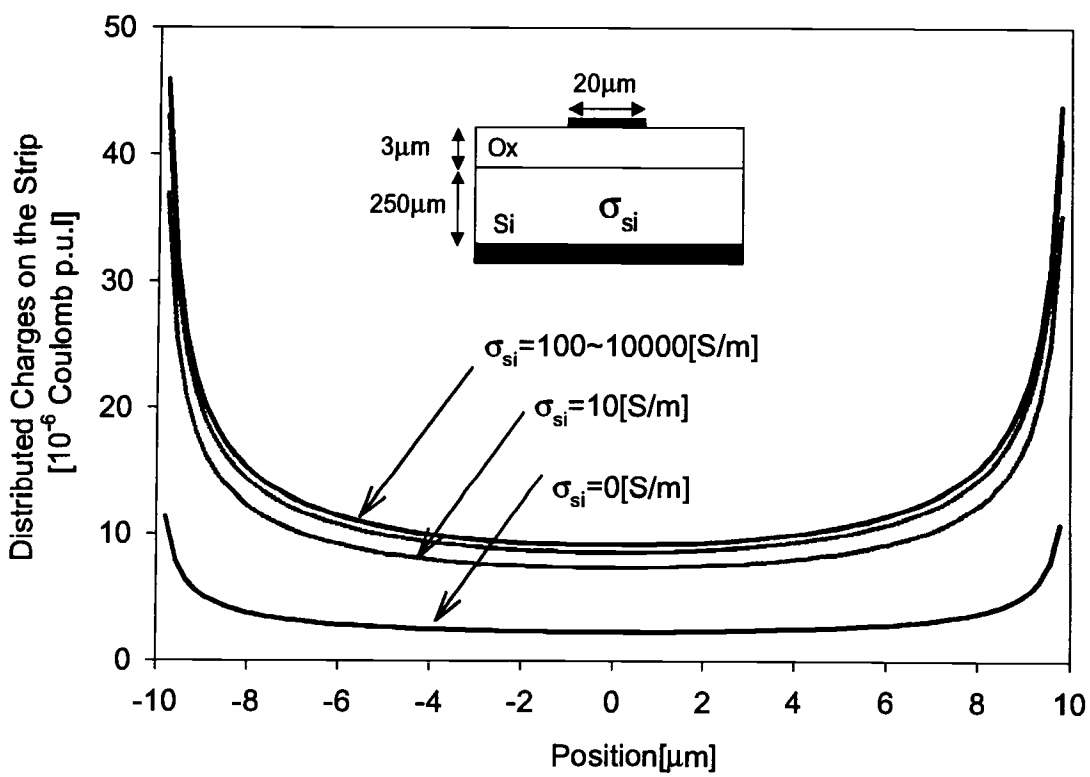

Figure 3.6 Equivalent surface charge distribution on the conductor @1GHz for 1[V] electric potential.

With increasing substrate conductivity, the conductance, G_{si}, becomes more dominant and the effective shunt capacitance approaches the oxide capacitance, C_{Ox}, In contrast, for low substrate conductivities, C_{si} dominates and the effective shunt capacitance is approximately given by $C=(C_{Ox}C_{si})/(C_{Ox}+C_{si})$.

3.3 Physical Concept of Magnetic Vector Potential

In order to understand the physical behavior of magnetic vector potential, one can start from the following relation between magnetic vector potential and magnetic flux density.

$$\nabla \times \mathbf{A} = \mathbf{B} \tag{3.27}$$

Physically, this relation can be expressed using Stoke's theorem as

$$\int_S (\nabla \times \mathbf{A}) \cdot \mathbf{ds} = \oint_C \mathbf{B} \cdot \mathbf{ds} \tag{3.28}$$

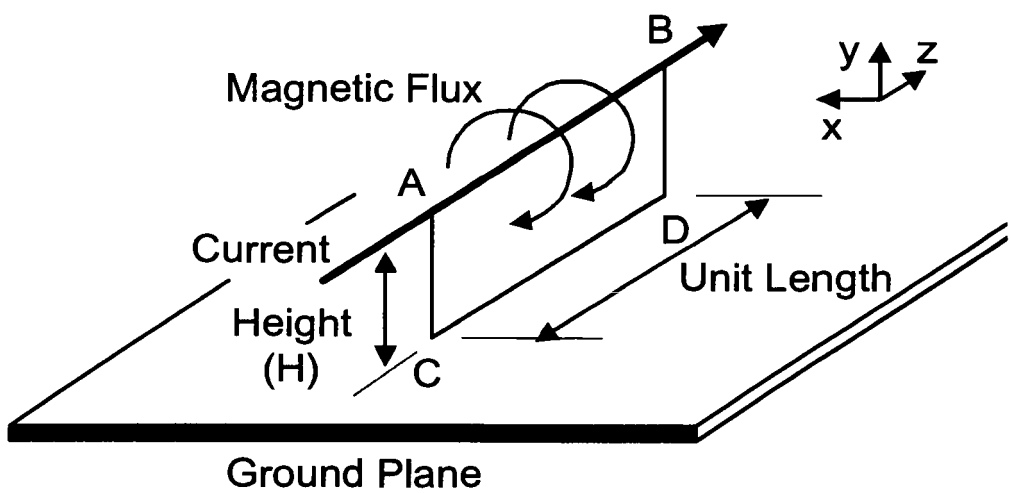

Figure 3.7 Concept of magnetic vector potential in microstrip line structure

If S is the surface enclosed by path ABCD in Figure 3.7, and Λ is the total magnetic flux passing through the surface S, the RHS becomes Λ..

$$\Lambda = \int_S \mathbf{B}\cdot\mathbf{ds} = \int_S (\nabla\times\mathbf{A})\cdot\mathbf{ds} = \oint_c \mathbf{A}\cdot\mathbf{dl} \qquad (3.29)$$

For a z-directed current, only the $\hat{\mathbf{z}}$ component of **A** is nonzero. Thus,

$$\oint_c \mathbf{A}\cdot\mathbf{dl} = \oint_c A_z\hat{\mathbf{z}}\cdot\mathbf{dl}$$

$$= \int_{AB} A_z\hat{\mathbf{z}}\cdot dz\hat{\mathbf{z}} + \int_{BD} A_z\hat{\mathbf{z}}\cdot dy(-\hat{\mathbf{y}}) + \int_{DC} A_z\hat{\mathbf{z}}\cdot dz(-\hat{\mathbf{z}}) + \int_{CA} A_z\hat{\mathbf{z}}\cdot dy\hat{\mathbf{y}}$$

$$= \int_{AB} A_z\hat{\mathbf{z}}\cdot dz\hat{\mathbf{z}} + \int_{DC} A_z\hat{\mathbf{z}}\cdot dz(-\hat{\mathbf{z}}) \qquad (3.30)$$

The 2nd integration is 0 since the magnetic vector potential at the ground plane is taken as 0. In addition, if the paths *AB* and *DC* are of unit length, we can summarize the relation in the following form.

$$\Lambda = \int_S \mathbf{B}\cdot\mathbf{ds} = \int_S (\nabla\times\mathbf{A})\cdot\mathbf{ds} = \oint_c \mathbf{A}\cdot\mathbf{dl} = A_z \qquad (3.31)$$

Consequently, the flux linkage Λ per unit length between the strip and ground plane is equivalent to the vector magnetic potential A_z can be specified on the surface of the strip. This means that A_z can be specified on the conductor surface and the strip current can be determined, as illustrated in the following section.

3.4 Magnetic Vector Potential (A) Based Quasi-static SDM

The main approach for determining inductance by specifying A_z and calculating the strip current is analogous to the calculation of the charge distribution in the electric potential-based SDM. Since the shape of the current distribution for a given electric potential on the conductor is similar to the shape of the charge distribution, the same

basis functions are used. However, the Green's function here is different and must first be derived.

- Magnetic Potential Oriented Green's Function

If a volumetric magnetic vector potential is located at $\hat{\mathbf{r}}_2$, the corresponding current density at $\hat{\mathbf{r}}_1$ can be expressed as

$$\nabla^2 \mathbf{A}(\hat{\mathbf{r}}_1) - j\omega\mu\sigma\mathbf{A}(\hat{\mathbf{r}}_1) = -\mu\mathbf{J}(\hat{\mathbf{r}}_2) \qquad (3.32)$$

$$\nabla^2 \mathbf{G}_A(\hat{\mathbf{r}}_1) - j\omega\mu\sigma\mathbf{G}_A(\hat{\mathbf{r}}_1) = - \ (\hat{\mathbf{r}}_2) \qquad (3.33)$$

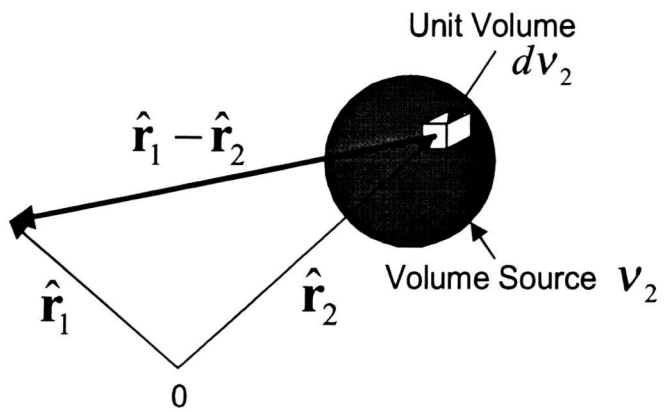

Figure 3.8 Magnetic vector potential representation in terms of magnetic potential oriented Green's function

Here, the equation (3.32) is derived in Appendix 8. The equations above can extract the relations between current density and magnetic vector potential in terms of a vector potential oriented Green's function representing the corresponding magnetic potential when a unit vector source is located at the same location. The tangential current on the

conducting strip is composed of both **z** and **x** components which represent the propagation and dispersion, respectively. However, dispersion critically appears only when the conducting strip is wide compared to the height of substrates, or the operation is in the quasi-TEM mode and in the higher frequency range.

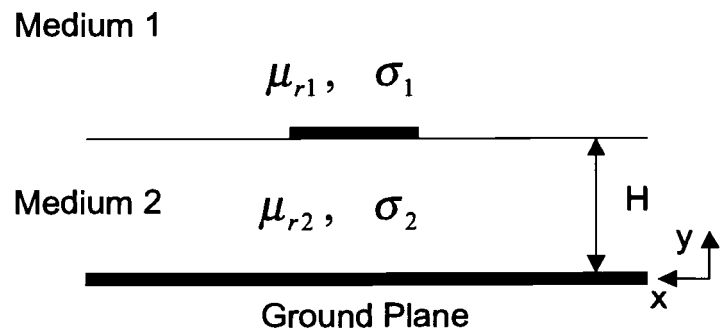

Figure 3.9 Single line structure with two media for deriving the magnetic vector potential based Green's function.

Otherwise, this phenomenon barely influences the mode parameters, and it is negligible especially in the skin-effect mode. Thus, it is assumed that only the longitudinal $\hat{\mathbf{z}}$ current component exists. By applying this approach, the total current on the strip in Figure 3.9 can be obtained by integrating the current distribution. The equivalent inductance is given as follows.

$$I_z = \int_{-\frac{W}{2}}^{+\frac{W}{2}} J_z(x)dx = \Lambda / L_{eff}(\omega) \qquad (3.34)$$

Since the current component has only a $\hat{\mathbf{z}}$ component, the magnetic vector potential also has only a $\hat{\mathbf{z}}$ component. Thus, the vector quantities of the magnetic potential equation and Green's function become scalar equations.

$$\nabla^2 A_z(x,y) - j\omega\mu\sigma A_z(x,y) = -\mu J_z(x,y) \qquad (3.35)$$

$$\nabla^2 G_A(x,y) - j\omega\mu\sigma G_A(x,y) = - \ (x,y) \qquad (3.36)$$

Using the magnetic potential Green's function, the relationship between current density and magnetic potential is

$$A_z(\hat{\mathbf{r}}_1) = \mu \int_{v2} G_A(\hat{\mathbf{r}}_1 - \hat{\mathbf{r}}_2) J_{z,v2}(\hat{\mathbf{r}}_2) d(v2) \qquad (3.37)$$

In the spectral domain, this integral relationship transforms to the product form given by

$$\tilde{A}_z(\alpha,y) = \mu \tilde{G}_A(\alpha,y) \tilde{J}_z(\alpha,y) \qquad (3.38)$$

In order to derive the spectral domain expression for the magnetic potential Green's function, one has to solve an ordinary differential equation subject to the boundary conditions. The magnetic potential equation in spectral domain is

$$(j\alpha)^2 \tilde{A}_z(\alpha,y) + \frac{d^2}{dy^2} \tilde{A}_z(\alpha,y) - j\omega\mu\sigma \tilde{A}_z(\alpha,y) = -\mu \tilde{J}_z(\alpha,y) \qquad (3.39)$$

In a source free region, this equation becomes

$$\frac{d^2}{dy^2} \tilde{A}_z(\alpha,y) = (\alpha^2 + j\omega\mu_i\sigma_i) \tilde{A}_z(\alpha,y) = \alpha_i^{\ 2} \tilde{A}_z(\alpha,y) \qquad (3.40)$$

where

$$\alpha_i = \sqrt{\alpha^2 + j\omega\mu_i\sigma_i} \quad \text{and} \quad \mu_i = \mu_o\mu_{ri}.$$

If we assume that medium 1 is not bounded by electric sidewalls, the field will be evanescent. In medium 2 the magnetic potential function is bounded by the strip and ground plane. Thus, the solution to the 2nd order ordinary differential equation (3.40) in each region becomes

$$\tilde{A}_{z1}(\alpha, y) = Be^{-\alpha_1(y-H)} \text{ in medium 1} \qquad (3.41)$$

$$\tilde{A}_{z2}(\alpha, y) = C\sinh(\alpha_2 y) \text{ in medium 2} \qquad (3.42)$$

Here, B and C are unknown coefficients.

The potential at the interface between medium 1 and medium 2 must be the same, Thus, the unknown coefficient C can be readily derived from the following equation.

$$B = C \cdot Sinh(\alpha_2 H) \qquad (3.43)$$

The boundary condition at the interface (y=H) is given by

$$\frac{\partial A_{z1}(x,y)}{\partial y} - \frac{\partial A_{z2}(x,y)}{\partial y} = -\mu J_z(x) \qquad (3.44)$$

The corresponding spectral domain expression becomes

$$\frac{1}{\mu_1}\frac{d\tilde{A}_{z1}(\alpha,y)}{dy} - \frac{1}{\mu_2}\frac{d\tilde{A}_{z2}(\alpha,y)}{dy} = -\tilde{J}_z(\alpha) \qquad (3.45)$$

By rewriting equation (3.45) in terms of unknown coefficient B, the following equation results:

$$\frac{1}{\mu_1}(-\alpha_1 B) - \frac{1}{\mu_2}\left(\alpha_2 \frac{B}{Sinh(\alpha_2 H)}\right)Cosh(\alpha_2 H) = -\tilde{J}_z(\alpha) \qquad (3.46)$$

Thus, the unknown coefficient B can be solved as

$$B = \frac{\tilde{J}_z(\alpha)}{\frac{1}{\mu_1}\alpha_1 + \frac{1}{\mu_2}\alpha_2 Coth(\alpha_2 H)}. \qquad (3.47)$$

By inserting the coefficient B into (3.46), the magnetic potential at the interface between the two media can be represented by the Green's function as

$$\tilde{A}_z(\alpha, H) = \frac{\tilde{J}_z(\alpha)}{\frac{1}{\mu_1}\alpha_1 + \frac{1}{\mu_2}\alpha_2 \coth(\alpha_2 H)} = \mu_o \tilde{G}_A(\alpha)\tilde{J}_z(\alpha). \qquad (3.48)$$

Finally, the Green's function is derived as

$$\tilde{G}_A(\alpha) = \frac{1}{\frac{1}{\mu_{r1}}\alpha_1 + \frac{1}{\mu_{r2}}\alpha_2 \coth(\alpha_2 H)} \qquad (3.49)$$

To generalize, the Green's function for an arbitrary number of media can be readily represented using Wheeler's approach.

$$\tilde{G}_A(\alpha) = \frac{1}{\tilde{Y}_H(\alpha) + \tilde{Y}_L(\alpha)} \qquad (3.50)$$

$$\tilde{Y}(\alpha)_{L,i} = \tilde{Y}(\alpha)_{o,i} \frac{\tilde{Y}(\alpha)_{o,i} + \tilde{Y}(\alpha)_{L,i-1} \coth(\alpha_i H_i)}{\tilde{Y}(\alpha)_{L,i-1} + \tilde{Y}(\alpha)_{o,i} \coth(\alpha_i H_i)} \qquad (3.51)$$

Assuming $\mu_{r1} = \mu_{r2} = \cdots = 1.0$, each $\tilde{Y}(\alpha)_{o,i}$ can be obtained as

$$\tilde{Y}(\alpha)_{o,i} = \alpha_i = \sqrt{\alpha^2 + j\omega\mu_o\sigma_i}$$

For example, the Green's function for the magnetic potential for a two-layer case is

$$\tilde{G}_A(\alpha) = \frac{1}{\alpha_o + \alpha_1 \dfrac{\alpha_1 + \alpha_2 Coth(\alpha_2 H_2) Coth(\alpha_1 H_1)}{\alpha_2 Coth(\alpha_2 H_2) + \alpha_1 Coth(\alpha_1 H_1)}} \qquad (3.52)$$

- Galerkin's Procedure

Galerkin's procedure for this spectral domain approach is similar to that of the electric potential-based SDM. The magnetic vector potential can be expressed in the following form if Chebyshev basis functions with unknown coefficients a_n are used for current. That is

$$\tilde{A}_z(\alpha, y) = \mu \tilde{G}_A(\alpha, y) \tilde{J}_z(\alpha, y) = \frac{\pi W \mu_o}{2} \sum_{n=0}^{N} a_n (-j)^{2n} \tilde{G}_A(\alpha) J_{2n}\left(\frac{\alpha W}{2}\right) \qquad (3.53)$$

where

$$J_z(x) = \sum_{n=0}^{N} a_n \frac{T_{2n}\left(\dfrac{2x}{W}\right)}{\sqrt{1 - \left(\dfrac{2x}{W}\right)^2}} \qquad (3.54)$$

The spectral domain representation for (3.54) becomes

$$\tilde{J}_z(\alpha) = \frac{\pi}{2} \sum_{n=0}^{N} a_n W (-j)^{2n} J_{2n}\left(\frac{\alpha W}{2}\right) \qquad (3.55)$$

Multiplying with the orthogonal functions as weight functions on both sides and taking the inner product results in

$$\int_{-\infty}^{\infty} \tilde{A}_z(\alpha)(-j)^{2m} J_{2m}\left(\frac{\alpha W}{2}\right) d\alpha$$

$$= \frac{\pi W \mu_o}{2} \sum_{n=0}^{N} a_n (-j)^{2n+2m} \int_{-\infty}^{\infty} \tilde{G}_A(\alpha) J_{2n}\left(\frac{\alpha W}{2}\right) J_{2m}\left(\frac{\alpha W}{2}\right) d\alpha \qquad (3.56)$$

Similar to the quasi-electrostatic case described in the previous section, application of Galerkin's procedure results in a set of linear equations for the unknown current coefficients, i.e.,

$$\sum_{m}^{N} \sum_{n}^{N} S_{nm} (-j)^{2m+2n} a_n = \begin{cases} \dfrac{2}{W\mu_o} \Lambda & n = 0 \\ 0 & otherwise \end{cases} \qquad (3.57)$$

Each element can be obtained by integration as

$$S_{nm} = \int_0^{\infty} \tilde{G}_A(\alpha) J_{2n}\left(\frac{\alpha W}{2}\right) J_{2m}\left(\frac{\alpha W}{2}\right) d\alpha \qquad (3.58)$$

where

$$\alpha = \frac{k\pi}{L_{sub}}, \quad k = 0 \ldots \infty, \quad L_{sub} \cong 10 \cdot W.$$

- Total Current on the Strip and Equivalent Inductance

Calculating the current on the strip is as similar to calculating the total electric charge. The solution to the linear equation

$$\begin{bmatrix} a_0 \\ \vdots \\ a_N \end{bmatrix} = \begin{bmatrix} S_{0,0} & \cdots & S_{0,N_f} \\ \vdots & & \vdots \\ S_{N_f,0} & \cdots & S_{N_f,N_f} \end{bmatrix}^{-1} \begin{bmatrix} 2\Lambda/W\,\mu_o \\ \vdots \\ 0 \end{bmatrix} = \begin{bmatrix} T_{0,0} & \cdots & T_{0,N_f} \\ \vdots & & \vdots \\ T_{N_f,0} & \cdots & T_{N_f,N_f} \end{bmatrix} \begin{bmatrix} 2\Lambda/W\,\mu_o \\ \vdots \\ 0 \end{bmatrix} \quad (3.59)$$

yields the unknown coefficient vector. Then, the current is obtained as

$$I_z = a_o \int_{-W/2}^{+W/2} \frac{T_0\left(\frac{2x}{W}\right)}{\sqrt{1-\left(\frac{2x}{W}\right)^2}} dx = a_o \frac{W}{2} \int_{-1}^{1} \frac{T_0(\chi)}{\sqrt{1-(\chi)^2}} d\chi = a_o \frac{W\pi}{2} \quad (3.60)$$

where

$$a_o = \frac{2T_{0,0}}{W\mu_o}.$$

Consequently, the p.u.l. inductance can be calculated as follows:

$$I_z = \int_{-\frac{W}{2}}^{+\frac{W}{2}} J_z(x)dx = \Lambda / L_{eff}(\omega) \quad (3.61)$$

Note that the equivalent inductance is reciprocal to the calculated total current if a unit magnetic flux is assumed.

- Examples

Using the approach described above, several exemplary cases are characterized in terms of slow-wave factor and attenuation. The results are also compared with the full-wave SDM to validate this new quasi-static approach. It is interesting to examine the change in strip current as a function of substrate conductivity. In Figure 3.10, the calculated relative current distribution on the conducting strip is plotted for several cases

of substrate conductivity. Similar to the charge distributions on the conductor depicted in the Figure 3.6, the total current increases significantly for large substrate conductivities. For high substrate conductivities, the longitudinal substrate current due to the magnetic field (i.e., magnetic potential) in the substrate begins to flow close to the surface of semiconductor. For a given magnetic flux, the strip current is increased, thus lowering the inductance. From a more physical point of view, for a given strip current, the flux linkage is reduced due to the magnetic fields generated by the longitudinal substrate currents.

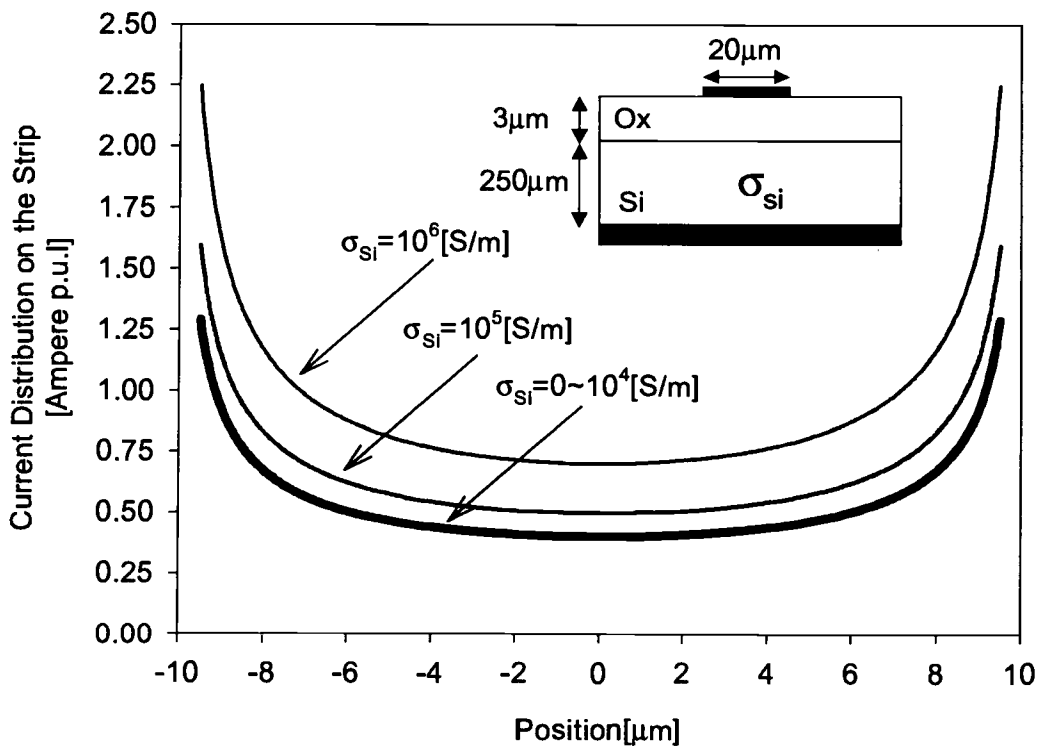

Figure 3.10 Relative current distribution on the conducting strip calculated by magnetic potential-based quasi-static SDM @ 1[GHz] assuming unit magnetic flux linkage

It is clear that the inductance calculated by the conventional method (i.e., constant value over the entire $\sigma_{si}\omega$ region) is not applicable to structures with highly lossy substrates.

Even though the dominant substrate current increases rapidly when σ_{Si} is around 10^4[S/m] for this specific case, this value, in general, depends on the operating conditions of the circuit. In most cases, it is lower than 10^4[S/m] as frequency increases. The substrate resistance can be calculated from the imaginary part of the equivalent inductance.

As another validating case, the same structure as in electric potential-based SDM approximation in Figure 2.4 is investigated with the proposed approach and compared with full-wave SDM in Figure 3.11. Since the quasi-magnetostatic SDM accurately calculates the substrate resistance together with the inductance, the slow-wave factor and attenuation obtained with the new quasi-static approach is in excellent agreement with the corresponding full-wave solutions.

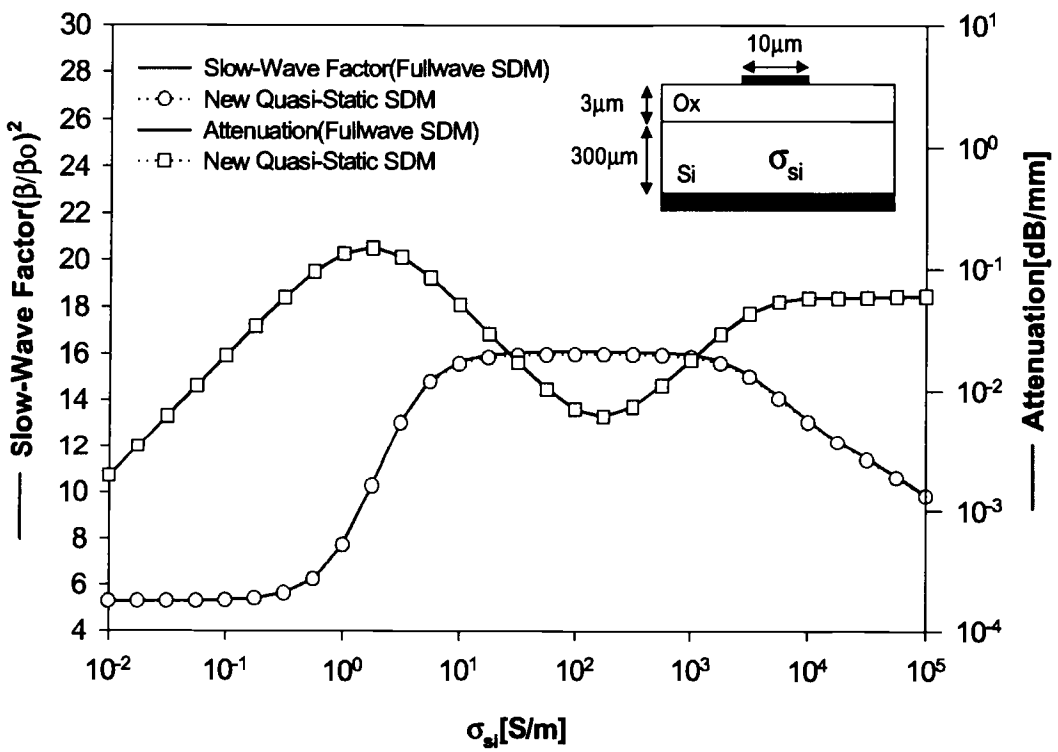

Figure 3.11 Slow-wave factor and attenuation by quasi-static and full-wave SDM

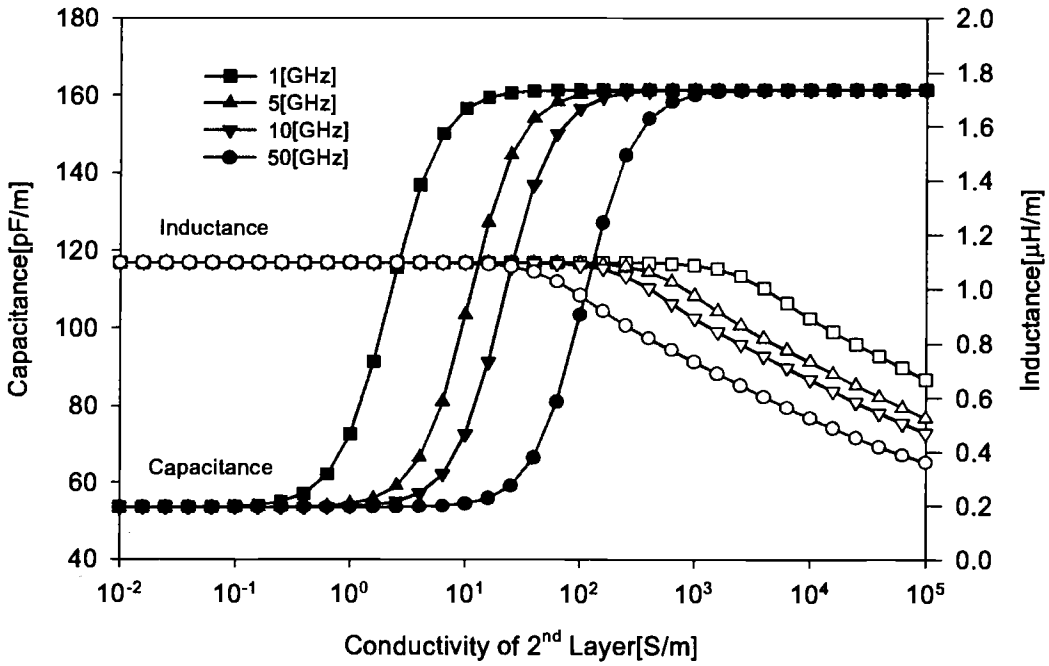

(a)

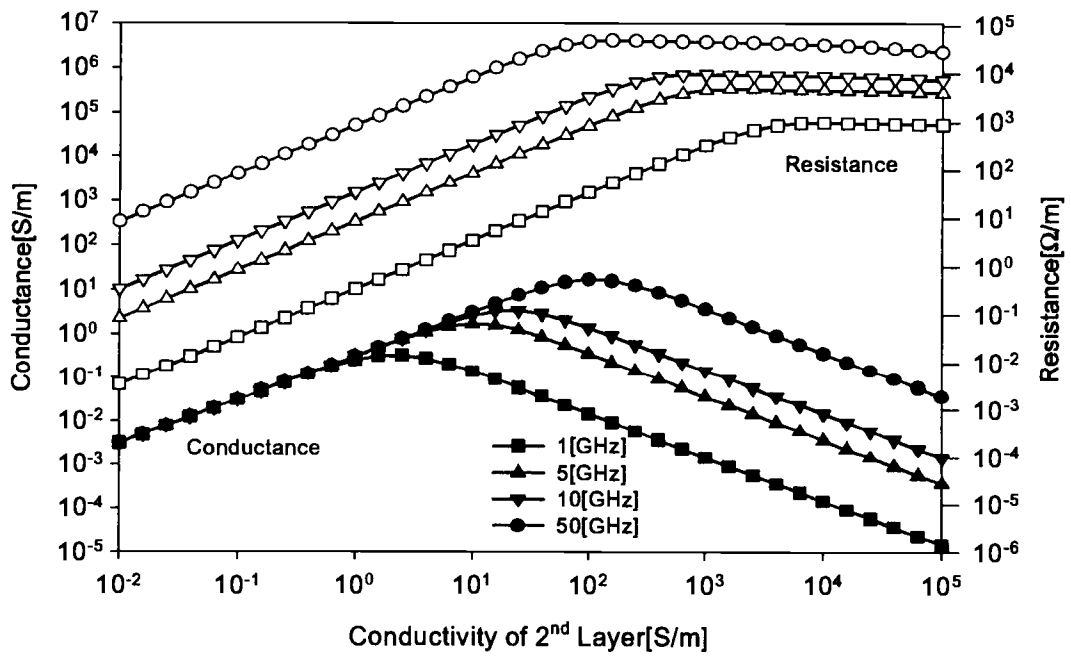

(b)

Figure 3.12 *R(ω), L(ω), G(ω), C(ω)* generated by electric and magnetic potential-based quasi-static SDM

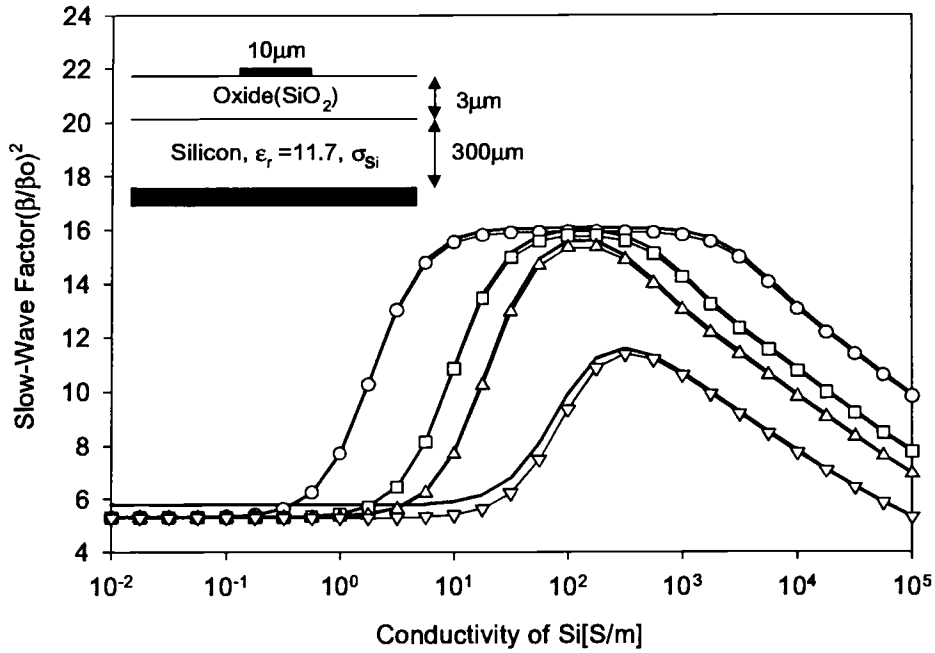

(a)

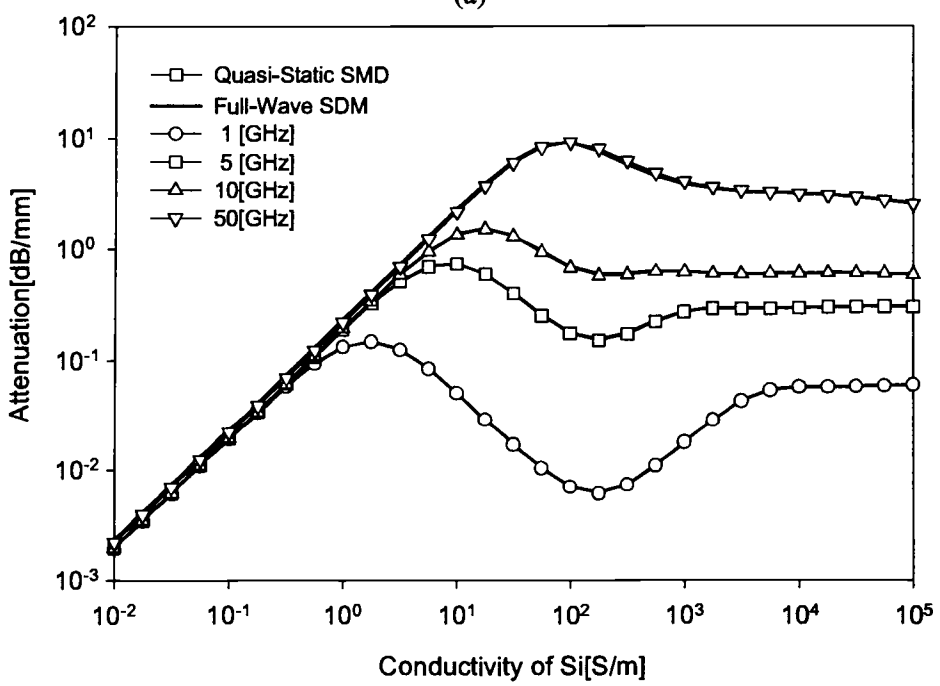

(b)

Figure 3.13 Slow-wave factor and attenuation by quasi-static SDM @1~50GHz

Next, the frequency-dependent distributed R,L,G,C parameters for the structure shown in Figure 3.1 are calculated by electric and magnetic potential-based SDM as a function of frequency and substrate conductivity and results shown in Figure 3.12.

As expected, the distributed inductance decreases with increasing substrate conductivity in the skin-effect mode region. In particular, at higher frequencies, the quasi-TEM mode region extends to higher values of conductivity, and the transmission line behavior goes into the skin-effect mode before completely extending into the slow-wave mode region. Thus, only a small portion of the slow-wave mode occupies the conductivity range at 50[GHz]. As the loss terms dominating the changes in attenuation, distributed conductance and resistance are considered in Figure 3.12(b). First, the distributed resistance significantly increases and does not decrease as much as the distributed conductance does in these cases. The series and shunt loss terms cause higher power loss as frequency increases, and consequently influence the performance of the entire circuit.

Using the distributed circuit parameters, the line mode parameters are calculated at each frequency and compared with full-wave SDM (see Figure 3.13). For all the cases the results obtained with the new quasi-static SDM are in good agreement with the full-wave SDM, except for a slight difference for the quasi-TEM mode at 50[GHz] due to dispersion, which is not an obtainable quantity by any quasi-TEM approach. This dispersion caused by the **x**-directed current component becomes important especially when relatively wide conducting strips on lossless substrate are operated at high frequency. Thus, this dispersion effect is negligible for RF/Microwave and VLSI circuits operating far below 50[GHz].

3.5 Conclusion

A new quasi-static approach for determining the complete frequency-dependent transmission line parameters for a microstrip on semiconductor has been presented. The quasi-static solution is in excellent agreement with full-wave solution, but requires significantly less computation time. The quasi-static calculation approach is summarized in Figure 3.14.

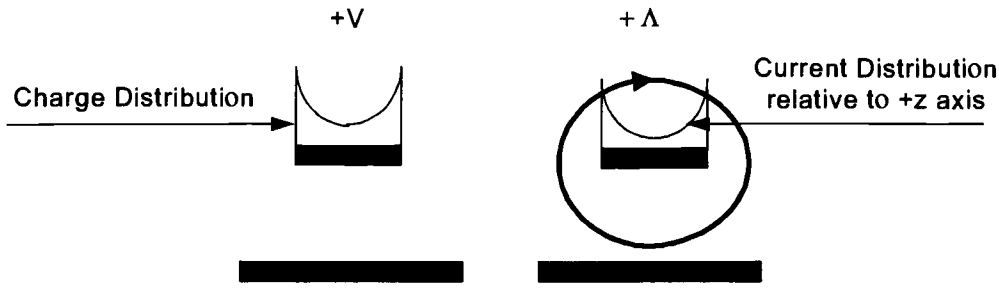

Electric Potential-based quasi-static SDM		Magnetic Potential-based quasi-static SDM
V[volt]	Applied Potential	Λ[Wb/m] or A
Total Charge [Coulomb/m]	Calculated Quantity of Source	Total Current [Ampere/m]
C, G	Calculated Parameters	L, R

Figure 3.14 Physical representation and conceptual summary of electric and magnetic potential-based quasi-static calculation approach

Mode dispersion is ignored during this procedure since the quasi-static approach assumed that the current has only a **z** component. In general, the effective dielectric constant increases as the frequency increases due to stronger electric field under the conducting strip. That is, the electric potential at each position of the conductor begins to change as the frequency increases and this horizontal potential difference on the conductor leads not only to an additional **x** directed current, but also to a change in the electric field distribution under the conductor since $d\phi(x)/dx$ is no longer 0.

In other words, the propagating mode is obviously not TEM (i.e., Ez≠0 and Hz≠0), even for lossless substrates.

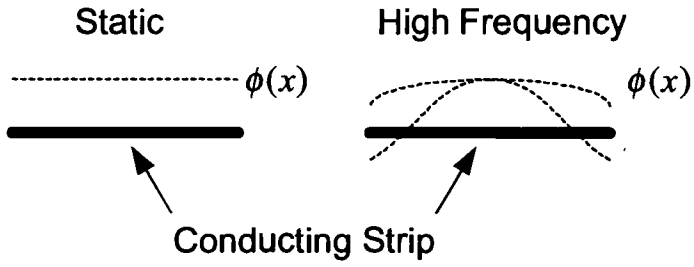

Figure 3.15 Mode dispersion due to tangential (x) voltage difference

Thus, mode dispersion is another significant factor determining the physical properties of microstrip lines at high frequency, especially when the W/H ratio is typically more than 0.5~0.1 and the operation is in the quasi-TEM mode. However, this phenomenon plays a relatively minor role if the W/H ratio is small, and it can be totally omitted for common interconnects used in RFIC's or VLSI's for which the operation is in the slow-wave or skin-effect mode, as seen in the Figure 3.15.

Additional advantages of the new quasi-static approach over full-wave techniques are that the characteristic impedance is readily obtained, and the entire computation takes approximately less than 2% of the full-wave SDM if one basis function is used and a lossless substrate is assumed. It is observed that approximately 2~3% of the computation time is achieved for general MIS structures compared with full-wave SDM.

4 MULTICONDUCTOR STRUCTURES WITH GROUND PLANE

4.1 Introduction

In this chapter, the quasi-electrostatic and quasi-magnetostatic spectral domain approaches are extended to various types of multiple coupled interconnect configurations having a ground plane at the backside of the lossy substrate. Due to the proximity of interconnects, mutual capacitive and inductive coupling can lead to significant crosstalk noise. On the other hand, coupling between lines is used in various microwave components such as directional couplers, power dividers, and coupled line filters. Hence, multiple interconnects should be modeled as a coupled transmission line system.

Figure 4.1 shows the general equivalent circuit of two coupled interconnects. In general, the coupled line system can be represented in terms of *[R], [L], [G], [C]* matrices. The off-diagonal elements in these matrices represent the coupling between the interconnects.

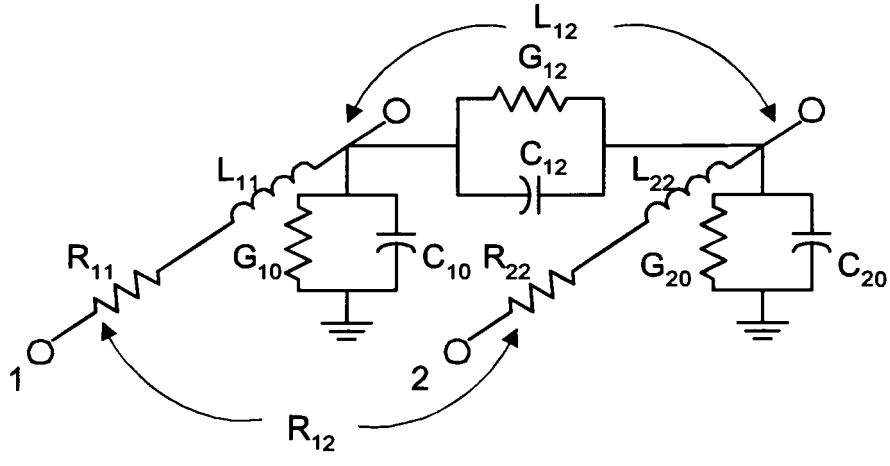

Figure 4.1 Equivalent circuit model for multiple coupled interconnects

Since the whole procedure for calculating the capacitance matrix has already been described in the literature [11~16], this chapter focuses on describing how to obtain the inductance matrix in terms of the magnetic vector potential based Green's function obtained in the previous chapter.

4.2 Single Level, Multiple Coupled Interconnects

Figure 4.2 shows a general single level multiple coupled interconnect structure. Here, the total current distribution on the *k-th* conductor with *m-th* conductor excited can be expanded in terms of the same basis functions as for the signal line case as

$$J_{z,k}(x) = \sum_{n=0}^{\infty} a_n^{k,m} \frac{T_n\left(\frac{2(x-x_k)}{W_k}\right)}{\sqrt{1-\left(\frac{2(x-x_k)}{W_k}\right)^2}} \qquad (4.1)$$

where $T_n(\chi)$ is the Chebyshev polynomial of order n.

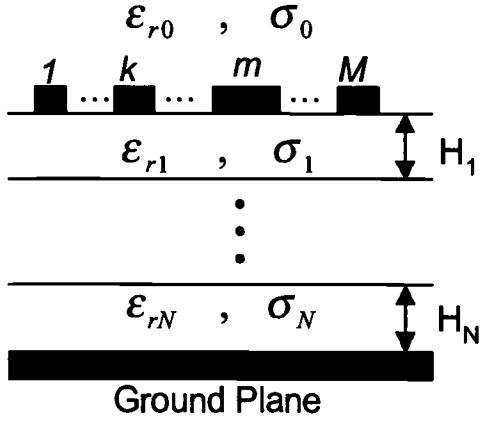

Figure 4.2 Single level, multiple coupled microstrip transmission line structure

Once the current distribution is obtained, total current flowing on the *k-th* conductor can be calculated by integration.

$$I_{z,k} = \int_{x_k - \frac{W_k}{2}}^{x_k + \frac{W_k}{2}} J_{z,k}(x)dx \qquad (4.2)$$

Unlike the relations between charge and capacitance, inductance is reciprocal to the current on the conductor. By employing a dummy matrix *[K]* so that each element is proportional to the current, all elements of *[K]* can be found from the relations between the resulting current on the *k-th* conductor corresponding to the excitation of the *m-th* conductor. This relationship can be expressed in matrix form as

$$[I_z] = [K][\Lambda] \qquad (4.3)$$

where

$$K_{k,m} = \left.\frac{I_{z,k}}{\Lambda_m}\right|_{\substack{I_{z,l}=0 \\ l \neq k}} \quad \text{and} \quad [K] = [L]^{-1}.$$

- Calculation Approach

By transforming the spatial domain representation of the current distribution into the spectral domain, the vector magnetic potential can be written in terms of a Green's function and current expansion on conductor for *k*.

$$\tilde{J}_{z,k}(\alpha) = \sum_n \left(\frac{\pi W_k}{2} \cdot a_n^{k,m} \cdot (-j)^n \cdot J_n\left(\frac{\alpha W_k}{2}\right) \cdot e^{-j\alpha x_k} \right) \qquad (4.4)$$

and

$$\tilde{A}_{z,k}(\alpha)=\mu_o\tilde{G}_A(\alpha)\cdot\tilde{J}_{z,k}(\alpha)=\mu_o\sum_n\left(\frac{\pi W_k}{2}\cdot a_n^{k,m}\cdot(-j)^n\cdot\tilde{G}_A(\alpha)\cdot J_n\left(\frac{\alpha W_k}{2}\right)\cdot e^{-j\alpha x_k}\right). \quad (4.5)$$

Here, $J_i(\chi)$ is the Bessel function of the first kind of order *i*, and $a_n^{k,m}$ is the coefficient of the *n-th* basis function representing the current distribution on the *m-th* conductor when the *k-th* conductor excited. Taking the inner product of the basis functions and test functions as $(-j)^i\cdot J_i(\alpha W_m/2)\cdot e^{j\alpha x_m}$, the left-hand side becomes

$$L.S.H=\int_{-\infty}^{\infty}\tilde{A}_{z,k}(\alpha)\cdot(-j)^i\cdot J_i\left(\frac{\alpha W_m}{2}\right)\cdot e^{j\alpha x_m}\cdot d\alpha \quad (4.6)$$

The spatial domain representation of the L.H.S can be obtained using Parseval's theorem.

$$L.H.S=2\pi\frac{2}{\pi W_m}\int_{-x_m-\frac{W_m}{2}}^{-x_m+\frac{W_m}{2}}A_{z,k}(x)\cdot\frac{T_i\left(\frac{2(x+x_m)}{W_m}\right)}{\sqrt{1-\left(\frac{2(x+x_m)}{W_m}\right)^2}}\cdot dx \quad (4.7)$$

Using the properties of the Chebyshev functions, the L.H.S becomes a constant after some simple manipulations as shown the chapter 3.

$$L.H.S=2\Lambda\int_{-1}^{1}\frac{T_i(\chi)}{\sqrt{1-\chi^2}}d\chi=2\Lambda\cdot\begin{cases}\pi & if \quad i=0\\ 0 & Otherwise\end{cases} \quad (4.8)$$

where

$$\frac{2(x+x_m)}{W_m}=\chi,\quad dx=\frac{W_m}{2}d\chi.$$

On the other hand, the R.H.S. becomes

$$R.H.S = \mu_o \sum_n \left(\int_{-\infty}^{\infty} \frac{\pi W_k}{2} \cdot a_n^{k,m} \cdot (-j)^{i+n} \cdot J_i\left(\frac{\alpha W_m}{2}\right) \cdot \tilde{G}_A(\alpha) \cdot J_n\left(\frac{\alpha W_k}{2}\right) \cdot e^{-j\alpha(x_k - x_m)} \cdot d\alpha \right) \quad (4.9)$$

This integration can be simplified if the exponential term representing the spatial distance between the center position of two arbitrary conductors can be divided into even and odd trigonometric terms as follows.

$$R.H.S. =$$

$$\mu_o \sum_n \left(\int_{-\infty}^{\infty} (\bullet) \cdot (-j)^{i+n} \cdot Cos[\alpha(x_k - x_m)] \cdot d\alpha + \int_{-\infty}^{\infty} (\bullet) \cdot (-j)^{i+n+1} \cdot Sin[\alpha(x_k - x_m)] \cdot d\alpha \right) \quad (4.10)$$

where

$$(\bullet) = J_i\left(\frac{\alpha W_m}{2}\right) \cdot \tilde{G}_A(\alpha) \cdot J_n\left(\frac{\alpha W_k}{2}\right) \cdot$$

Note that the Green's function is always an even function. If the orders i and n of the Bessel functions are either even, or both odd numbers, (•) becomes an even function and the second integration term becomes 0. Otherwise, the first integration term becomes 0. Finally, the right-hand side becomes the following form after eliminating the unnecessary terms.

$$R.H.S = \mu_o \sum_n a_n^{k,m} \cdot \pi W_k \int_0^{\infty} J_i\left(\frac{\alpha W_k}{2}\right) \cdot \tilde{G}_A(\alpha) \cdot J_n\left(\frac{\alpha W_m}{2}\right) \cdot P(\alpha)_{i,k,n,m} \cdot d\alpha \quad (4.11)$$

where

$$P(\alpha)_{i,k,n,m} = \begin{cases} Cos[\alpha|x_k - x_m|] & if \quad i+n = even \\ Sin[\alpha|x_k - x_m|] & if \quad i+n = odd \end{cases}.$$

Combining left and right-hand sides together, the linear equations for M coupled lines with (N_f+1) basis functions is written in the following simplified matrix form in order to find the (N_f+1) unknown coefficients by Galerkin's procedure, that is,

$$a_n^{k,m} \cdot \tilde{F}(\alpha)_{i,k,n,m} = \begin{Bmatrix} \dfrac{2\Lambda}{W_k} & if \quad i=0 \\ 0 & Otherwise \end{Bmatrix} \tag{4.12}$$

$$i= 0,1, .. ,N_f, \quad k= 1,2, .. ,M, \quad n= 0,1, .. ,N_f, \quad m= 1,2, .. ,M,.$$

Here

$$\tilde{F}(\alpha)_{i,k,n,m} = \int_0^\infty J_i\left(\frac{\alpha W_k}{2}\right) \cdot \tilde{G}_A(\alpha) \cdot J_n\left(\frac{\alpha W_m}{2}\right) \cdot P(\alpha)_{i,k,n,m} \cdot d\alpha .$$

Each $\tilde{F}(\alpha)_{i,k,n,m}$ becomes $F_{p,q}$ of an $(N_f+1) \times M(N_f+1)$ sized matrix as follows.

$$\mathbf{Fa} = \mathbf{b} \tag{4.13}$$

In (4.13), **a** is the coefficient vector, and **b** is the vector containing the potential. Matrix equation (4.13) is solved as

$$\begin{bmatrix} \begin{bmatrix} a_0^{k,m} \end{bmatrix} \\ \begin{bmatrix} a_1^{k,m} \end{bmatrix} \\ \vdots \\ \begin{bmatrix} a_{N_f}^{k,m} \end{bmatrix} \end{bmatrix} = \begin{bmatrix} F_{0,0} & F_{0,1} & \cdots & F_{0,N} \\ F_{1,0} & F_{1,1} & \cdots & F_{1,N} \\ \vdots & \vdots & \ddots & \vdots \\ F_{N,0} & F_{N,2} & \cdots & F_{N,N} \end{bmatrix}^{-1} \begin{bmatrix} [2\Lambda/W_m\mu_o] \\ [0] \\ \vdots \\ [0] \end{bmatrix} \tag{4.14}$$

where

$$F_{p,q} = \tilde{F}(\alpha)_{i,k,n,m}, \text{ and } p=M\times i+k, \quad q=M\times n+m, \text{ and } N=M(N_f+1).$$

Once the unknown coefficient vector for each current distribution on an arbitrary conductor is calculated, each element of matrix *[K]* and corresponding matrix *[L]* can be readily obtained using the following equation:

$$K_{k,m} = \left.\frac{I_{z,k}}{\Lambda_m}\right|_{\substack{\Lambda_m=1 \\ \Lambda_l=0}} = \sum_{n=0}^{N_f} \left[\int_{x_k-\frac{W_k}{2}}^{x_k+\frac{W_k}{2}} a_n^{k,m} \cdot \frac{T_n\left(\frac{2(x-x_k)}{W_k}\right)}{\sqrt{1-\left(\frac{2(x-x_k)}{W_k}\right)^2}} dx \right] \tag{4.15}$$

with

$$[I_z] = [K][\Lambda]$$

and

$$[L] = [K]^{-1}.$$

The unknown coefficient vector also can be obtained using the approach described in the previous chapter. If the properties of Chebyshev polynomial are used, the dummy matrix *[K]* can be calculated in a similar manner as in the single line inductance case.

$$\therefore K_{k,m} = \frac{T_{k,m}\pi}{\mu_o} \tag{4.16}$$

Once the equivalent capacitance and inductance matrices are calculated, the line mode parameters can be extracted by calculating the eigenvalue of the following characteristic linear equations.

$$[Z][Y] - \gamma^2[U] = \mathbf{0} \quad \text{and} \quad [Z][Y]^{-1} - Z_o^{\,2}[U] = \mathbf{0} \tag{4.17}$$

where

$$[Z] = [R] + j\omega[L], \quad [Y] = [G] + j\omega[C] \text{ and } [U] = \text{Unitary Matrix.}$$

The solution yields M line mode parameter vectors, $[\gamma]_{M\times 1} = [\alpha + j\beta]_{M\times 1}$ and $[Z_o]_{M\times 1}$ for M conductors over a ground plane.

- Examples

As a first case of multiple coupled interconnects, an asymmetric coupled transmission line on a heavily doped silicon substrate is considered. The coupled line parameters are shown in Figure 4.3 as a function of frequency. Calculated line parameters for the c and π mode by a full-wave simulator HP/Momentum® are also plotted in this figure together with the simulation results from the new modeling approach. As frequency increases, attenuation and wave velocity increase, similar to the single line case. In the π mode (mode 2) both conductors are excited with opposite polarities and most of the field around the strips is concentrated in the oxide layer between the conducting strips at which the relative permittivity and conductivity are very small compared to the silicon layer. In this case, the oxide layer dominates the propagation characteristics. On the other hand, excited potentials with same polarity in the c mode (mode 1) force the fields to penetrate deeply into the substrate, and the silicon layer dominates the propagation characteristics. Figures 4.4 and 4.5 illustrate the propagation characteristics for three and four line cases, respectively. In general, the line parameters extracted from the scattering matrix generated by HP/Momentum® are in good agreement with the results obtained with the electric and magnetic potential–based quasi-static SDM.

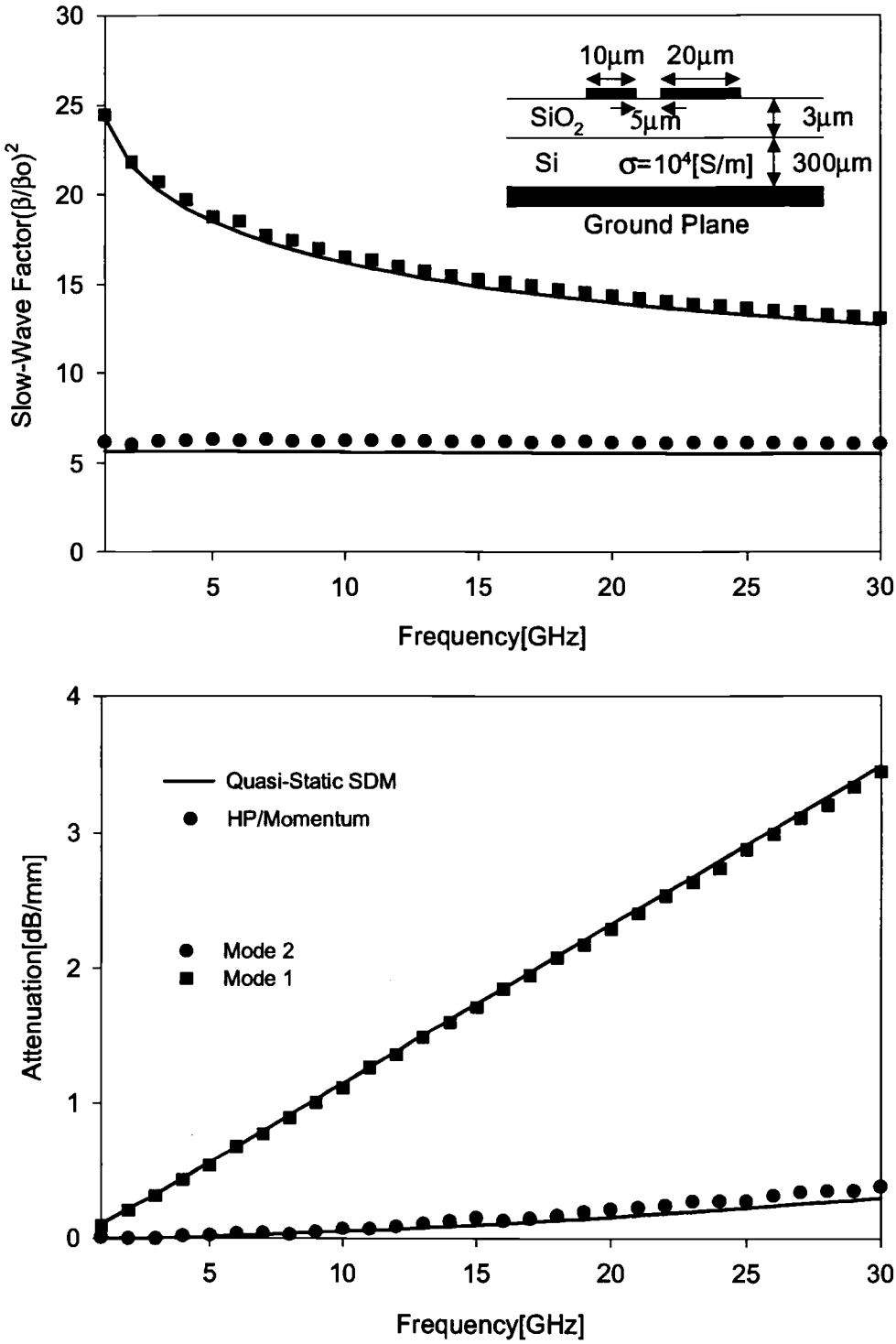

Figure 4.3 Line parameters of a single level, two coupled line structure calculated by quasi-static SDM and HP/Momentum®.

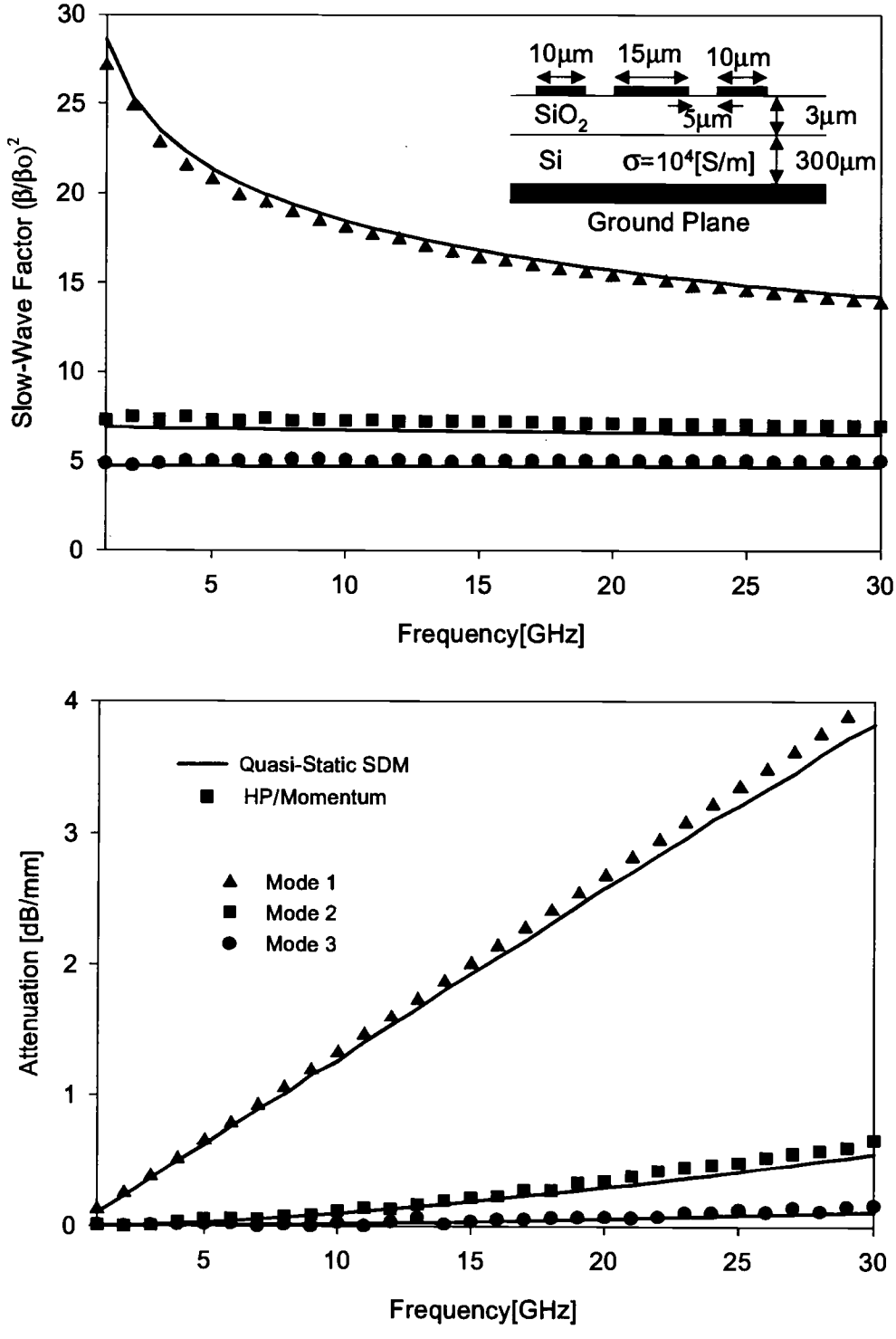

Figure 4.4 Line parameters of a single level, three coupled line structure calculated by quasi-static SDM and HP/Momentum®.

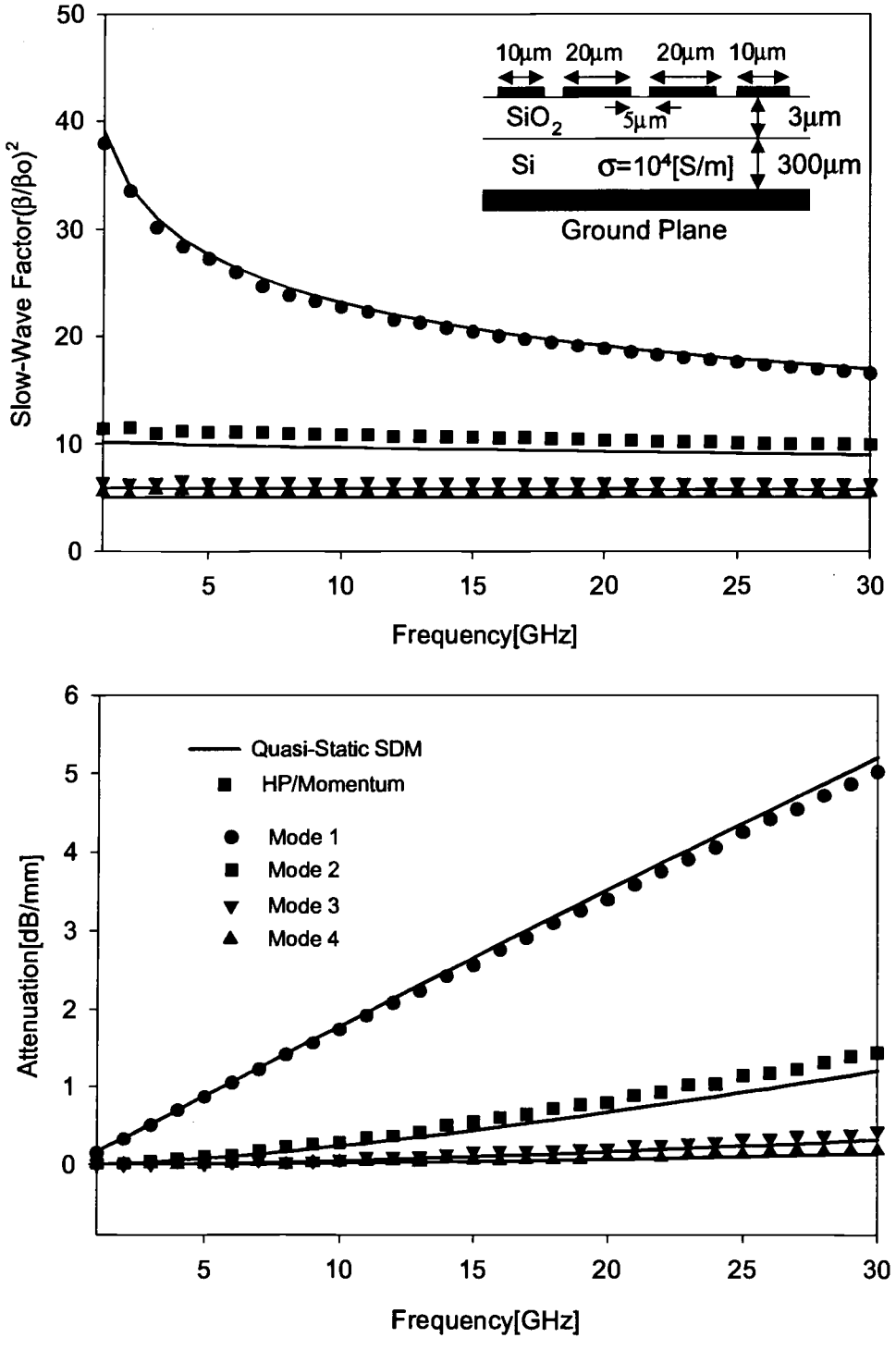

Figure 4.5 Line parameters of a single level, four coupled line structure calculated by quasi-static SDM and HP/Momentum®.

4.3 Multilevel, Multiple Coupled Interconnects

Multiple coupled, multilevel interconnects are more common structures used in current MMIC's and RFIC's. Unlike the microstrip lines as edge-couplers, multileveled conductors have tighter coupling if the interconnects are fabricated in the same direction (broadside coupled). In most cases, these broadside-coupled configurations are more common in MMIC applications and need rigorous analysis due to the complicated coupling effects.

As shown in Figure 4.6, all the conductors are coupled to each other in both horizontally and vertically. Modeling this configuration can be achieved by formulating the relations between all the source positions by a Green's function given in a matrix form.

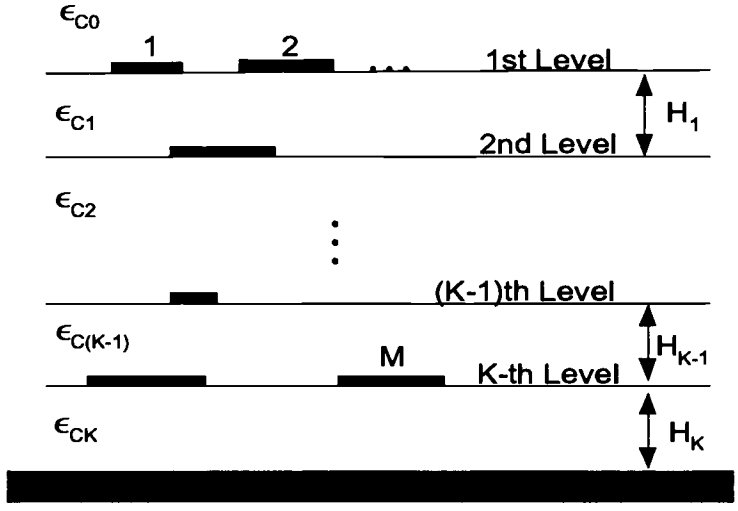

Figure 4.6 General multilevel, multiconductor structure

- Calculation Approach

Since the Green's function only characterizes the vertical source positions, the Green's function is given in $k \times k$ sized matrix form if k levels of conductor are present.

The electric or magnetic potential based Green's function matrix, $\tilde{G}^{o}_{\phi,A}(\alpha)$, quantifying the relations between the layers is found by inverting the matrix composed of input admittance seen at each conductor layer. First, the electric potential based Green's function matrix is found by a similar approach as described in Appendix 11.

$$\left[\tilde{\rho}^{o}\right]_{K\times 1} = \left[\tilde{Y}^{o,\phi}\right]_{K\times K}\left[\tilde{\phi}^{o}\right]_{K\times 1} \tag{4.18}$$

where

$$\left[\tilde{Y}^{o,\phi}\right]^{-1} = \left[\tilde{G}^{o,\phi}\right].$$

Here, the admittance matrix form is given as

$$\left[\tilde{Y}^{o,\phi}\right] = \begin{bmatrix} \tilde{Y}^{\phi}{}_{1,1}(\alpha) & \tilde{Y}^{\phi}{}_{1,2}(\alpha) & 0 & \cdots & 0 \\ \tilde{Y}^{\phi}{}_{2,1}(\alpha) & \tilde{Y}^{\phi}{}_{2,2}(\alpha) & \tilde{Y}^{\phi}{}_{2,3}(\alpha) & \ddots & \vdots \\ 0 & \ddots & \ddots & \ddots & 0 \\ \vdots & \ddots & \tilde{Y}^{\phi}{}_{K-1,K-2}(\alpha) & \tilde{Y}^{\phi}{}_{K-1,K-1}(\alpha) & \tilde{Y}^{\phi}{}_{K-1,K}(\alpha) \\ 0 & \cdots & 0 & \tilde{Y}^{\phi}{}_{K,K-1}(\alpha) & \tilde{Y}^{\phi}{}_{K,K}(\alpha) \end{bmatrix} \tag{4.19}$$

where each element can be obtained using the following equations:

$$\tilde{Y}^{\phi}_{1,1}(\alpha) = \tilde{Y}^{\phi}_{U}(\alpha) + |\alpha|\varepsilon_{C1}Coth(|\alpha|\cdot H_1),\ \tilde{Y}^{\phi}_{U}(\alpha) = |\alpha|\varepsilon_{C0} \tag{4.20}$$

$$\tilde{Y}^{\phi}_{K,K}(\alpha) = \tilde{Y}^{\phi}_{L}(\alpha) + |\alpha|\varepsilon_{C(K-1)}Coth(|\alpha|\cdot H_{K-1}),\ \tilde{Y}^{\phi}_{L}(\alpha) = |\alpha|\varepsilon_{CK}Coth(|\alpha|\cdot H_K) \tag{4.21}$$

$$Y^{\phi}_{i,i}(\alpha) = |\alpha|\varepsilon_{Ci}\cdot Coth(|\alpha|\cdot H_i) + |\alpha|\varepsilon_{C(i-1)}\cdot Coth(|\alpha|\cdot H_{i-1}) \tag{4.22}$$

$$\tilde{Y}^{\phi}_{i,i-1}(\alpha) = \tilde{Y}^{\phi}_{i-1,i}(\alpha) = \frac{-|\alpha|\varepsilon_{Ci}}{Sinh(|\alpha|\cdot H_i)} \tag{4.23}$$

Similarly, the magnetic potential based Green's function matrix can be written as

$$\left[\tilde{J}_z^O\right]_{K\times 1} = \left[\tilde{Y}^{O,A}\right]_{K\times K}\left[\tilde{A}_z^O\right]_{K\times 1} \tag{4.24}$$

where

$$\left[\tilde{Y}^{O,A}\right]^{-1} = \left[\tilde{G}^{O,A}\right].$$

Also, the admittance matrix becomes

$$\left[\tilde{Y}^{O,A}\right] = \begin{bmatrix} \tilde{Y}^A_{1,1}(\alpha) & \tilde{Y}^A_{1,2}(\alpha) & 0 & \cdots & 0 \\ \tilde{Y}^A_{2,1}(\alpha) & \tilde{Y}^A_{2,2}(\alpha) & \tilde{Y}^A_{2,3}(\alpha) & \ddots & \vdots \\ 0 & \ddots & \ddots & \ddots & 0 \\ \vdots & \ddots & \tilde{Y}^A_{K-1,K-2}(\alpha) & \tilde{Y}^A_{K-1,K-1}(\alpha) & \tilde{Y}^A_{K-1,K}(\alpha) \\ 0 & \cdots & 0 & \tilde{Y}^A_{K,K-1}(\alpha) & \tilde{Y}^A_{K,K}(\alpha) \end{bmatrix}. \tag{4.25}$$

For calculating each element, the following equations are used.

$$\tilde{Y}^A_{1,1}(\alpha) = \tilde{Y}^A_U(\alpha) + \alpha_1 Coth(\alpha_1 \cdot H_1), \quad \tilde{Y}^A_U(\alpha) = \alpha_0 \tag{4.26}$$

$$\tilde{Y}^A_{K,K}(\alpha) = \tilde{Y}^A_L(\alpha) + \alpha_K Coth(\alpha_K \cdot H_K), \quad \tilde{Y}^A_L(\alpha) = \alpha_K Coth(\alpha_K \cdot H_K) \tag{4.27}$$

$$Y^A_{i,i}(\alpha) = \alpha_i \cdot Coth(\alpha_i \cdot H_i) + \alpha_{i-1} \cdot Coth(\alpha_{i-1} \cdot H_{i-1}) \tag{4.28}$$

$$\tilde{Y}^A_{i,i-1}(\alpha) = \tilde{Y}^A_{i-1,i}(\alpha) = \frac{-\alpha_i}{Sinh(\alpha_i \cdot H_i)} \quad \text{and} \quad \alpha_i = \sqrt{\alpha^2 + j\omega\sigma_i} \tag{4.29}$$

Here, $\tilde{Y}^{p,q}_{\phi,A}(\alpha)$ is the input admittance seen from the *p-th* layer to the *q-th* layer

As the next step, the Green's function matrix is expanded to ($M\times M$) size to represent the interaction between all of the conductors including the horizontal distances between the interconnects, as shown in the following figure.

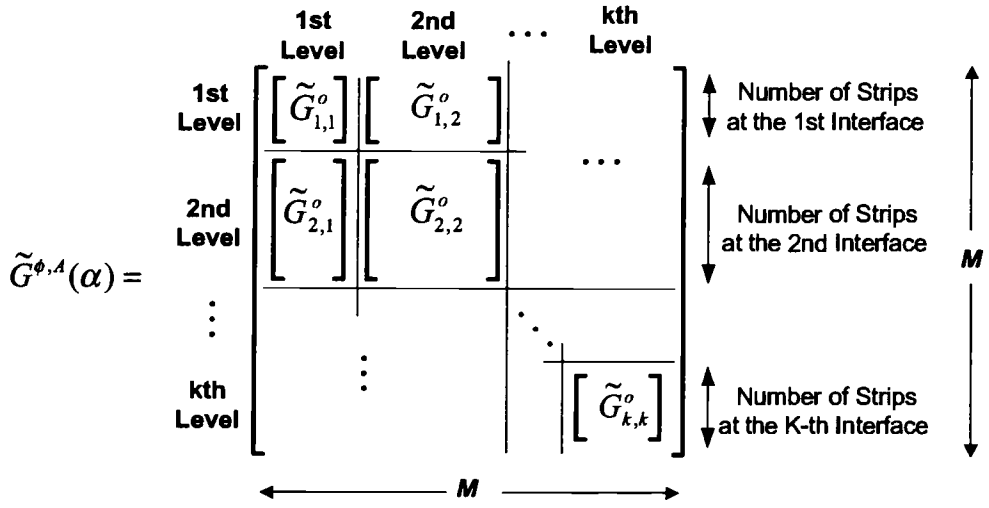

Figure 4.7 Final Green's function matrix representing multilevel, multiconductor structure

In order to form the final system equation for calculating the unknown coefficient matrix, each element is given as

$$\tilde{F}(\alpha)_{i,k,n,m} = \int_0^{\infty} J_i\left(\frac{\alpha W_k}{2}\right) \cdot \tilde{G}_{k,m}(\alpha) \cdot J_n\left(\frac{\alpha W_m}{2}\right) \cdot P(\alpha)_{i,k,n,m} \cdot d\alpha \qquad (4.30)$$

The linear equation given in (4,13) is directly solve for the unknown coefficient vector, ***a***.

- Examples

Using the modeling technique for multilevel planar transmission line structures, line parameters of two level, two, three, and four coupled conductor cases are calculated and depicted in Figures 4.8~10 as well as compared with HP/Momentum® simulations.

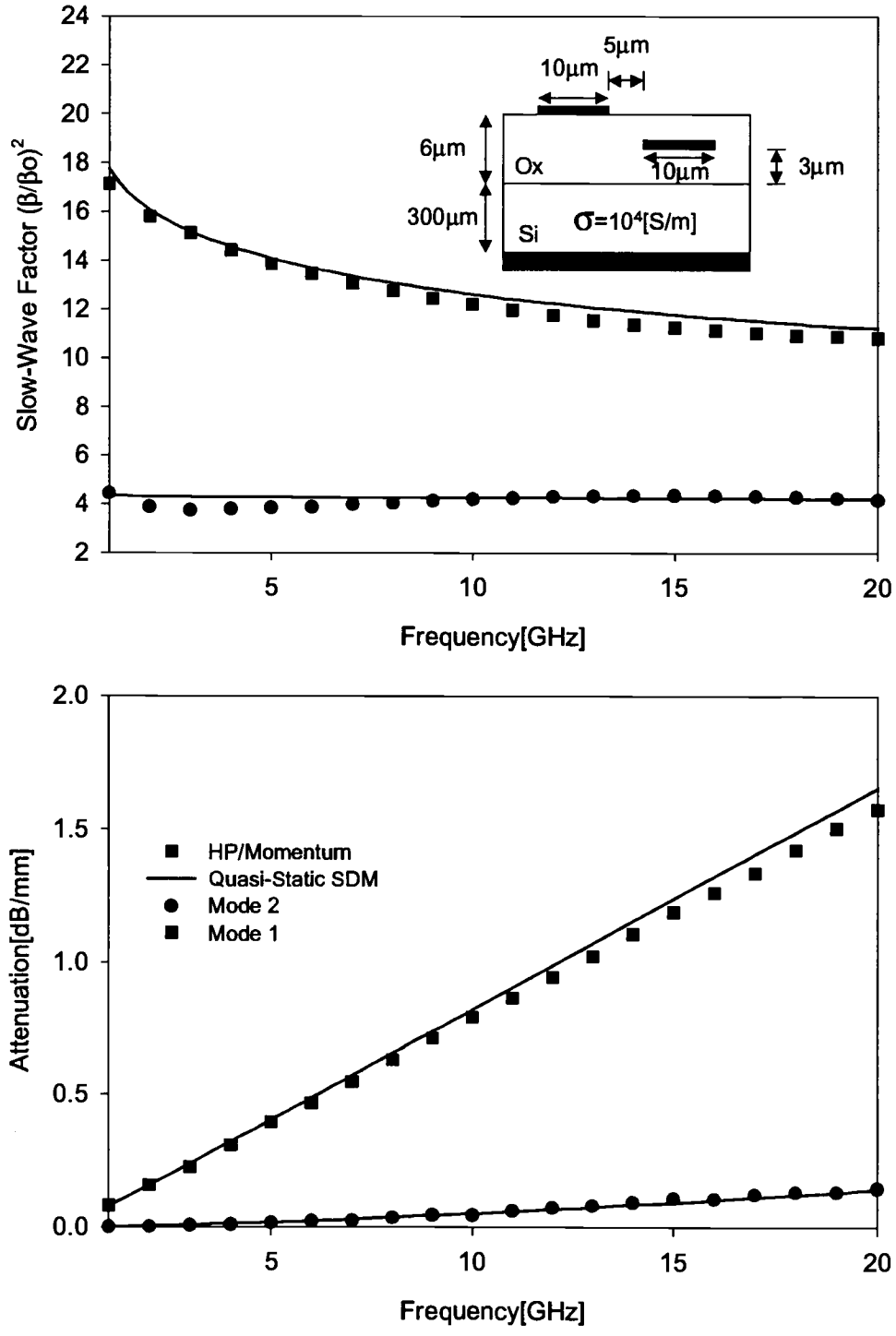

Figure 4.8 Line parameters of a two level, two coupled line structure calculated by quasi-static SDM and HP/Momentum®

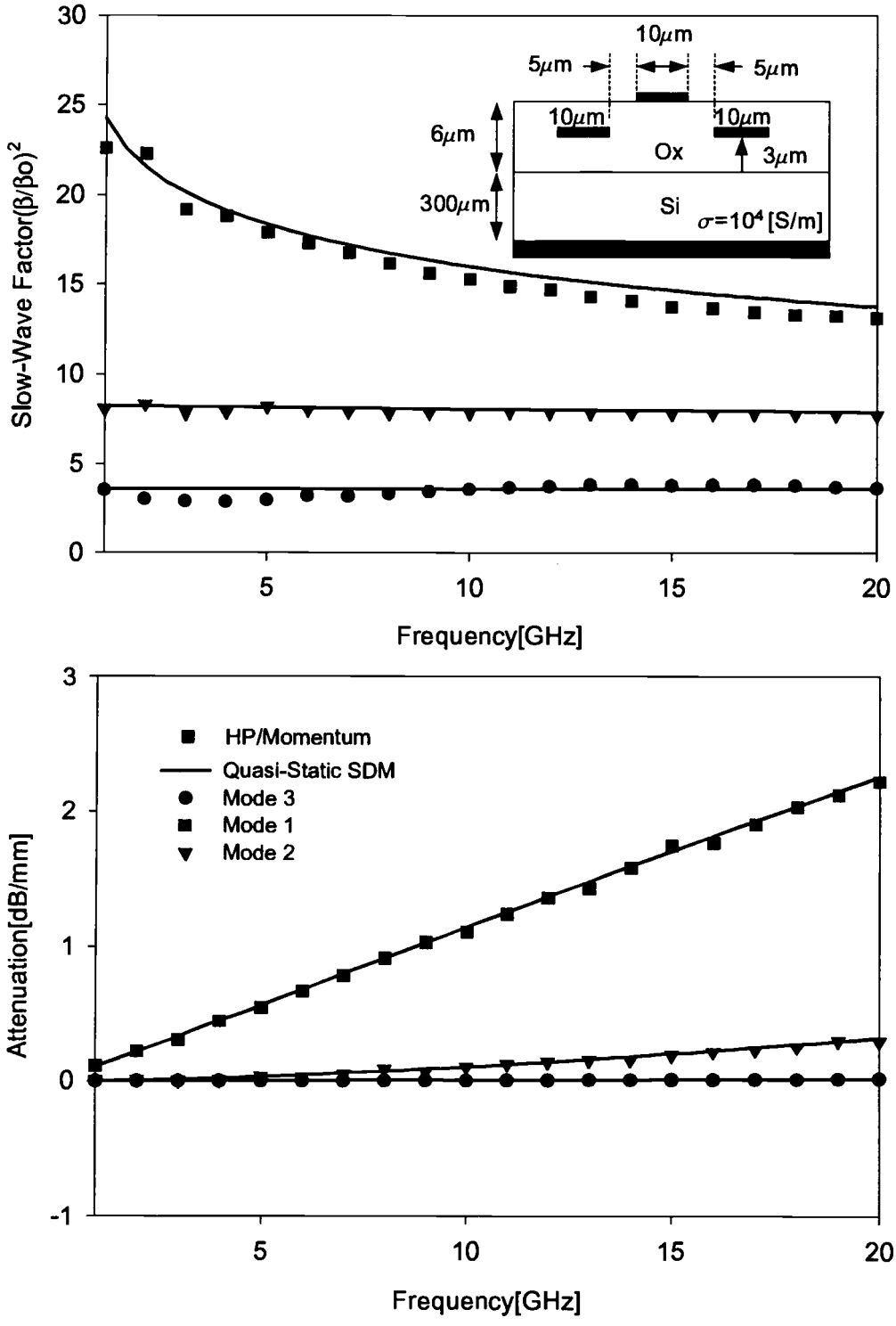

Figure 4.9 Line parameters of a two level, three coupled line structure calculated by quasi-static SDM and HP/Momentum®

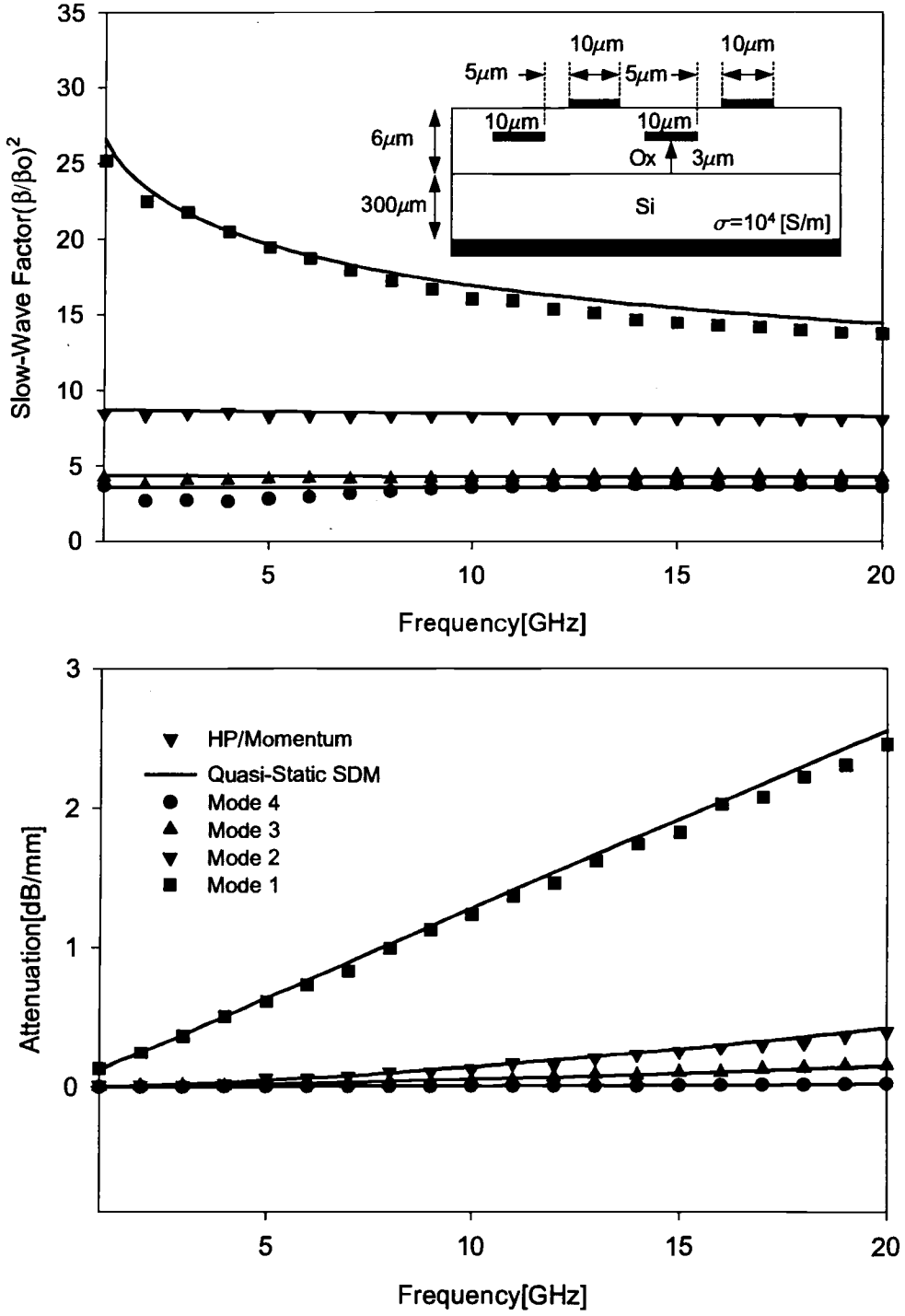

Figure 4.10 Line parameters of a two level, four coupled line structure calculated by quasi-static SDM and HP/Momentum®

For the two-line case illustrated in Figure 4.8, the field distribution is rather different from that of the single level case in Figure 4.3. Since one of the conducting strips is embedded in the oxide layer, more fields are condensed at the oxide layer between the conductors in contrast to the single level structure, even for the same polarity of excitation. Thus, the wave velocity does not change as much as in the former case. A similar behavior occurs for three and four line cases with less attenuation compared with the single microstrip case. For all cases, the solutions obtained with the proposed method are in good agreement with the full-wave solutions.

4.4 Interconnects with Finite Thickness

In the previous section, the interconnect thickness was assumed to be zero. With decreasing conductor width, however, the finite thickness of the conductor becomes significant and cannot be ignored. This is especially of concern for VLSI circuits where for narrow interconnects, the thickness is about as large as the interconnect width, or even larger. In general, a thick conductor with finite conductivity itself has a complicated loss behavior including the conductor skin effect and proximity effects. Thus, calculating the conductor loss is another important issue, and has been studied by various full-wave and/or quasi-static techniques [22~23]. Currently, some chip manufacturers are trying to fabricate the circuits with high-conductivity materials such as copper in order to reduce the conductor loss [3].

In this thesis, the effects of finite matallization thickness for an ideal conductor are the main focus and are analyzed in terms of capacitance and inductance. Once accurate L and C parameters are calculated, the conductor loss can be estimated with various quasi-static or empirical methods and added to the contributions to the substrate skin effect.

If the conductor has finite thickness, more electric charge and current are accumulated at the surface compared to an infinitesimally thin conductor. This results in changes in the capacitance and inductance values. In order to take into account the matallization thickness effects, Kollipara and Tripathi [20] introduced an effective and accurate modeling technique using a stacked conductor model.

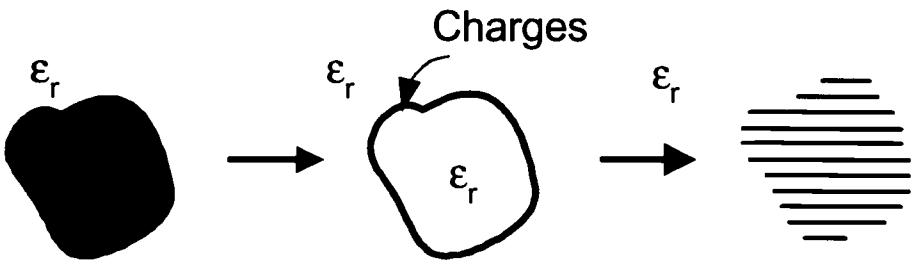

Figure 4.11 Arbitrary shaped conductor cross section and its stacked model

The main idea of this approach is that all of the electric charges are accumulating on the outer shell of the conductor if the conductivity is infinity. Therefore, the arbitrary cross sectional shape of a conductor can be equivalently replaced with an adequate number of infinitesimally thin multiple stacked conductors, as shown in Figure 4.11. Since the electric potentials of all the stacked conductors are the same and the distance between adjacent conductors is very small, most of the charges are populated at the edges of each stacked conductor except for the top and the bottom ones.

Technically, the Green's function matrix for this model can be modified from the multilayered conductor structure explained in the previous section. However, this modeling process is more complicated if the conductor is considered as a function of thickness since it is difficult to decide how many conductors should be stacked for a given thickness. The most accurate way is setting the number of conductors to as many as possible, thus a Green's function matrix of large dimensions is obtained, and the computation becomes more complicated than that of the lossy substrate problem.

This section proposes a simple strategy that greatly reduces the matrix size based on the following assumptions. First, the cross section of the conductor is rectangular. That is, all the stacked conductors have the same width, and the corresponding arguments of the basis functions used in Galerkin's procedure are also the same. Second, the distances between the stacked conductors are all the same so that the Green's function matrix does not have too many different height terms. This strategy drastically reduces the entire formulation. That is, the Green's function matrix becomes a single equation since the stacked conductors can be regarded as a single conductor.

- Calculating Approach

As described above, the admittance matrix for the stacked conductor structure can be obtained by calculating input admittance elements seen at each conductor. In Figure 4.12, a conductor with finite thickness and rectangular cross section is modeled with *(N+1)* stacked conducting strips.

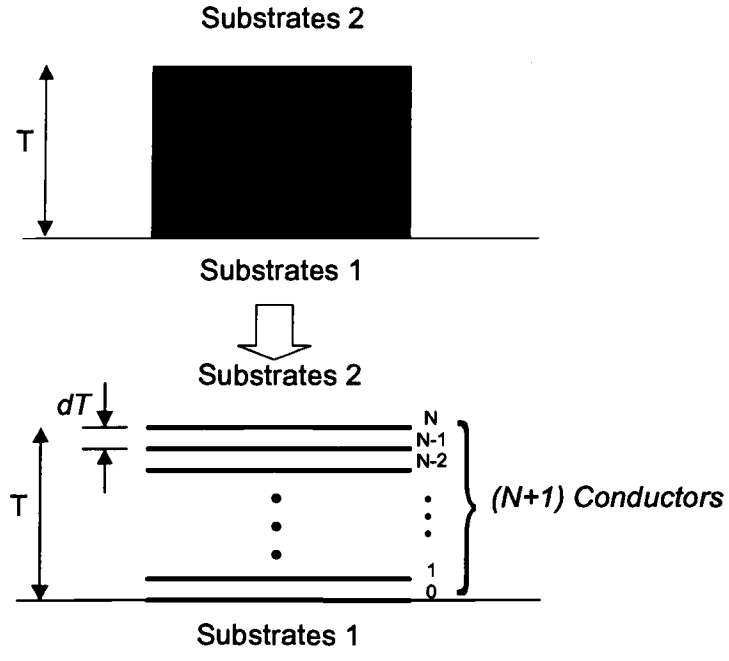

Figure 4.12 Rectangular conductor cross section and its stacked conductor model

For capacitance calculation, the set of linear equations in terms of input admittance matrix and potential is given as

$$\begin{bmatrix} \tilde{\rho}_N(\alpha) \\ \tilde{\rho}_{N-1}(\alpha) \\ \vdots \\ \tilde{\rho}_1(\alpha) \\ \tilde{\rho}_0(\alpha) \end{bmatrix} = \begin{bmatrix} \tilde{Y}^{\phi}{}_{N,N}(\alpha) & \tilde{Y}^{\phi}{}_{N,N-1}(\alpha) & 0 & \cdots & 0 \\ \tilde{Y}^{\phi}{}_{N-1,N}(\alpha) & \tilde{Y}^{\phi}{}_{N-1,N-1}(\alpha) & \tilde{Y}^{\phi}{}_{N-1,N-2}(\alpha) & \ddots & \vdots \\ 0 & \ddots & \ddots & \ddots & 0 \\ \vdots & \ddots & \tilde{Y}^{\phi}{}_{1,2}(\alpha) & \tilde{Y}^{\phi}{}_{1,1}(\alpha) & \tilde{Y}^{\phi}{}_{1,0}(\alpha) \\ 0 & \cdots & 0 & \tilde{Y}^{\phi}{}_{0,1}(\alpha) & \tilde{Y}^{\phi}{}_{0,0}(\alpha) \end{bmatrix} \begin{bmatrix} \tilde{\phi}_N(\alpha) \\ \tilde{\phi}_{N-1}(\alpha) \\ \vdots \\ \tilde{\phi}_1(\alpha) \\ \tilde{\phi}_0(\alpha) \end{bmatrix} \quad (4.31)$$

where

$$\tilde{Y}^{\phi}{}_{0,0}(\alpha) = \tilde{Y}_L^{\phi}(\alpha) + |\alpha|\varepsilon_o\varepsilon_r Coth(|\alpha| \cdot dT) \quad (4.32)$$

$$\tilde{Y}^{\phi}{}_{N,N}(\alpha) = \tilde{Y}_U^{\phi}(\alpha) + |\alpha|\varepsilon_o\varepsilon_r Coth(|\alpha| \cdot dT) \quad (4.33)$$

$$\tilde{Y}_{i,i}(\alpha) = |\alpha|\varepsilon_o\varepsilon_r \left(Coth(|\alpha| \cdot dT) + Coth(|\alpha| \cdot dT)\right) = 2|\alpha|\varepsilon_o\varepsilon_r Coth(|\alpha| \cdot dT) \quad (4.34)$$

$$\tilde{Y}_{i,i-1}(\alpha) = \tilde{Y}_{i-1,i}(\alpha) = \frac{-|\alpha|\varepsilon_o\varepsilon_r}{Sinh(|\alpha| \cdot dT)} \quad (4.35)$$

If the thick conductor has an arbitrary cross section of shape, it is desired to compute the entire matrix written above to apply to Galerkin's procedure. However, if we assume that the shape of the conductor cross section is rectangular, the procedure can be drastically simplified. That is, we are only interested in the total accumulated charges of the conductor group, and not the total charge on each of the thin conductors. In addition, all of the thin conductors of the stacked model are at the same electric potential (i.e., $\tilde{\rho}_{Total} = \tilde{\rho}_0 + \tilde{\rho}_1 + \cdots + \tilde{\rho}_N$ and $\tilde{\phi}_0 = \tilde{\phi}_1 = \cdots = \tilde{\phi}_N = \tilde{\phi}$). This approach changes the admittance matrix above into a simpler form which can be written as

$$\tilde{\rho}_{Total}(\alpha) = \left[\tilde{Y}_L^{\phi}(\alpha) + \tilde{Y}_U^{\phi}(\alpha) + N \cdot \frac{-2|\alpha|\varepsilon_o\varepsilon_r}{Sinh(|\alpha| \cdot dT)} + N \cdot 2|\alpha|\varepsilon_o\varepsilon_r Coth(|\alpha| \cdot dT)\right] \cdot \tilde{\phi}(\alpha) \quad (4.36)$$

or

$$\tilde{Y}_{IN}^{\phi}(\alpha) = \tilde{Y}_L^{\phi}(\alpha) + \tilde{Y}_U^{\phi}(\alpha) + 2N \cdot |\alpha|\varepsilon_o\varepsilon_r \left(Coth(|\alpha| \cdot dT) - \frac{1}{Sinh(|\alpha| \cdot dT)} \right). \quad (4.37)$$

Since the admittance matrix changed into a single value, the size of the linear equation matrix in Galerkin's procedure also can be reduced.

Equivalently, this equation can be generalized for a conductor with finite thickness as shown in the Figure 4.13.

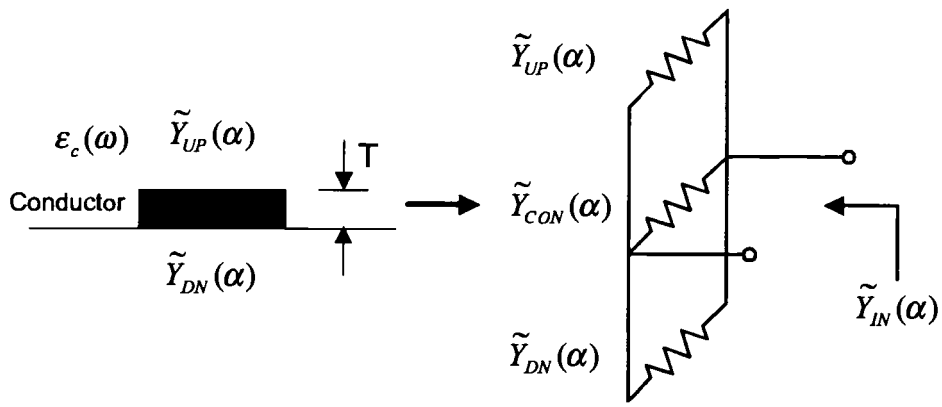

Figure 4.13 Equivalent input admittance of a thick conductor in α domain

The input admittance for capacitance calculation is obtained as

$$\tilde{Y}_{IN}(\alpha) = \tilde{Y}_{UP}(\alpha) + \tilde{Y}_{DN}(\alpha) + \tilde{Y}_{CON}(\alpha)$$

$$= \tilde{Y}_{L}^{\phi,A}(\alpha) + \tilde{Y}_{U}^{\phi,A}(\alpha) + \tilde{Y}_{CON}^{\phi,A}(\alpha) \qquad (4.38)$$

which results in

$$\tilde{Y}_{CON}^{\phi}(\alpha) = 2N \cdot |\alpha| \varepsilon_o \varepsilon_r \left(Coth(|\alpha| \cdot dT) - \frac{1}{Sinh(|\alpha| \cdot dT)} \right). \qquad (4.39)$$

Using a similar approach, the input admittance of a thick conductor for inductance calculation can be derived as

$$\tilde{Y}_{CON}^{A}(\alpha) = 2N \cdot \alpha_C \left(Coth(\alpha_C \cdot dT) - \frac{1}{Sinh(\alpha_C \cdot dT)} \right) \qquad (4.40)$$

with

$$\alpha_C = \sqrt{\alpha^2 + j\omega\mu_o\mu_r\sigma}\,.$$

Here, T_N is the number of stacked conductors and dT is the gap between the stacked conductors($=T/N$).

- Examples

The effects of the conductor thickness on the interconnect characteristics are considered and plotted in Figures 4.14 and 4.15. Here, the substrate is assumed to be lossless to examine the effects from the conductor only. Figure 4.14 shows the line capacitance, inductance and characteristic impedance calculated by this method as a function of conductor thickness. As the conductor becomes thicker, the total charge and current increase, and the characteristic impedance decreases. This change is very close to the result obtained with the commercial quasi-static solver HP/LineCalc®.

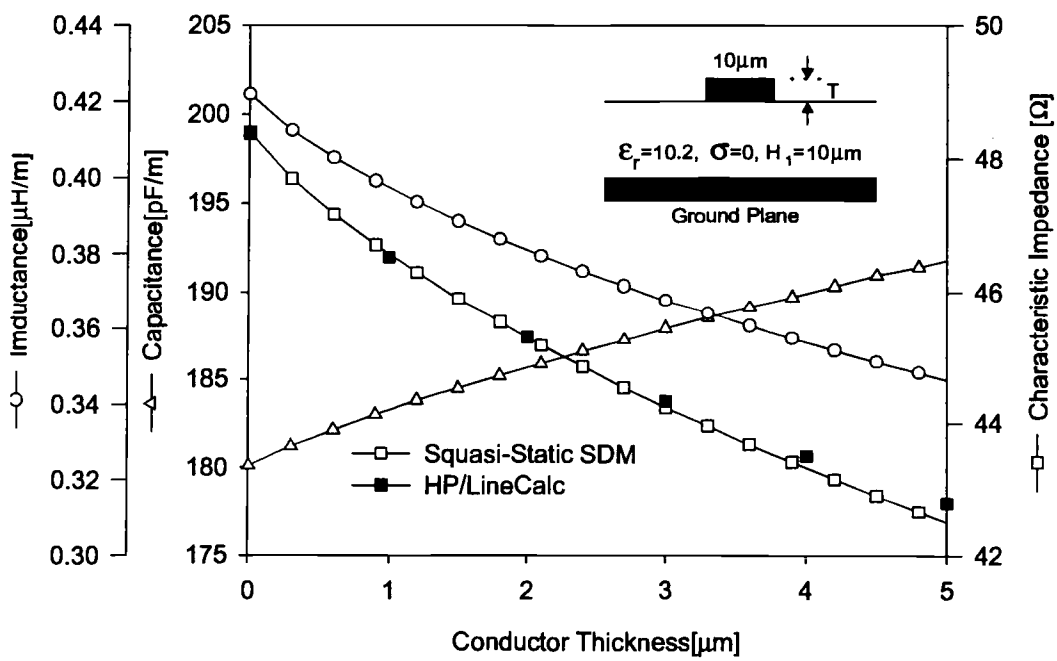

Figure 4.14 Changes in C, L and Zo as a function of conductor thickness @1GHz

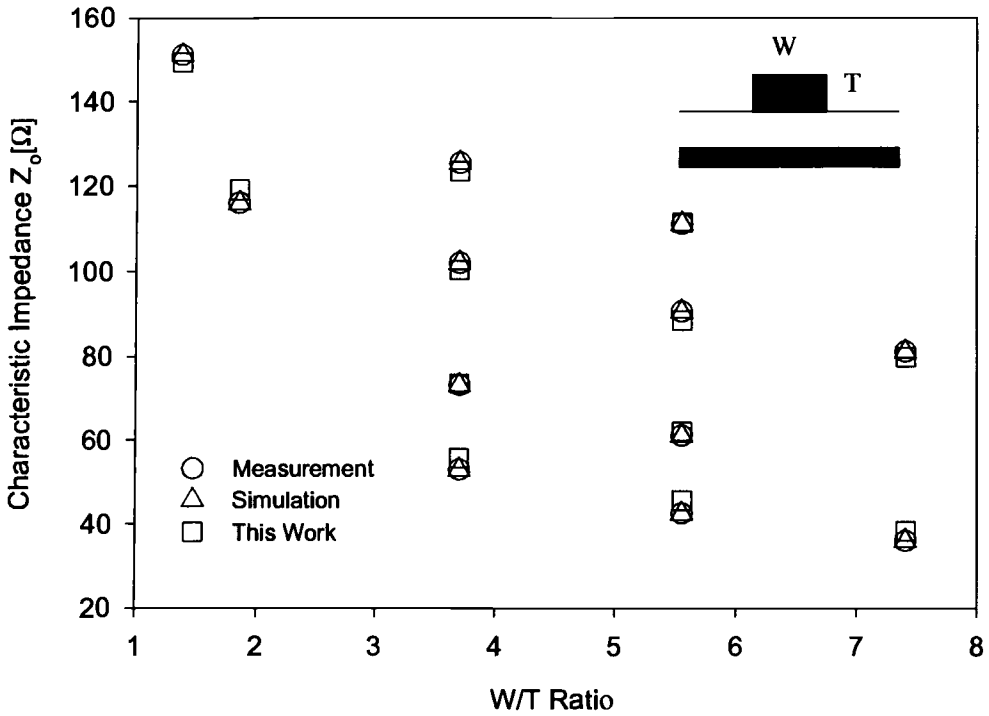

Figure 4.15 Calculated characteristic impedance for various conductor thickness

In order to show the accuracy of this approach, the characteristic impedances of various conductor cases with different W/T (width to thickness) ratios are calculated and compared with other published data and measurements as shown in Figure 4.15. Since the test structures are all different cases, the characteristic impedances are marked with unsorted order in Figure 4.15. It can be seen that the results for each group composed of data from measurements, the technique proposed in [21] and this work are very close to each other.

As seen in the simulation results depicted in Figures 4.14 and 4.15, except for skin effect associated with the operating frequency, all the effects of the finite conductor thickness are sufficiently taken into account during the parameter calculation. In general, this method can be applied to most structures when the conductor thickness and frequency are not too high.

4.5 CAD-Oriented Modeling of Interconnect with Finite Length

Once the distributed line parameters are obtained, on-chip interconnect structures of finite length can be simulated. However, since the line parameters are frequency-dependent the implementation of the model in general simulator environments are difficult or, in some cases, impossible. Therefore, it is advantageous to represent the frequency-dependent parameters in terms of a lumped element circuit with ideal (fixed) element values. Such a CAD-oriented circuit can be directly implemented in general simulators including Spice to simulate the broadband characteristics of the interconnect structure. A general-purpose CAD model for a single MIS transmission line has been developed in [26] and is shown in Fig. 4.16.

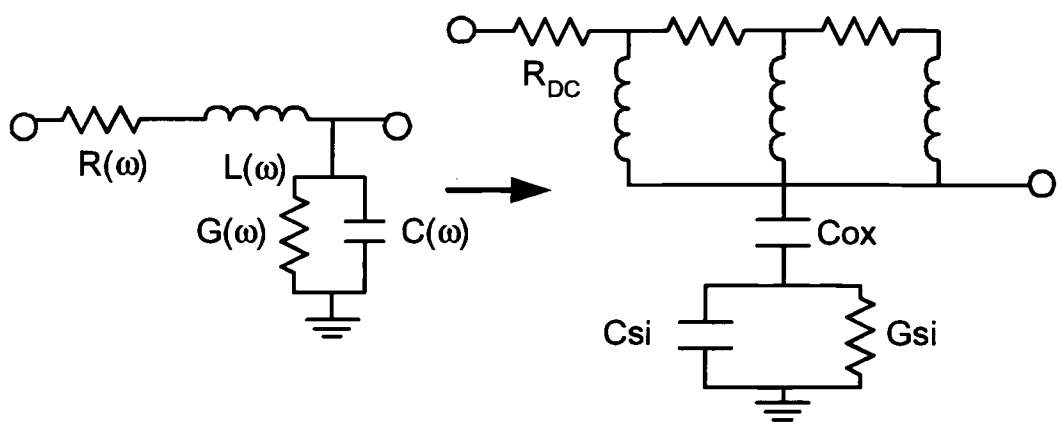

Figure 4.16 Frequency-dependent equivalent circuit and its CAD model for a single interconnect on Si-SiO_2

The three shunt elements (C_{Ox}, C_{Si} and G_{Si}) in this equivalent circuit can be extracted from the frequency-dependent shunt admittance $Y(\omega)=G(\omega)+j\omega C(\omega)$ at one frequency by taking into account the additional relationship

$$C_{eq}(\omega) = C(\omega) + \frac{G(\omega)}{j\omega} = \frac{C_{OX} \cdot \left(C_{Si} + \frac{G_{Si}}{j\omega} \right)}{C_{OX} + C_{Si} + \frac{G_{Si}}{j\omega}} \qquad (4.41)$$

with the relation

$$\frac{G_{Si}}{C_{Si}} = \frac{\sigma_{Si}}{\varepsilon_{Si}}.$$

The equivalent circuit for the p.u.l. series impedance $Z(\omega)=R(\omega)+j\omega L(\omega)$ is derived by constructing a realizable rational polynomial approximation of the general form [67]:

$$F(j\omega) = \frac{A_0 + A_1(j\omega) + A_2(j\omega)^2 + \cdots + A_m(j\omega)^m}{1 + B_1(j\omega) + B_2(j\omega)^2 + \cdots + B_n(j\omega)^n} \qquad (4.42)$$

The rational polynomial function is synthesized in terms of ideal R and L elements in a ladder-type canonical topology [67].

The ideal element equivalent circuit models for single and coupled interconnects have been implemented in Spice. Figure 4.17 shows the step response of a single interconnect when the full frequency-dependence of the transmission line parameter is taken into account. Also shown are the results for the corresponding distributed constant value *RC* and *RLGC* models. It is seen that the frequency-independent models give an inaccurate approximation of the step response.

As a second example, an asymmetric coupled line structure is simulated. The near-end, far-end and through port voltage waveforms are shown in Fig. 4.18. The results obtained by the Spice simulation are in excellent agreement with the solution obtained by direct convolution.

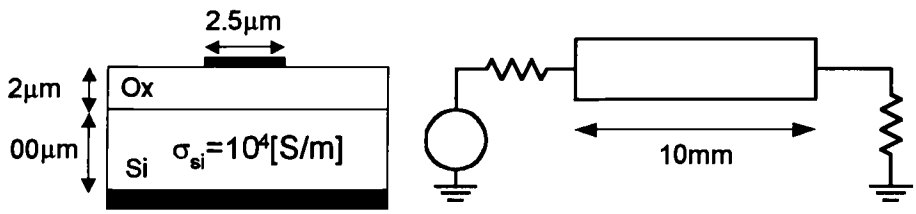

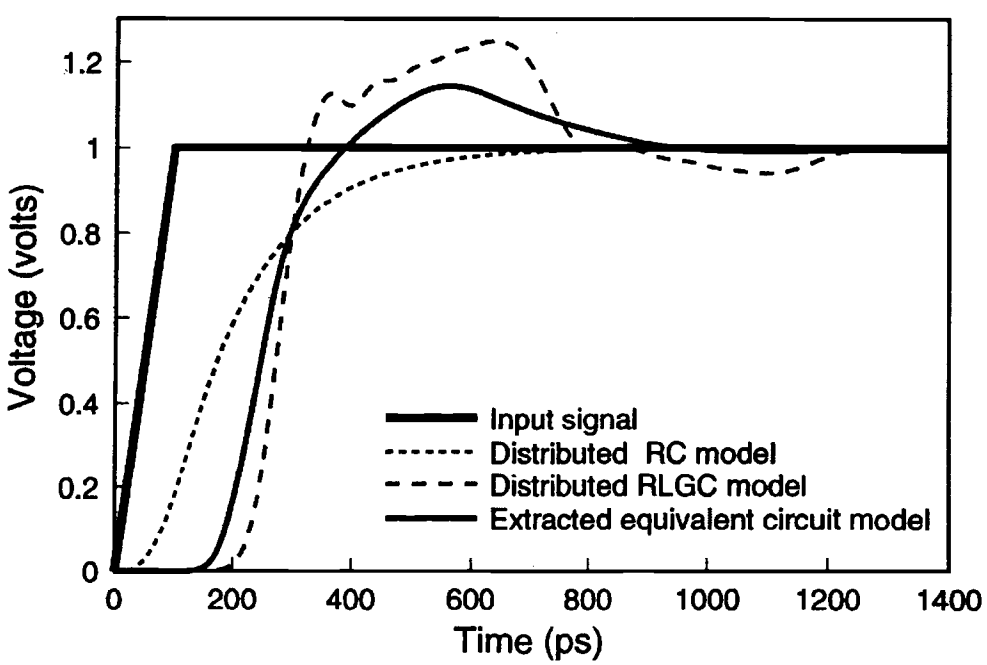

Figure 4.17 Simulation of step response for a single interconnect

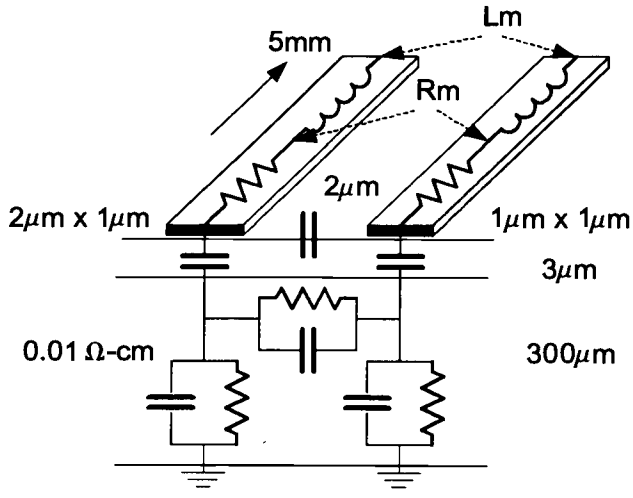

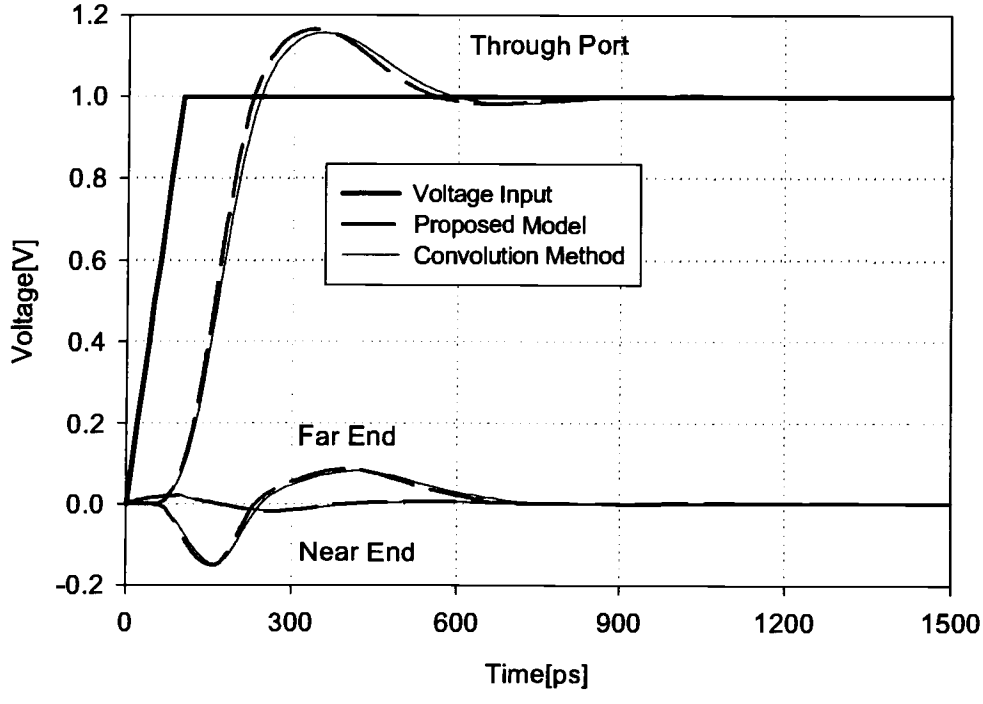

Figure 4.18 Simulation of step response of the equivalent circuit model for an asymmetric coupled interconnect structure and comparison with direct convolution.

4.6 Conclusion

In this chapter, the quasi-static modeling approach has been extended to multiple coupled lines on single and multiple metallization levels. This approach can be extended to characterize the structures without conductor at the interface of the media (see Appendix 12). The technique has also been extended to include the effects of finite conductor thickness. The conductor loss including conductor skin effect has been determined separately and added to the distributed series resistance due to the substrate loss. Finally, the transmission line model has been implemented in Spice, and the broadband step response of a single and coupled line structure have been simulated.

5 MULTICONDUCTOR STRUCTURES WITHOUT GROUND PLANE

5.1 Introduction

IC technologies of today suffer from various problems due to the interconnects such as delay time, radiation effects and heat [27]. One possible structure solving these problems can be made by placing the ground conductors close to the signal lines as shown in the Figure 5.1, thus, the signal interconnects can be conveniently referenced by closely located ground lines. This is also a common structure in current VLSI technology.

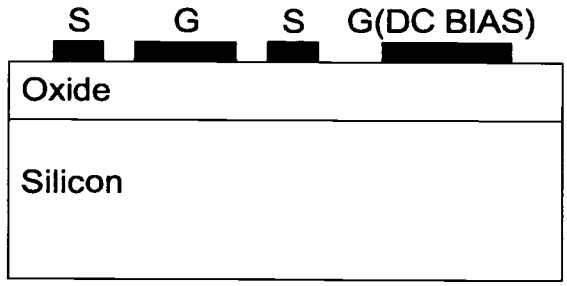

Figure 5.1 Signal-ground paired interconnects without bottom ground plane

The coupling effects are composed of mutual terms between the lines without having any effect from the bottom ground plane, unlike the strictures in the previous chapters. Thus, this configuration provides less delay time as well as higher circuit density on a given area.

Modeling of signal-ground interconnects can be achieved by placing the ground plane at the bottom at infinity (or, virtually removing) in the previous microstrip modeling equation. However, the numerical integration in Galerkin's procedure for capacitance calculation needs to deal with the critical singularity at $\alpha=0$ since the Green's

function becomes a numerically unstable function when the electric walls located at the top and bottom are removed simultaneously. In order to solve this problem, the Green's function was divided into singular and regular parts, and the spatial Galerkin's procedure was applied to the singular part while the spectral domain Galerkin's procedure was applied to the regular part [11,12].

$$\tilde{G}(\alpha)=\tilde{G}_{\text{Singular}}(\alpha)+\tilde{G}_{\text{Regular}}(\alpha)=\tilde{G}_{\text{Singular}}(\alpha)+\left[\tilde{G}(\alpha)-\tilde{G}_{\text{Singular}}(\alpha)\right] \qquad (5.1)$$

Mathematically, the extracted singular part of the Green's function described above, in general, implies that interconnects are located in a purely homogeneous medium (e.g., free space). Thus, previous works used elliptic integral equations obtained by the conformal mapping technique instead of the spatial Galerkin's method for structures in a homogeneous medium [11,27].

However, these techniques have practical difficulties considering the situations as following situations. First, applying this approach in both spatial and spectral domain, in general, requires a computation time, and, if the conductors are located in a homogeneous single medium, the calculation should be carried out purely in the spatial domain, including the conformal mapping technique. Second, Galerkin's procedure for capacitance becomes even more complicated if the conductor has a finite thickness. Conventionally, the procedure in the spatial domain was necessary since it was the only way to obtain the inductance values even for lossy substrate media. According to the magnetic potential-based quasi-static SDM introduced in the previous chapter, it is clear that the conventional method is not accurate for high substrate conductivities and high frequencies. Thus, doing the entire calculation in the spectral domain is more appropriate in order to take advantage of successful evaluation of the series and shunt components for the lossy substrate effects and conductor thickness. The main approach is done in the following manner.

1. Investigate the behavior of capacitive and inductive Green's function around the specific singular point, $\alpha=0$, in the spectral domain.

2. Reconstruct the equivalent physical structure in the spatial domain for $\alpha=0$ using the information obtained in the first step.
3. Derive the Green's function again for the structure and transform it into the spectral domain.
4. Apply the Galerkin's procedure fully in the spectral domain.

In the first section, a new technical approach to obtain an appropriate Green's function for the specific singular point, $\alpha=0$, is introduced and applied to typical structures. Also, using the proposed method, the calculated results are compared with the previous results to demonstrate the validity of this approach of decreased complexity. That is, the evaluation procedure is done purely in the spectral domain, and the proposed method accurately models the interconnect structures with the metallization thickness. In addition, the equivalent inductance calculation approach is introduced for the same structure in the next section using a similar singular point treatment.

Once the distributed elements are computed, the lumped element matrices for the structures are extracted. That is, if a structure has a total of M lines with N signal lines and $(M-N)$ reference lines, the dimension of the final matrix should be reduced from $M \times M$ to $N \times N$. In contrast to the simplicity of the capacitance matrix reduction, the inductance matrix must be obtained by solving the current relations between the lines.

In the last section, typical structures such as co-planar microstrips and co-planar waveguides are examined to show the validity of the entire approach for the interconnect structures without ground plane.

5.2 Capacitive Coupling in Signal-Ground Paired Interconnects

If the bottom ground plane is completely removed, it is expected that the capacitances between the conductors and ground plane (i.e., self-capacitances) annihilates, and the mutual capacitance between the lines are the only capacitance component. For instance, the changes of self and mutual capacitance as a function of substrate height H_2 for the structure depicted in Figure 5.2 are computed. The two values

converge to a final value drawn as a straight line (*o* marks). However, the capacitance calculated by this quasi-static method blows up when the height increases further due to the singularity in the system equation.

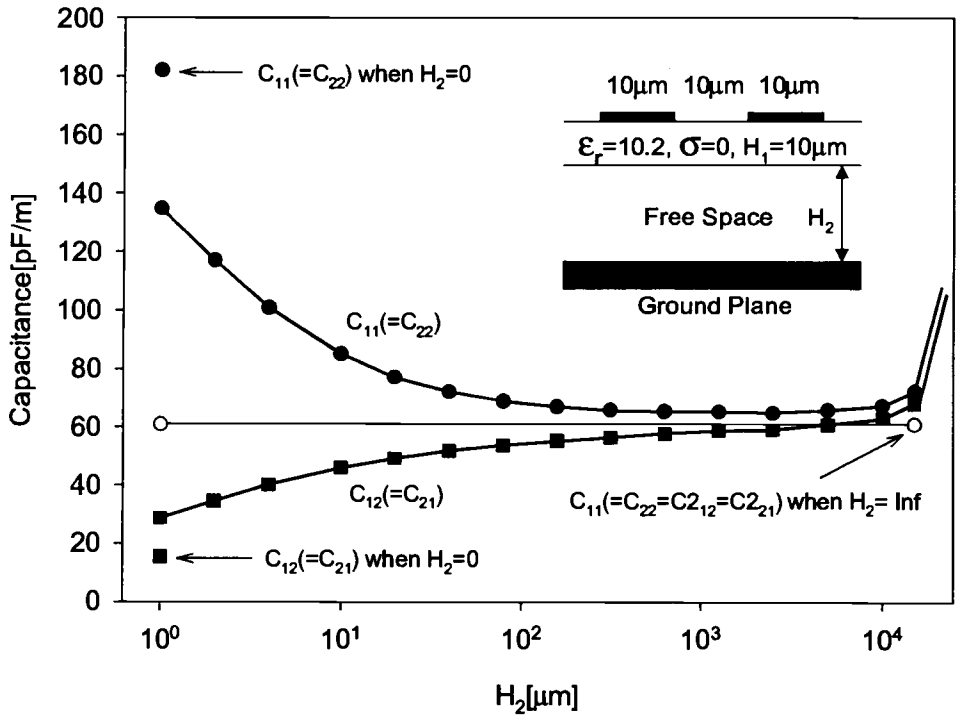

Figure 5.2 Changes of capacitance as a function of ground plane spacing calculated by normal quasi-static SDM and its numerical failure.

Even though the calculated capacitance is approaching closely to the final value in this case, it is not guaranteed to obtain the converged (final) value in many cases, especially for asymmetrically coupled strips and multiple coupled lines. Thus, calculating the capacitance for this configuration is not as simple as the previous approach by setting the height of the medium to infinity. Hence, a modified Green's function needs to be derived.

In order to derive a new Green's function for interconnects without a ground plane, the following three layered general planar transmission line configuration is considered.

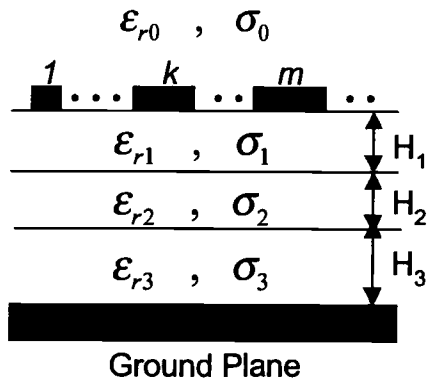

Figure 5.3 General multiconductor structure with ground plane

For a finite height H_3 of bottom layer, the Green's function is given as

$$\tilde{G}_{\phi}(\alpha)=\frac{1}{|\alpha|\left[\varepsilon_{c0}+\varepsilon_{c1}\dfrac{\varepsilon_{c1}+\varepsilon_{c2}\dfrac{\varepsilon_{c2}+\varepsilon_{c3}Coth(|\alpha|H_3)Coth(|\alpha|H_2)}{\varepsilon_{c3}Coth(|\alpha|H_3)+\varepsilon_{c2}Coth(|\alpha|H_2)}Coth(|\alpha|H_1)}{\varepsilon_{c2}\dfrac{\varepsilon_{c2}+\varepsilon_{c3}Coth(|\alpha|H_3)Coth(|\alpha|H_2)}{\varepsilon_{c3}Coth(|\alpha|H_3)+\varepsilon_{c2}Coth(|\alpha|H_2)}+\varepsilon_{c1}Coth(|\alpha|H_1)}\right]} \qquad (5.2)$$

where

$$\varepsilon_{ci}=\varepsilon_{ri}-j\frac{\sigma_i}{\omega\varepsilon_o}.$$

Note that, potentially, the Green's function for an arbitrary structure may have multiple singular points. However, in general, it is very rare to encounter any of these singular points during the integration if the distance between the electric sidewalls is sufficiently long [5]. However, the Green's function for the structure without ground plane includes a very critical singular point at $\alpha=0$ which is a necessary point to be evaluated during the

Gelerkin's procedure. That is, the Green's function obtained by setting $H_3=\infty$, in the equation (5.2) becomes

$$\tilde{G}_{\phi}(\alpha)\Big|_{H_3\to\infty} = \frac{1}{|\alpha|\left[\varepsilon_{c0}+\varepsilon_{c1}\dfrac{\varepsilon_{c1}+\varepsilon_{c2}\dfrac{\varepsilon_{c2}+\varepsilon_{c3}Coth(|\alpha|H_2)}{\varepsilon_{c3}+\varepsilon_{c2}Coth(|\alpha|H_2)}Coth(|\alpha|H_1)}{\varepsilon_{c2}\dfrac{\varepsilon_{c2}+\varepsilon_{c3}Coth(|\alpha|H_2)}{\varepsilon_{c3}+\varepsilon_{c2}Coth(|\alpha|H_2)}+\varepsilon_{c1}Coth(|\alpha|H_1)}\right]}. \qquad (5.3)$$

Thus, the standard Galerkin's procedure cannot be directly carried out without any analytical manipulation of the Green's function at this specific point.

In order to derive the mathematical expression for the specific singular point $\alpha=0$, each element of matrix [F] of the following set of linear equations is considered, that is,

$$\mathbf{Fa} = \mathbf{b}. \qquad (5.4)$$

Here, **a** is the unknown coefficient vector, and **b** is the potential vector as used in the previous chapters. Each element of the matrix [F] is obtained by the following Galerkin's procedure, and is simplified as

$$\tilde{F}^{\phi}(\alpha)_{i,k,n,m} = \int_0^{\infty} J_i\left(\frac{\alpha W_k}{2}\right)\cdot\tilde{G}_{\phi}(\alpha)\cdot J_n\left(\frac{\alpha W_m}{2}\right)\cdot P(\alpha)_{i,k,n,m}\cdot d\alpha \qquad (5.5)$$

The entire integrand can be simplified due to the properties of the Bessel function. That is,

$$J_i(0) = \begin{cases} 0 & if \quad i \neq 0 \\ 1 & if \quad i = 0 \end{cases} \qquad (5.6)$$

As described in (5.6), the first condition of the singularity at $\alpha=0$ is that the orders of each Bessel function in the integrand must be 0 (i.e., $i=n=0$). Otherwise, the integrand

becomes 0 and does not include any singular point. Also, the phase term becomes purely a cosine function and becomes 1 as α approaches 0. Consequently, the entire integrand becomes simply the Green's function, i.e.,

$$\lim_{\substack{H_b\to\infty \\ \alpha\to 0}}\left[J_0\left(\frac{|\alpha|W_k}{2}\right)\cdot\tilde{G}_\phi(\alpha)\cdot J_0\left(\frac{|\alpha|W_m}{2}\right)\cdot\cos\left[|\alpha|(x_k-x_m)\right]\right]=\tilde{G}_\phi(\alpha) \qquad (5.7)$$

where H_b is the height of the bottom layer medium. Effectively, for α=0 the two conductors with finite widths of W_k and W_m can be regarded as one infinitesimally thin conductor regardless of the distance between the lines. An additional simplification of the Green's function can be made by setting $Coth(\alpha H)\approx 1/\alpha H$ if α is very small. Then, for α=0 the Green's function can be written as

$$\tilde{G}_\phi(\alpha)\approx\frac{1}{|\alpha|\left[\varepsilon_{c0}+\varepsilon_{c1}\dfrac{\varepsilon_{c2}+\dfrac{\varepsilon_{c3}}{|\alpha|H_2}}{\varepsilon_{c1}+\varepsilon_{c2}\dfrac{\varepsilon_{c3}+\dfrac{\varepsilon_{c2}}{|\alpha|H_2}}{|\alpha|H_1}}}{\varepsilon_{c2}\dfrac{\varepsilon_{c2}+\dfrac{\varepsilon_{c3}}{|\alpha|H_2}}{\varepsilon_{c3}+\dfrac{\varepsilon_{c2}}{|\alpha|H_2}}+\varepsilon_{c1}\dfrac{1}{|\alpha|H_1}}\right]}. \qquad (5.8)$$

As expected, this function becomes singular as α approaches 0. Analytically, the exact expression including the specific singular point can be obtained by calculating the residue around the singular point at α=0 [50, Appendix 9], and it becomes

$$\tilde{F}_\phi(\alpha)=\tilde{F}_{\phi,Singular}(\alpha)=\frac{1}{|\alpha|\left[\varepsilon_{c0}+\varepsilon_{c3}\right]}. \qquad (5.9)$$

More generally, for a multilayer structure with an arbitrary number of layers, the singular part of $\widetilde{F}_{\phi}(\alpha)$ becomes

$$\widetilde{F}_{\phi}(\alpha)\Big|_{\alpha\to 0} = \widetilde{F}_{\phi,Singular}(\alpha) = \frac{1}{|\alpha|[\varepsilon_{c0}+\varepsilon_{cb}]} \qquad (5.10)$$

where ε_{cb} is the complex permittivity of the bottom layer whose height is ∞. Effectively, it can be re-organized in the original integrand form assuming that α is very close to 0. That is,

$$J_i\left(\frac{\alpha W_k}{2}\right)\cdot\widetilde{G}_{\phi}(\alpha)\cdot J_n\left(\frac{\alpha W_m}{2}\right)\cdot P(\alpha)_{i,k,n,m}\Big|_{\alpha\to 0}$$

$$\approx J_0\left(\frac{\alpha W_m}{2}\right)\cdot\frac{1}{|\alpha|[\varepsilon_{c0}+\varepsilon_{cb}]}\cdot J_0\left(\frac{\alpha W_k}{2}\right). \qquad (5.11)$$

Since equation (5.11) becomes the same as the expression in equation (5.10) assuming all the Bessel function terms as 1.0, the integrand becomes

$$J_0\left(\frac{\alpha W_m}{2}\right)\cdot\frac{1}{|\alpha|[\varepsilon_{c0}+\varepsilon_{cb}]}\cdot J_0\left(\frac{\alpha W_k}{2}\right)\Big|_{\substack{W_m=0\\W_m=0}}$$

$$\approx\frac{1}{|\alpha|[\varepsilon_{c0}+\varepsilon_{cb}]} \qquad (5.12)$$

Note that $\widetilde{F}_{\phi}(\alpha)$ still can not be evaluated at α=0. However, a physical interpretation can be implicitly derived from equation (5.12). First, all the substrates with finite heights located between the top and bottom layers with infinite height can be ignored. Second, the equivalent conductor width is changed into infinitesimally thin line conductor. Third,

spatial distances between the conductor lines are all ignored and regarded as a single line (i.e., $W_m=W_k=0$).

Using the information given above, a new equivalent structure for $\alpha=0$ is constructed as illustrated in Figure 5.4.

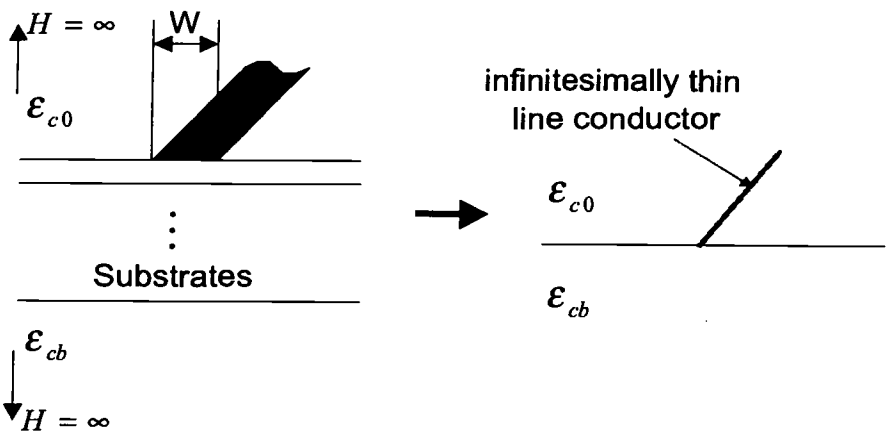

Figure 5.4 Stripline without ground plane and its equivalent configuration for the singular point evaluation at $\alpha=0$ in the spectral domain

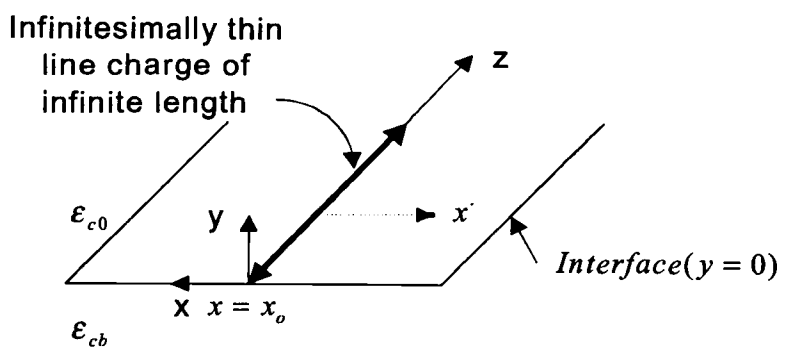

Figure 5.5 Simplified structure for calculating the unknown charge on the conductor located at the interface of two layered media

Since the potential at an arbitrary point on the interface of the two media is of interest, the observation point x' is arbitrarily chosen on the $y=0$ plane as illustrated in Figure 5.5. The electric field intensity due to the infinitely long line charge located at $x=x_o$ can be readily obtained from equation (5.13).

$$\mathbf{E}(x)=\frac{\rho_l\cdot\Pi(x-x_o)}{2\pi\varepsilon_o\left(\frac{\varepsilon_{c0}+\varepsilon_{cb}}{2}\right)\cdot|x-x_o|}\hat{\mathbf{x}} \qquad (5.13)$$

where

$$\Pi(x-x_o)=\begin{cases}1 & if \quad x=x_o\\ 0 & if \quad x\neq x_o\end{cases}.$$

The corresponding potential can be written as

$$V(x')=-\int_{x_{ref}}^{x'}\mathbf{E}(x)\cdot(dx\hat{\mathbf{x}})=\frac{-\rho_l\cdot\Pi(x'-x_o)}{\pi\varepsilon_o(\varepsilon_{c0}+\varepsilon_{cb})}\ln|x'-x_o| \qquad (5.14)$$

By definition, the Green's function at the observation point becomes

$$G_\phi(x')=\frac{-\Pi(x'-x_o)}{\pi\varepsilon_o(\varepsilon_{c0}+\varepsilon_{cb})}\ln|x'-x_o| \qquad (5.15)$$

In order to solve for the charge distribution from equation (5.15), the observation point x' must be moved to x_o where the electric potential is known. Otherwise, this equation cannot be solved since $V(x')$ and ρ_l are both unknown. Thus, the $ln(x)$ term in this equation becomes the Dirac delta function, δ (x), with negative sign.

$$\lim_{x'\to x_o}\left(G_\phi(x')\right)=1[volt]=\lim_{x'\to x_o}\left(\frac{-\Pi(x'-x_o)}{\pi\varepsilon_o(\varepsilon_{c0}+\varepsilon_{cb})}\ln|x'-x_o|\right)$$

$$=\frac{1}{\pi\varepsilon_o(\varepsilon_{c0}+\varepsilon_{cb})}\cdot\delta(0) \qquad (5.16)$$

where

$$\delta(x) = \begin{cases} \infty & if \quad x = 0 \\ 0 & if \quad x \neq 0 \end{cases}.$$

The spectral domain representation of this function can be written as

$$G(x' \rightarrow x_o) = \frac{1}{\pi\varepsilon_o(\varepsilon_{c0} + \varepsilon_{cb})} \cdot \delta(0) \quad \Rightarrow \quad \tilde{G}(\alpha)\Big|_{\alpha=0} = \frac{1}{\pi\varepsilon_o(\varepsilon_{c0} + \varepsilon_{cb})} \tag{5.17}$$

Here, the delta function becomes a constant in the spectral domain, and the magnitude is always *1.0* at the singular point (i.e., for α=0). Hence, the Green's function becomes

$$\therefore \tilde{G}(\alpha) = \frac{1}{\pi(\varepsilon_{c0} + \varepsilon_{cb})} \tag{5.18}$$

where

$$0^- \leq \alpha \leq 0^+.$$

Using this new Green's function, Galerkin's procedure can be carried out entirely in the spectral domain. Each element can be obtained by the following generalized equation. Also, the effects from the substrates with finite thickness are calculated during the normal integration procedure while $\alpha \neq 0$.

$$\tilde{F}^{\phi}(\alpha)_{i,k,n,m} = \int_0^{\infty} J_i\left(\frac{\alpha W_k}{2}\right) \cdot \tilde{G}_{\phi}(\alpha) \cdot J_n\left(\frac{\alpha W_m}{2}\right) \cdot P(\alpha)_{i,k,n,m} \cdot d\alpha$$

$$= \int_0^{\infty} J_i\left(\frac{\alpha W_k}{2}\right) \cdot \left\{ \begin{array}{ll} \dfrac{1}{\pi(\varepsilon_{c0} + \varepsilon_{cb})} & if \quad i = n = \alpha = 0 \\ \tilde{G}_{\phi}(\alpha) & Otherwise \end{array} \right\} \cdot J_n\left(\frac{\alpha W_m}{2}\right) \cdot P(\alpha)_{i,k,n,m} \cdot d\alpha \tag{5.19}$$

Once the capacitance matrix is calculated in this manner, each element does not include the self-capacitance term (i.e., $C_{i0}=0$), but it consist of coupling terms between the lines. For instance, the capacitance matrix written as the form of $\boldsymbol{Q}=\boldsymbol{CV}$ for a general three conductor case is shown in Figure 5.6.

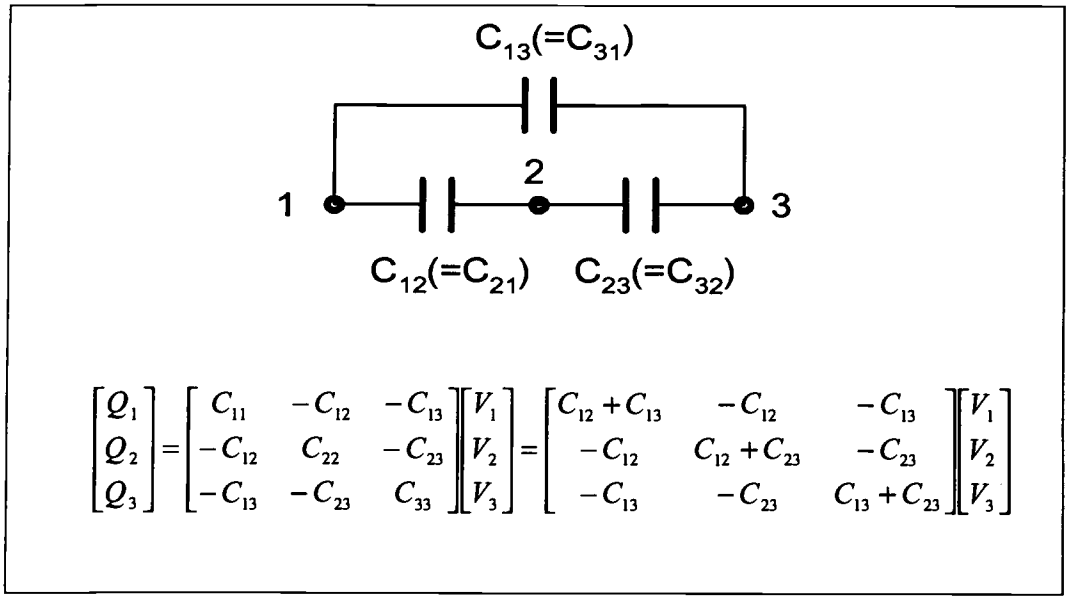

$$\begin{bmatrix} Q_1 \\ Q_2 \\ Q_3 \end{bmatrix} = \begin{bmatrix} C_{11} & -C_{12} & -C_{13} \\ -C_{12} & C_{22} & -C_{23} \\ -C_{13} & -C_{23} & C_{33} \end{bmatrix} \begin{bmatrix} V_1 \\ V_2 \\ V_3 \end{bmatrix} = \begin{bmatrix} C_{12}+C_{13} & -C_{12} & -C_{13} \\ -C_{12} & C_{12}+C_{23} & -C_{23} \\ -C_{13} & -C_{23} & C_{13}+C_{23} \end{bmatrix} \begin{bmatrix} V_1 \\ V_2 \\ V_3 \end{bmatrix}$$

Figure 5.6 Equivalent circuit for a three coupled line structure without ground plane, and its capacitance matrix representation

Also, the summation of each column or, row of capacitance matrix always becomes *0*. Thus, the matrix satisfies the following conditions.

$$\sum_i C_{i,j} = 0 \text{ or } \sum_j C_{i,j} = 0 \qquad (5.20)$$

As previously stated, the dimension of the capacitance matrix needs to be reduced to the size of the signal lines except for the reference conductors. That is, the matrix of $M \times M$ is to be reduced to $N \times N$ size if the structure has N signal conductors by setting the electric voltages of the grounded conductors as $V_0=0$ in the equivalent circuit. The new equivalent self and mutual capacitances referenced to the grounded conductors can be

simply found by eliminating the corresponding rows and columns in the capacitance matrix, as illustrated in Figure 5.7.

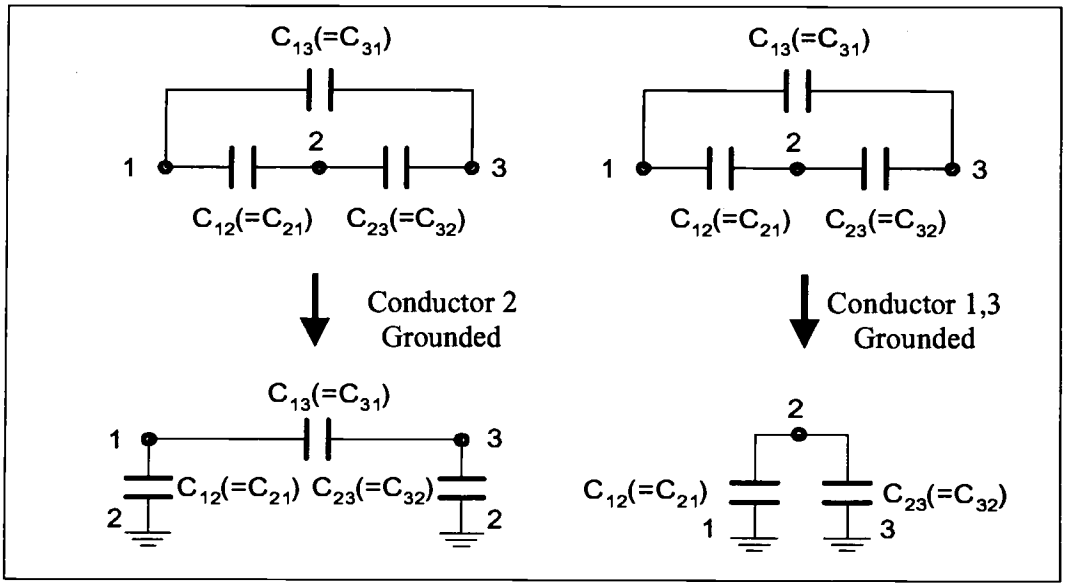

Figure 5.7 Equivalent circuit for a three coupled line structure represented in terms of capacitive coupling considering the referenced conductor

In order to check the validity of this approach, a symmetric coplanar stripline is investigated in terms of final capacitance value, and compared with the method introduced in [11]. Figure 5.7 shows the computed capacitances of a coupled coplanar stripline structure placed in a homogeneous medium (air) and the comparison with the results calculated by the closed form equation for various W/S ratios. Here, the closed form equation for this specific structure is a complete elliptic integral equation determined by conformal mapping [11].

$$C_{air} = \varepsilon_o \frac{K\left(\sqrt{1-\left(\frac{S}{S+2W}\right)^2}\right)}{K\left(\frac{S}{S+2W}\right)} \qquad (5.21)$$

where

$$K(x)=\int_0^{\pi/2}\frac{1}{\sqrt{1-(x\cdot\sin\theta)^2}}d\theta\,.$$

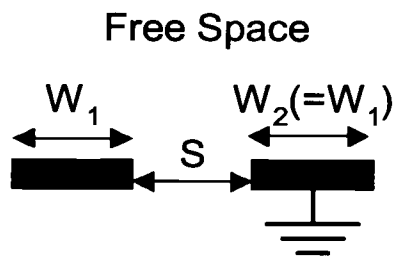

$W_1 : S : W_2$	C_{air}[pF/m] Generated by Elliptic Integral	C_{air}[pF/m] Generated by This Work	Difference
0.1:1:0.1	7.36	7.37	0.14%
0.5:1:0.5	11.32	11.35	0.27%
1:1:1	13.84	13.87	0.22%
2:1:2	16.83	16.86	0.19%
5:1:5	21.32	21.22	0.47%
10:1:10	24.97	25.04	0.28%

Figure 5.8 Comparison of calculated capacitance of coplanar stripline in free space generated by elliptic function and this work

As seen in the result in Figure 5.8, the capacitance values of two infinitesimally thin conducting symmetrically coupled strips are calculated using equation (5.21) and the proposed method. The results are in good agreement with each other for a wide range of W/S ratios. Even though the conformal mapping technique yields accurate results in this case, other approaches must be applied for characterizing coupled lines located in inhomogeneous media.

As a more complicated structure, the capacitive coupling of a symmetric three coplanar stripline structure located in a lossless inhomogeneous medium is calculated

with different conductor widths and separations. The results are shown in Figure 5.9 in terms of ε_{eff} and the characteristic impedance. The modal parameters calculated using the new approach are in good agreement with the previous method in which the spectral domain calculation as well as the additional spatial domain calculation are needed.

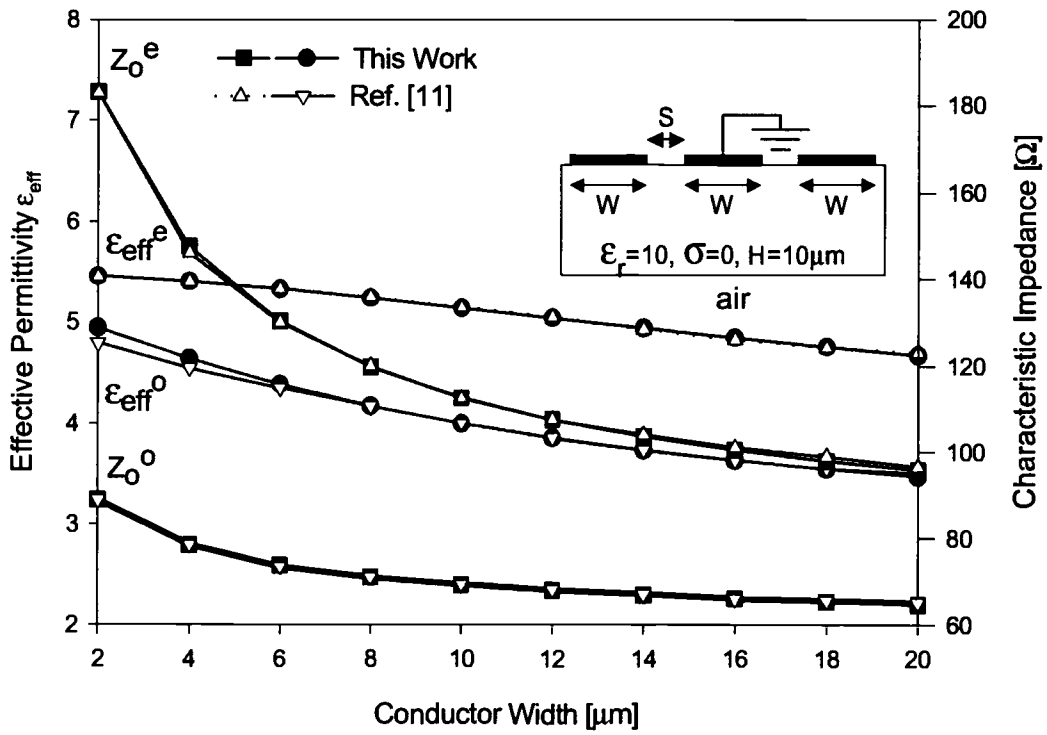

Figure 5.9 Line parameters of coplanar stripline on lossless substrate calculated by this work and compared with reference [11]

Since this work does not include any additional procedure, unlike the conventional approaches, computation speed is significantly improved. The new method proposed here also yields very accurate results and is directly applicable to any arbitrary lossy media. As demonstrated, the proposed method is superior to the elliptical integration method, or any other previous quasi-static approaches in term of modeling of practical structures.

5.3 Inductive Coupling in Signal-Ground Paired Interconnects

The properties of the Green's function for calculating inductance of the structure without ground plane are different from those for the capacitance calculation. Even though there exist some reference conductors among the interconnects, the new quasi-static SDM assumes all of the conductors located between the top and bottom electric walls as active lines. Consequently, the inductance can not be defined since there is no complete current loop in the structure if the substrates are completely lossless, and the ground plane is removed. By setting H_3 to infinity, the magnetic potential based Green's function corresponding to the structure shown in Figure 5.3 can be derived as

$$\tilde{G}_A(\alpha) = \frac{1}{\left[\alpha_0 + \alpha_1 \frac{\left[\alpha_1 + \alpha_2 \frac{(\alpha_2 + \alpha_3 Coth(\alpha_2 H_2))}{(\alpha_3 + \alpha_2 Coth(\alpha_2 H_2))}(Coth(\alpha_1 H_1))\right]}{\left[\alpha_2 \frac{(\alpha_2 + \alpha_3 Coth(\alpha_2 H_2))}{(\alpha_3 + \alpha_2 Coth(\alpha_2 H_2))} + (\alpha_1 Coth(\alpha_1 H_1))\right]}\right]} \qquad (5.22)$$

Since $\alpha_i = \sqrt{\alpha^2 + j\omega\sigma_i}$ in equation (5.22), the critical singularity for the magnetic potential based Green's function occurs when α=0 as well as the conductivities of all the layers are 0. As described in the earlier section, the steps for forming the system equation during the Galerkin's procedure are similar to the case for capacitance, and each element of *[F]* matrix can be obtained by

$$\tilde{F}^A(\alpha)_{i,k,n,m} = \int_0^\infty J_i\left(\frac{\alpha W_k}{2}\right) \cdot \tilde{G}_A(\alpha) \cdot J_n\left(\frac{\alpha W_m}{2}\right) \cdot P(\alpha)_{i,k,n,m} \cdot d\alpha . \qquad (5.23)$$

Applying a similar condition as in the capacitance case,

$$J_0\left(\frac{\alpha W_k}{2}\right) \cdot \tilde{G}_A(\alpha) \cdot J_0\left(\frac{\alpha W_m}{2}\right) \cdot \cos[\alpha(x_k - x_m)]\Big|_{\substack{H_b \to \infty \\ \alpha \to 0}} = \tilde{G}_A(\alpha) \qquad (5.24)$$

The singularity occurs when all the substrates are lossless. In this case, the magnetic-vector-potential-based Green's function becomes

$$\tilde{G}_A(\alpha)\Big|_{\sum_i \sigma_i = 0} = \frac{1}{2\alpha} \qquad (5.25)$$

In this case, deriving the Green's function by setting $\Sigma\sigma_i \neq 0$ is much easier than any other conditions to obtain the stable Green's function. That is, at least one of the substrate layers must have a finite conductivity so that this layer acts as a current returning path to form a complete closed loop. For the semiconductor-based structures, this is a natural choice for not having the singularity problem. However, the value for the lossless substrate should be carefully chosen. In other words, the arbitrarily chosen σ value should be large enough so that the layer acts as a current path, but also low enough that this conductivity does not affect to the accuracy of the entire calculation. Here, for the lossless case one of the layers was set to $\sigma=10^{-3}$ [S/m].

Similar to the capacitance calculation, this approach yields a general $M \times M$ inductance matrix regardless of the number of ground conductors. For instance, the generated inductance matrix for a three-line structure is represented by the inductive coupling components, and shown in Figure 5.10.

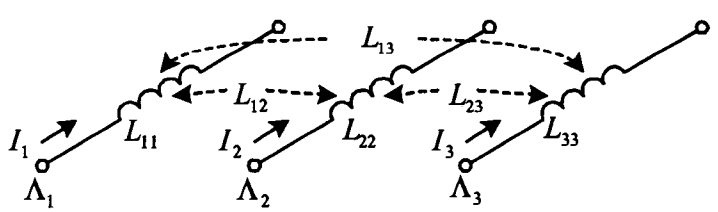

$$\begin{bmatrix} \Lambda_1 \\ \Lambda_2 \\ \Lambda_3 \end{bmatrix} = \begin{bmatrix} L_{11} & L_{12} & L_{13} \\ L_{21} & L_{22} & L_{23} \\ L_{31} & L_{32} & L_{33} \end{bmatrix} \begin{bmatrix} I_1 \\ I_2 \\ I_3 \end{bmatrix}$$

Figure 5.10 Equivalent circuit for a three coupled line structure without ground plane, and its inductance matrix representation

Once the inductance matrix is calculated, it is desirable to reduce the size of the inductance matrix to the actual number of signal conductors. Conventionally, if the structure is completely lossless, the corresponding inductance matrix is obtained from the capacitance matrix using $[\mathbf{L}]=\mu_o\varepsilon_o[\mathbf{C}_o]^{-1}$ after elimination the rows and columns corresponding to the ground conductors.

However, this strategy cannot be directly utilized simply by setting $\Lambda_0=0$ for every ground conductor. Instead, the new inductance matrix is calculated using the current relations since the ground conductor acts as a current returning path. That is, the following condition must be satisfied to derive the final inductance matrix for the configuration shown in Figure 5.11.

$$\sum_i I_i = 0 \tag{5.26}$$

If the 2nd conductor is grounded as shown in the figure, the current relation becomes $I_2=-(I_1+I_3)$ and each magnetic potential referenced by this conductor is $\Lambda_1^{'}=\Lambda_1-\Lambda_2$ and $\Lambda_3^{'}=\Lambda_3-\Lambda_2$, respectively. Using the current relations, the following matrix can be obtained after some simple manipulations.

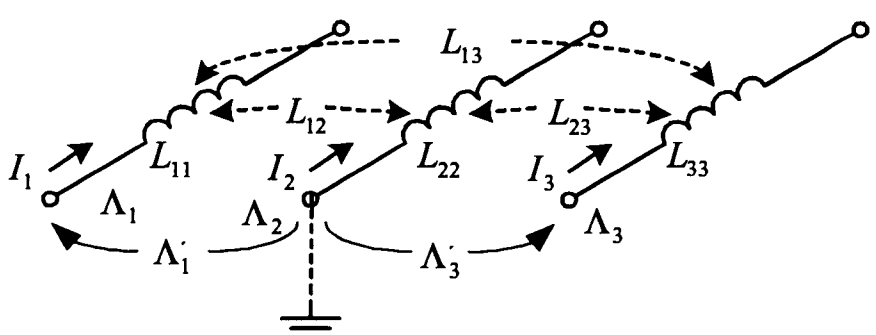

Figure 5.11 The relations between the conducting current at each conductor and magnetic potential corresponding to the grounded center line.

$$\begin{bmatrix}\Lambda_1\\ \Lambda_2\\ \Lambda_3\end{bmatrix}=\begin{bmatrix}L_{11} & L_{12} & L_{13}\\ L_{21} & L_{22} & L_{23}\\ L_{31} & L_{32} & L_{33}\end{bmatrix}\begin{bmatrix}I_1\\ I_2\\ I_3\end{bmatrix}$$

$$\downarrow$$

$$\begin{bmatrix}\Lambda_1'\\ \Lambda_3'\end{bmatrix}=\begin{bmatrix}L_{11}-2L_{21}+L_{22} & L_{13}-L_{23}-L_{12}+L_{22}\\ L_{31}-L_{32}-L_{21}+L_{22} & L_{33}-2L_{32}+L_{22}\end{bmatrix}\begin{bmatrix}I_1\\ I_3\end{bmatrix} \qquad (5.27)$$

For lossless cases, the final inductance matrix should be the same as that of conventional method.

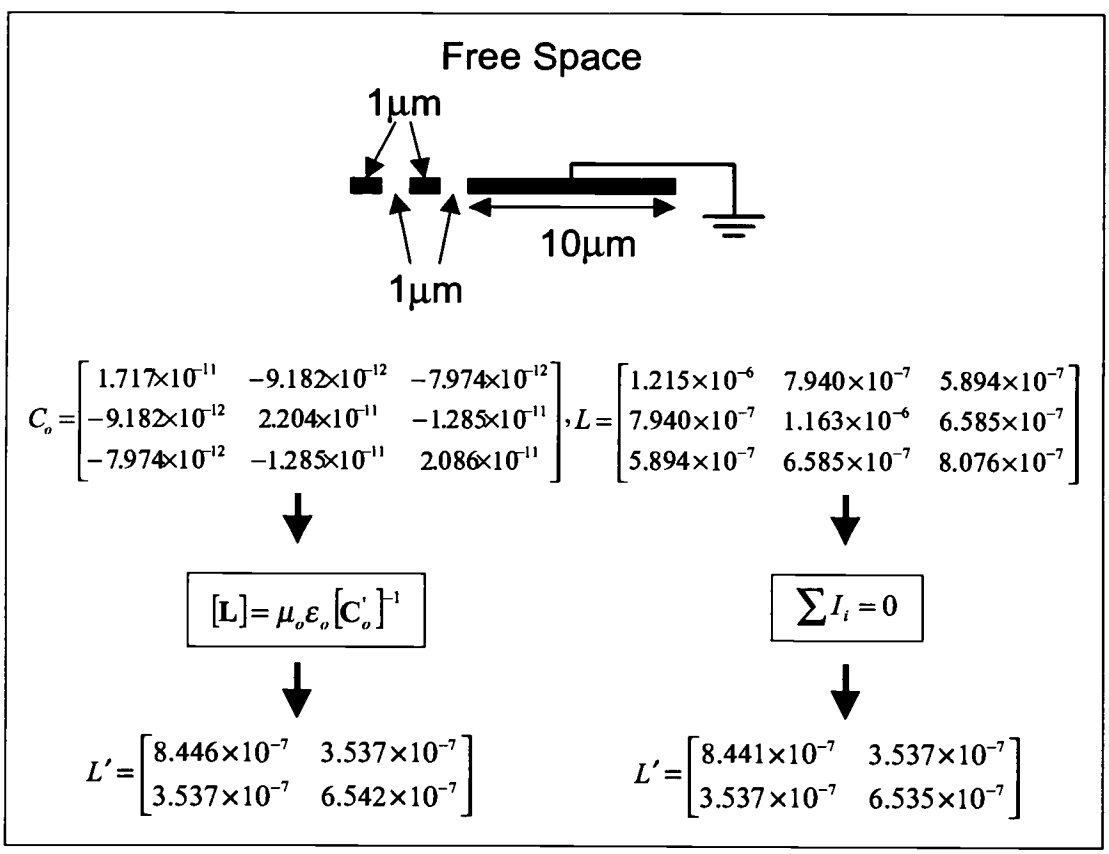

Figure 5.12 Validation of capacitance and inductance matrix reduction technique

As shown in the example depicted in Figure 5.12, the capacitance and inductance matrices for a suspended three-line structure with grounded conductors were generated by this work, and compared with the values generated by the conventional method. As a result, computation of this matrix reduction technique for inductance is very close to the conventional method. Thus, the free space capacitance matrix does not have to be calculated to get the inductance matrix. Moreover, this scheme can be directly applied to any case operating in the skin-effect mode. As commonly used structures, generalized two and three conductors without ground plane are tabulated in Figure 5.13~14 with different ground conductor positions.

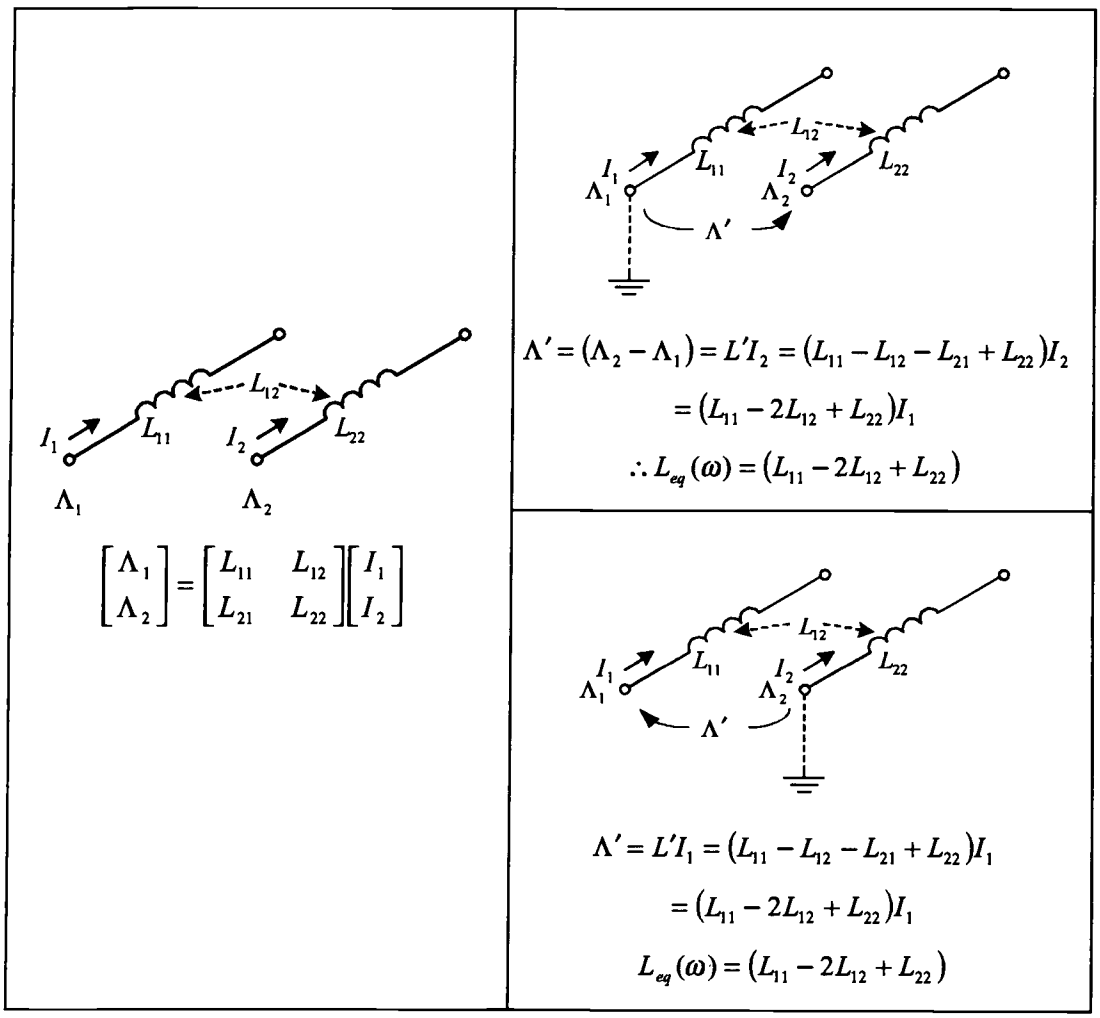

Figure 5.13 Inductance matrix reduction for an arbitrary two line structure

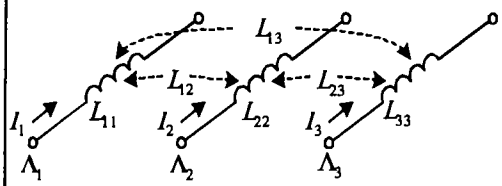

$$\begin{bmatrix}\Lambda_1\\ \Lambda_2\\ \Lambda_3\end{bmatrix}=\begin{bmatrix}L_{11} & L_{12} & L_{13}\\ L_{21} & L_{22} & L_{23}\\ L_{31} & L_{32} & L_{33}\end{bmatrix}\begin{bmatrix}I_1\\ I_2\\ I_3\end{bmatrix}$$

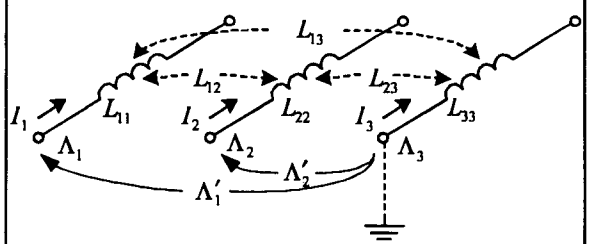

$$\begin{bmatrix}\Lambda_1'\\ \Lambda_2'\end{bmatrix}=\begin{bmatrix}L_{11}-2L_{31}+L_{33} & L_{12}-L_{32}-L_{13}+L_{33}\\ L_{21}-L_{23}-L_{31}+L_{33} & L_{22}-2L_{23}+L_{33}\end{bmatrix}\begin{bmatrix}I_1\\ I_2\end{bmatrix}$$

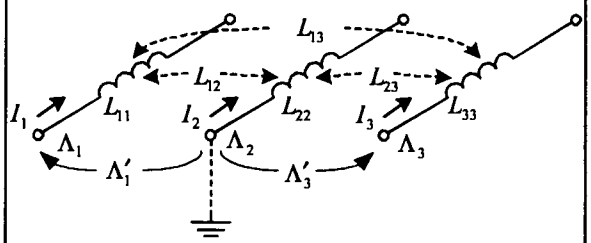

$$\begin{bmatrix}\Lambda_1'\\ \Lambda_3'\end{bmatrix}=\begin{bmatrix}L_{11}-2L_{21}+L_{22} & L_{13}-L_{23}-L_{12}+L_{22}\\ L_{31}-L_{32}-L_{21}+L_{22} & L_{33}-2L_{32}+L_{22}\end{bmatrix}\begin{bmatrix}I_1\\ I_3\end{bmatrix}$$

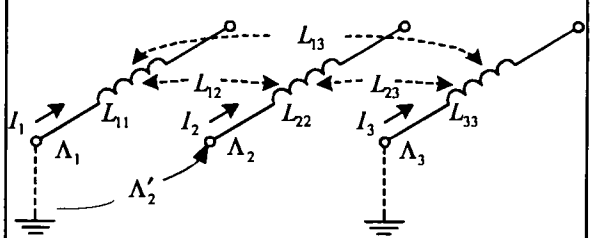

$$\Lambda_2'=\left(\frac{L_{1,1}+L_{3,1}-2L_{2,1}+\Delta(L_{1,3}+L_{3,3}-2L_{2,3})}{2(1+\Delta)}+\frac{(1+\Delta)(2L_{2,2}-L_{1,2}-L_{3,2})}{2(1+\Delta)}\right)I_2$$

where $\Delta=\dfrac{L_{3,1}+L_{1,2}-L_{1,1}-L_{3,2}}{L_{1,3}-L_{3,3}-L_{1,2}+L_{3,2}}$

(See Appendix 10)

Figure 5.14 Inductance matrix reduction for an arbitrary two line structure

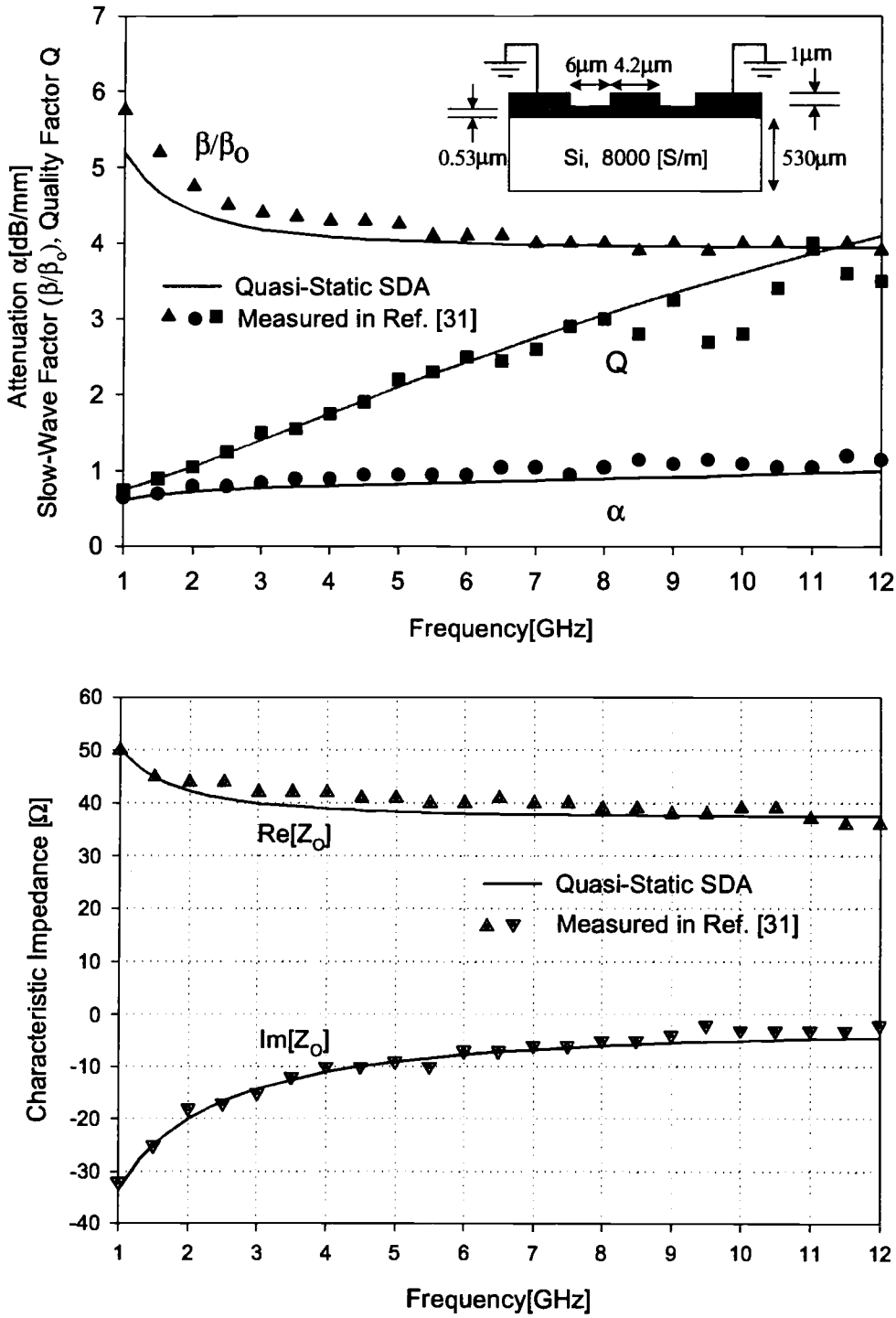

Figure 5.15 Line parameters for a coplanar waveguide structure generated by this work and comparison with measured data in reference [31]

Even if the structures are asymmetric coupled lines with multiple level, the formulated expressions are applicable without any additional procedure. For more complicated structures, similar procedure can be used to derive the reduced matrix expression [Appendix 10]. In addition, the obtained values imply the equivalent resistance and conductance, respectively if inductance and capacitance matrices have imaginary parts.

In Figure 5.15, a typical coplanar waveguide fabricated on silicon substrate is characterized in terms of the characteristic impedance and propagation constant as a function of frequency, and compared with measured data given in [31]. The slow-wave factor calculated by this method is slightly different from the measured data in the lower frequency range. In this case, the operation of the structure is in quasi-TEM mode, and most of the field is concentrated in the oxide layer between the conductors since there is no ground plane at the bottom. In addition, the field intensity becomes even stronger due to the ground conductors at both sides. Hence, dispersion is critical in this region. However, the calculated results are reasonably close to the measured data as frequency increases. Here, the width of each ground conductor of the structure simulated by the quasi-static SDM is set to 50[μm], and the conductor is aluminum with $\sigma_C=3.47\times10^7$[S/m]. The conductor loss is added to the series resistance per unit length of the interconnect which is obtained by the quasi-static SDA. Here, the conductor skin depth at the highest frequency of interest (12 GHz) is approximately 0.8 [μm] which is approximately the same as the conductor thickness of 1 [μm]. In this case, the conductor skin effect is not significant and the DC resistance per unit length is sufficient to represent the conductor loss [32].

5.4 Conclusion

In this chapter, the modeling methodology for interconnects on a lossy substrate with back metallization (ground plane) has been extended to interconnects without ground plane including co-planar strip-lines and co-planar waveguide structures. In the calculation of the distributed self and mutual capacitances of these interconnect structures a new approach has been formulated to efficiently deal with the singularity arising in the

Green's function. The approach used in the inductance calculation first assumes that all conductors are signal lines and then extracts the inductance or inductance matrix once the ground conductor lines have been specified. The results obtained with the new formulation agree well with known solutions for co-planar strip-line and co-planar waveguide structures on lossless substrates. The approach developed in this chapter is general and applies to single as well as multi-level coupled interconnect structures without ground plane [24,26,51,52].

6 TRANSFER MARIX APPROACH FOR GENERAL CASCADED ASYMMETRIC OPTICAL COUPLERS

6.1 Introduction

Optical interconnects have various potential advantages over electrical interconnects including reduced signal attenuation, shorter delay time, larger bandwidth, lower power dissipation and higher integration density [33,34]. Therefore, optical interconnects are increasingly being employed in high-speed electronic circuits and systems to overcome the performance bottleneck caused by electrical interconnects.

Unlike in electronic integrated circuits, optical interconnects are an essential part of opto-electronic and optical integrated circuits (OIC's) used in, for example, optical communications. Here, the optical interconnects function not only as signal transmission guides but are also used to achieve functional components and devices such as power dividers and combiners, optical modulators, switches and filters. The optical directional coupler is a basic building block to many of these functional components and devices.

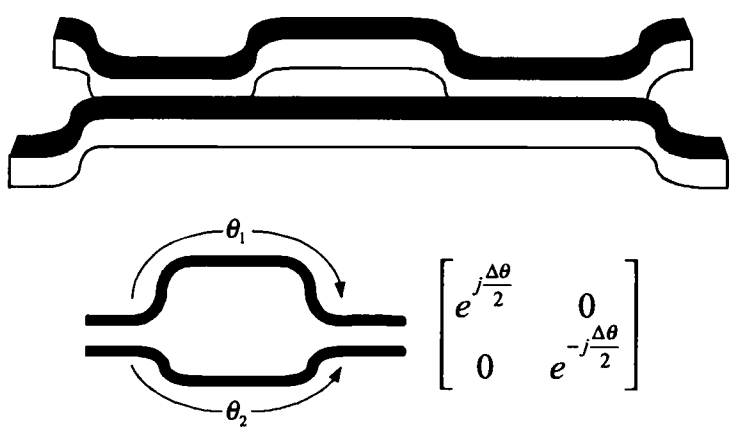

Figure 6.1 Typical example of rib waveguide Mach-Zehnder interferometer yielding phase difference between the propagating lightwaves due to the unequal physical length.

For example, optical directional couplers together with uncoupled waveguide sections of unequal length have been used to realize an integrated Mach-Zehnder interferometer, as illustrated in Figure 6.1. Since one of the lightwave propagating in the waveguide has a relative phase difference compared to the lightwave in the other waveguide due to the unequal lengths, the structure yields wavelength selective characteristics at the output ports. Thus, by cascading several optical interferometer sections, both wavelength and frequency filters have been realized [56,69]. As a disadvantage, however, waveguide bends have to be used to accommodate the uncoupled waveguide sections of unequal lengths. The uncoupled waveguides and bends result in an increase in chip area, and cannot be implemented in planar technology.

In this chapter, a new alternative approach for realizing an optical filter without the use of bends and uncoupled waveguides is described. As an advantage the new structure can be implemented directly in terms of both rectangular (e.g., rib waveguide) and planar waveguide technology. The new filter structure consists of general cascaded asymmetric coupled waveguide sections with various degrees of asymmetry. The approach used here is based on rigorous field theoretic analysis combined with an application of the normal mode theory for coupled transmission lines. Similar to coupled transmission lines, a new transfer matrix description for a general optical directional coupler is derived. Based on this transfer matrix formulation, the wavelength-dependent characteristics of multi-section optical filters consisting of general cascaded asymmetric optical directional coupler sections are investigated.

In the following section, a general symmetric coupled waveguide is characterized, the corresponding transfer matrix is derived, and the basic principle of operation is described. In the remaining sections, the normal mode approach is applied to general asymmetric couplers and the corresponding transfer matrix is derived. Finally, using the transfer matrix approach, the wavelength-dependent characteristics of a basic interferometric structure consisting of cascaded sections of asymmetric waveguide couplers are investigated, and the feasibility of an optical waveguide filter is demonstrated.

6.2 Characterization of a Symmetric Coupled Planar Waveguides

A typical optical coupled planar coupled waveguide structure is composed of multiple layers of thin dielectric slabs with different refractive indices acting as guiding and cladding layers. As a typical example of such structures, an asymmetric coupled waveguide is depicted in Figure 6.2. When the lightwave is launched in medium 1, most of the power propagates in this medium, and part of the power evanesces into the medium 2 (cladding layer), and is coupled into medium 3.

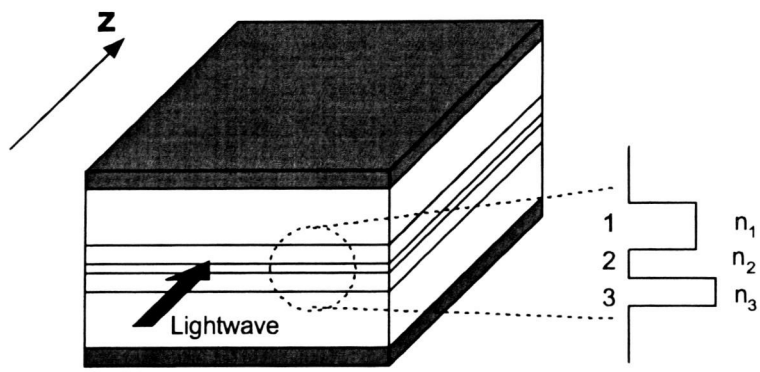

Figure 6.2 Typical geometry of a planar (slab) waveguide coupler

The characteristics of the coupled dielectric media can be modeled in terms of effective refractive indices. Various techniques have been introduced in the past to determine the characteristics of coupled waveguides [35~40]. In general, the modeling procedures can be summarized as solving the wave equation for TE, TM or hybrid modes in terms of the effective indices (or wave numbers) and field distributions. As in full-wave techniques applied to electrical interconnects, Galerkin's method is often used to solve the wave equation for optical waveguides [35]. In order to obtain non-trivial solutions to the system equation formed by basis functions with unknown coefficients, root finding in the form $det(\mathbf{F}(n_{eff}))=0$ is carried out. The corresponding unknown coefficient vector for the basis functions can be found from Galerkin's procedure in the spatial domain based on the calculated effective wave number.

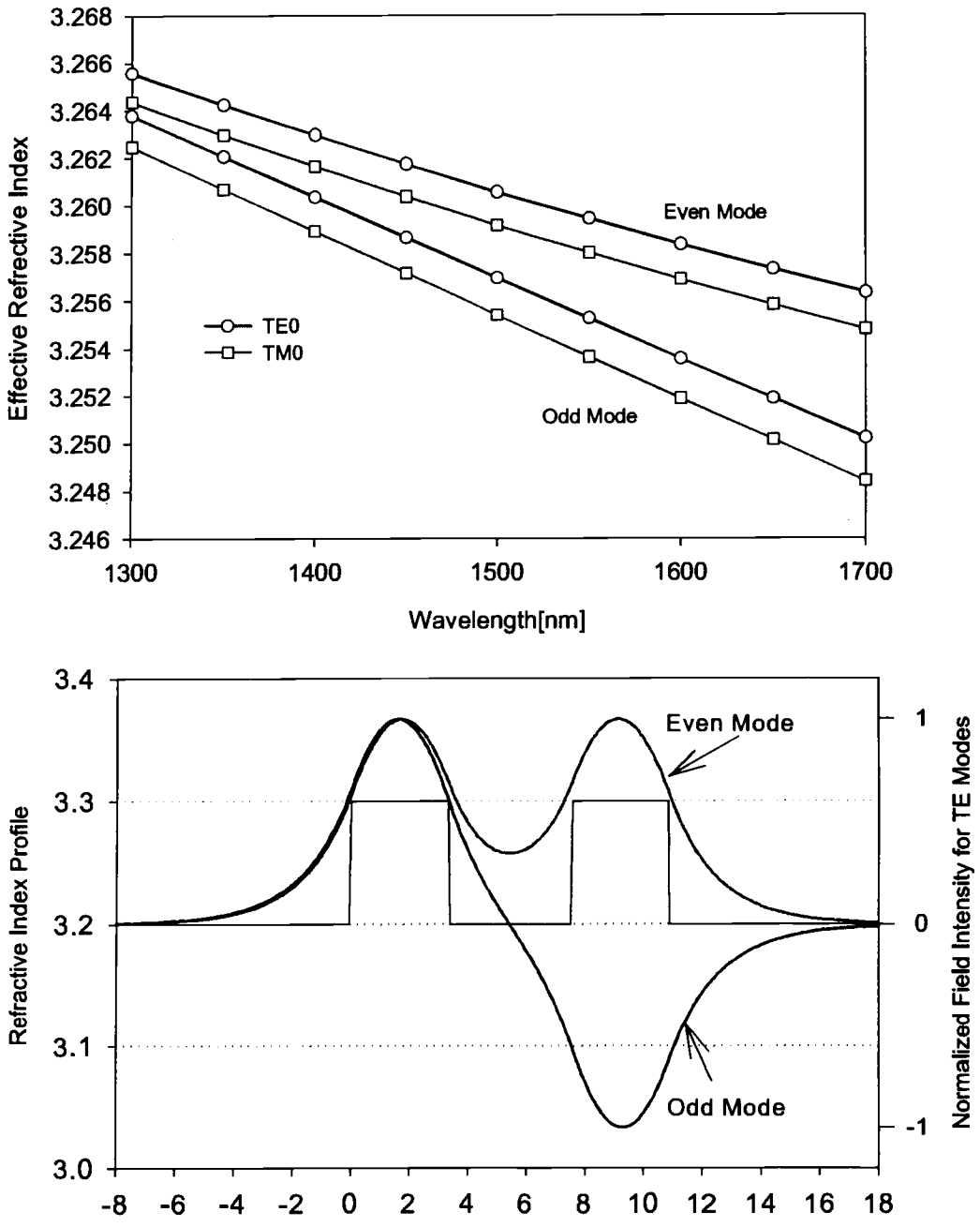

Figure 6.3 Calculated effective refractive indices for even and odd TE modes of an asymmetric coupled planar waveguide ($W_1=W_3=0.8\mu m$, $W_2=1.0\mu m$), and corresponding field distribution at $\lambda=1.5\mu m$

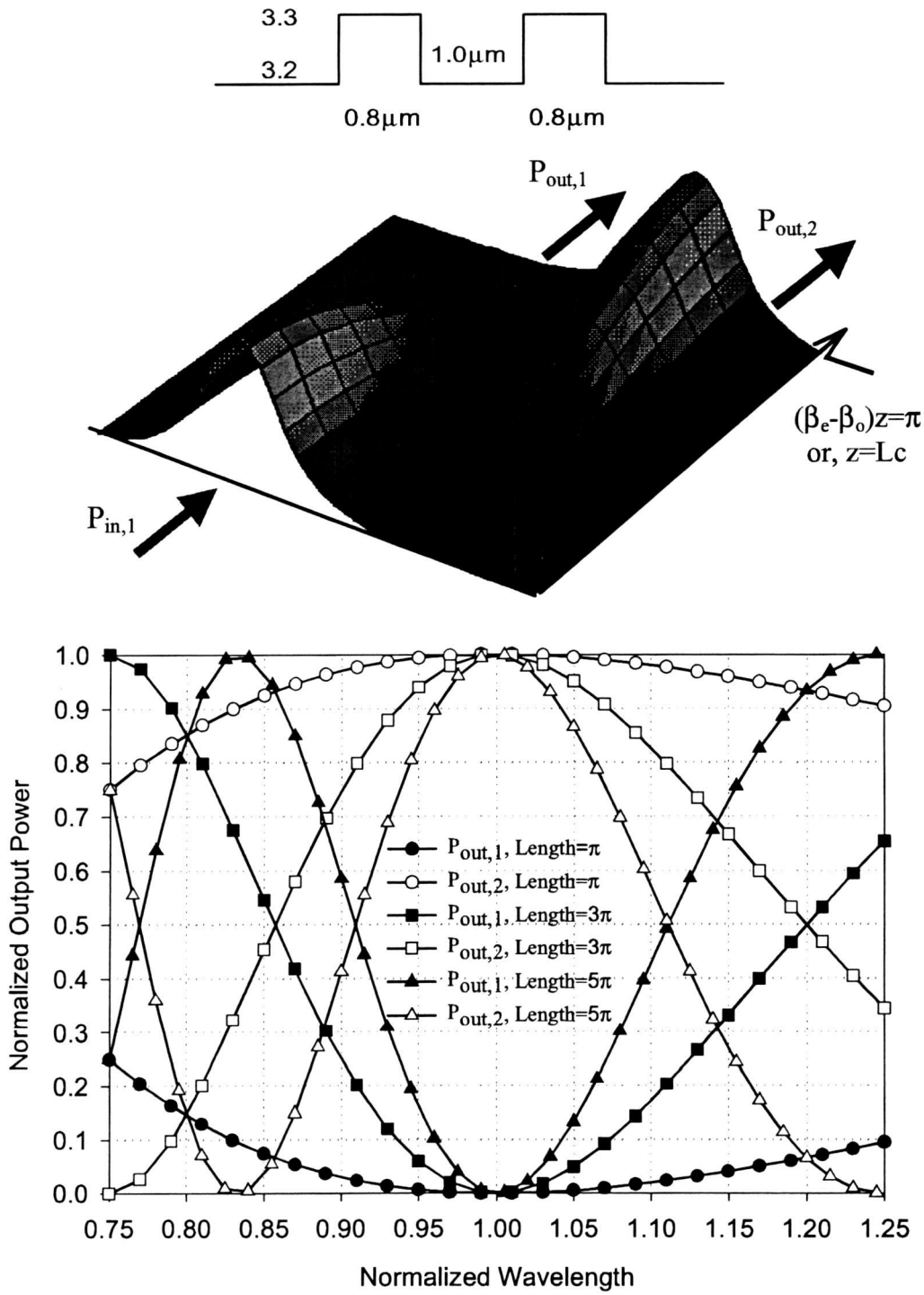

Figure 6.4 Beam propagation in a symmetric coupled waveguide @ λo=1.5μm ($N_{eff,c}$=3.26058, $N_{eff,\pi}$=3.256964, Lc=207.63μm) and normalized output power as a function of normalized wavelength and total electrical length.

Here, the wave propagation characteristics of a general coupled dielectric planar waveguide are calculated using a simple transfer-matrix-based method called Matrix Method [38]. The detailed procedure is described in Appendix 14. As an example, a symmetric coupled dielectric waveguide is characterized in terms of electric field distribution and effective refractive indices, as shown in Figure 6.3.

The symmetric coupler is a very common structure used in OIC's due to the simplicity of design and characterization. Although the detailed fundamental behavior of the symmetric coupler has been reported in [40] as a function of wavelength and electrical length, it is important to briefly review the mechanism of lightwave power exchange between the lines. As an example, the normalized power of a symmetric coupled waveguide along the propagation direction is plotted in Figure 6.4. This figure illustrates that with increasing length the lightwave launched into the first line is transferred to the other line. When the length becomes Lc, called coupling length defined in terms of $(\beta_e-\beta_o)\cdot Lc=\pi$, all the power is transferred to the second waveguide. This power exchange continues as the electrical length increases. The transmitted power at the output ports is dependent on wavelength and physical length of the structure. As shown in Figure 6.4, the coupled power becomes the maximum when the line length is an odd multiple of Lc since the power is totally transferred at these locations.

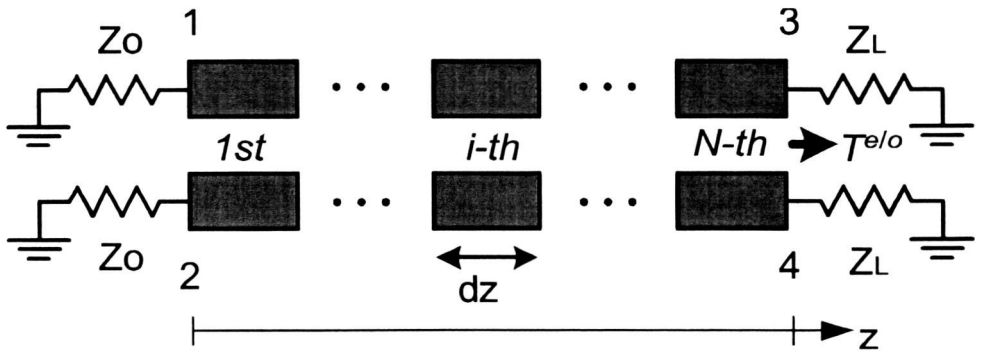

Figure 6.5 Configuration of a multisection symmetric coupler

If the structure is composed of multiple sections of symmetric coupler, the total transmitted power is found from the transfer matrix approach [37,40~42,43]. In this method, the reflected power at the input stage is neglected since the structure is appropriately matched. For an arbitrary *i-th* section as illustrated in Figure 6.5, the normalized transfer matrix is given as [50],

$$\overline{M}_i^{e/o} = \begin{bmatrix} \cos(\beta_i^{e/o} \cdot dz) & -j\dfrac{Z_{o,j}^{e/o}}{Z_o}\sin(\beta_i^{e/o} \cdot dz) \\ -j\dfrac{Z_o}{Z_{o,i}^{e/o}}\sin(\beta_i^{e/o} \cdot dz) & \cos(\beta_i^{e/o} \cdot dz) \end{bmatrix} \tag{6.1}$$

By multiplying each matrix, the total transfer matrix can be represented as the follows.

$$\overline{\mathbf{M}}^{e/o} = \prod_{i=1}^{N} \begin{bmatrix} \cos(\beta_i^{e/o} \cdot dz) & -j\dfrac{Z_{o,m}^{e/o}}{Z_o}\sin(\beta_i^{e/o} \cdot dz) \\ -j\dfrac{Z_o}{Z_{o,m}^{e/o}}\sin(\beta_i^{e/o} \cdot dz) & \cos(\beta_i^{e/o} \cdot dz) \end{bmatrix} = \begin{bmatrix} \overline{M}_{1,1} & \overline{M}_{1,2} \\ \overline{M}_{2,1} & \overline{M}_{2,2} \end{bmatrix}^{e/o} \tag{6.2}$$

where

$$Z_{o,m}^{e/o} = \sqrt{\frac{\mu_o}{\varepsilon_o}} \cdot \frac{1}{n_{eff,m}^{e/o}} \text{ and } \beta_m^{e/o} = \frac{2\pi}{\lambda} \cdot n_{eff,m}^{e/o}.$$

From the final matrix, the even and odd mode wave transmittances are given as [50]:

$$T^{e/o} = \frac{\dfrac{Z_L}{Z_o} + 1}{\dfrac{Z_L}{Z_o}\overline{M}_{1,1}^{e/o} + \overline{M}_{1,2}^{e/o} + \dfrac{Z_L}{Z_o}\overline{M}_{2,1}^{e/o} + \overline{M}_{2,2}^{e/o}} \tag{6.3}$$

Physically, the mode impedances Z_o^e and Z_o^o are very close to each other, especially for optical couplers. Thus, the transfer matrix for an arbitrary section can be simplified as follows

$$\overline{M}_i^{e/o} = \begin{bmatrix} \cos(\beta_i^{e/o} \cdot dz) & -j\sin(\beta_i^{e/o} \cdot dz) \\ -j\sin(\beta_i^{e/o} \cdot dz) & \cos(\beta_i^{e/o} \cdot dz) \end{bmatrix} \tag{6.4}$$

Since we are not interested in the wave delivered to the output ports for each mode, but the relations between the input and output waves for each waveguide (or transmission line), the following matrix form relating normalized input an output field amplitudes is more convenient.

$$\begin{bmatrix} p_{out,1} \\ p_{out,2} \end{bmatrix} = \prod_{i=1}^{N} \left[M_i^{Symm}\right] \begin{bmatrix} p_{in,1} \\ p_{in,2} \end{bmatrix} \tag{6.5}$$

where

$$\left[M_i^{Symm}\right] = \begin{bmatrix} \cos\phi_i & -j\sin\phi_i \\ -j\sin\phi_i & \cos\phi_i \end{bmatrix} \tag{6.6}$$

and

$$\phi_i = \frac{\theta_{e,i} - \theta_{o,i}}{2} = \frac{\beta_i^e dz - \beta_i^o dz}{2}. \tag{6.7}$$

Thus, the total normalized power delivered at the end of the line 1 and line 2 can be found from the following relations:

$$P_{out,1} = \left|p_{out,1}\right|^2 \tag{6.8}$$

and

$$P_{out,2} = \left|p_{out,2}\right|^2 \tag{6.9}$$

For symmetric couplers, the wavelength-dependent response of the output power can be readily expressed in closed form [60,61] as

$$P_{out,2}^{Symm}(\bar{\lambda}) = \begin{cases} \left[\sin\left(\frac{N\pi}{2}\bar{f}\right)\right]^2 & if \quad N = odd \\ 1-\left[\sin\left(\frac{N\pi}{2}\bar{f}\right)\right]^2 & if \quad N = even \end{cases} \qquad (6.10)$$

where $\bar{f}$ is the normalized frequency.

In Figure 6.6, an example structure of a symmetric coupler is considered in terms of power and phase difference of transmitted waves at the output ports.

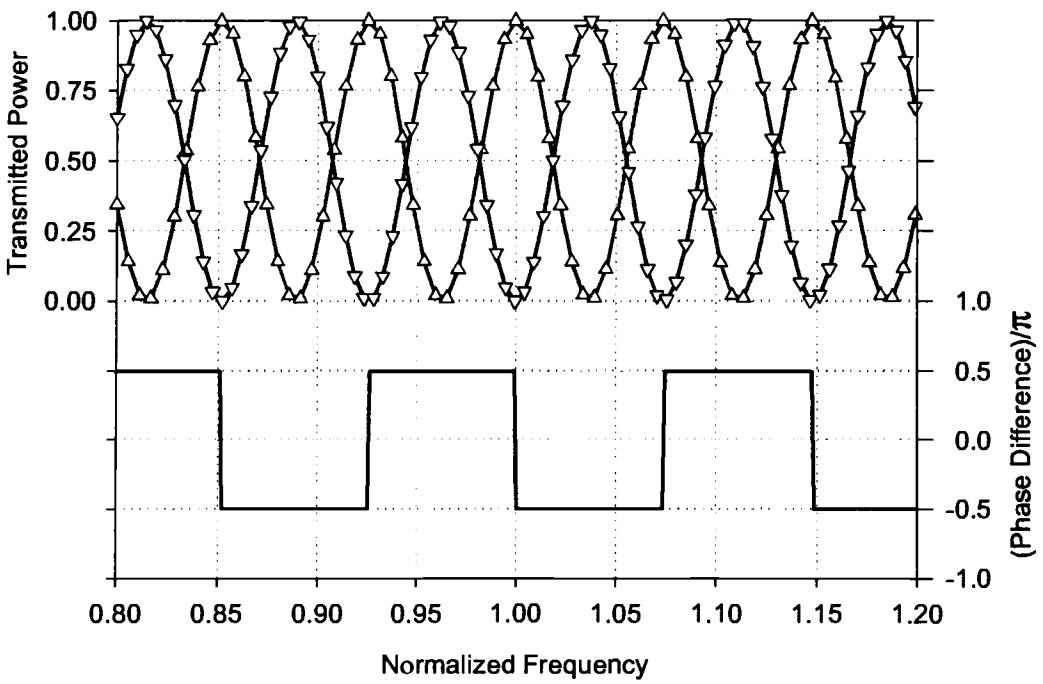

Figure 6.6 Frequency response and phase difference between the lines for 27 cascaded symmetric coupler sections (electrical length of single section = $(\beta_e-\beta_o)\cdot L=\pi$)

6.3 Normal Mode Approach for Asymmetric Couplers

Similar to the even and odd modes of symmetric couplers, asymmetric couplers can be characterized in terms of the c mode and π mode. Again, it is very convenient to represent the optical coupler in terms of a coupled transmission line. The relations between the ports can be accurately analyzed by normal mode theory [18]. In Figure 6.7, two corresponding equivalent circuits for the c and π modes are depicted. R_c and R_π are the ratios of voltages applied to the lines to generate each of the modes.

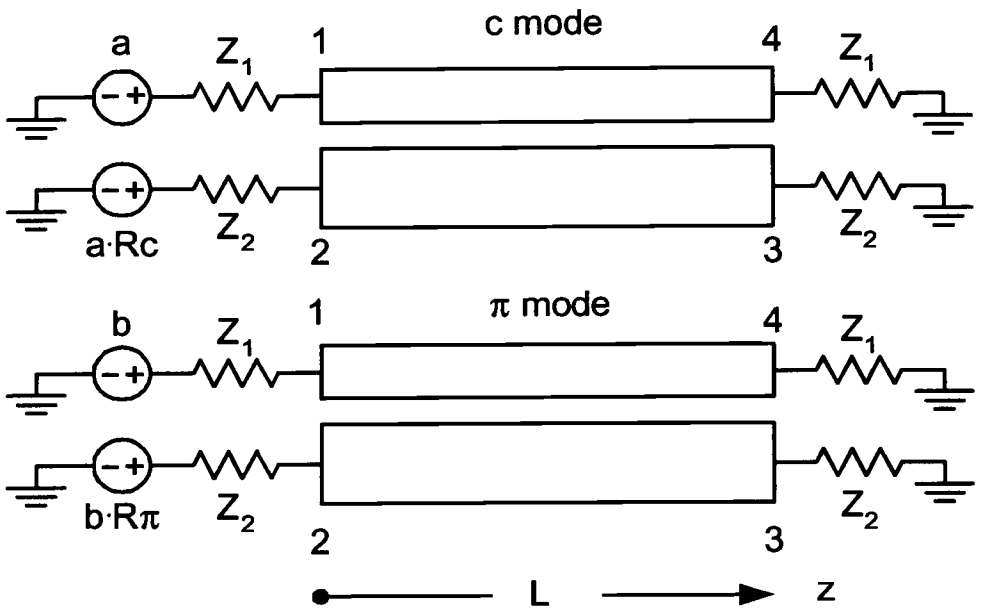

Figure 6.7 Asymmetric coupler and its analytic configuration for each mode

Also, these ratios are physically proportional to the corresponding maximum electric field amplitudes in each guide. Thus, the voltage ratios can be directly calculated from the electric field distributions for the coupled dielectric waveguides, as shown in Figure 6.8.

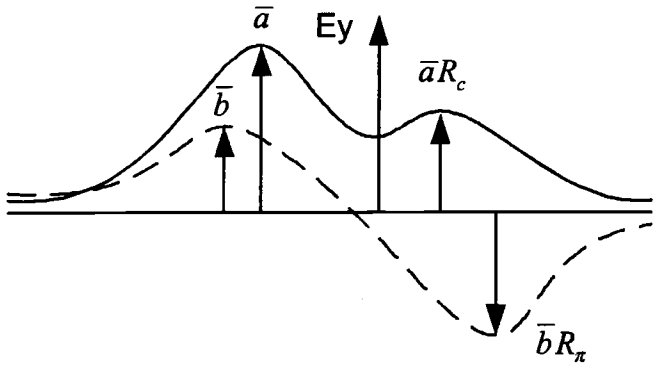

Figure 6.8 Relations between field intensities and voltage ratios for c and π modes

If each termination satisfies Z_2/Z_1=-R_cR_π, called the nonmode converting termination, it enables the excitation of individual normal modes. For TE modes with $Z_2 \approx Z_1$, this condition becomes $R_cR_\pi = -1$. Here, the characteristic line impedances, Z_c and Z_π, can be replaced by wave impedance corresponding to waveguide modes. That is, for TE modes

$$Z_{c,\pi} = \frac{\omega\mu_o}{\beta_{c,\pi}} \qquad (6.11)$$

In order to demonstrate this approach, calculations are carried out only for the TE mode throughout this chapter with the assumption that the load and source impedances are appropriately chosen for the termination conditions.

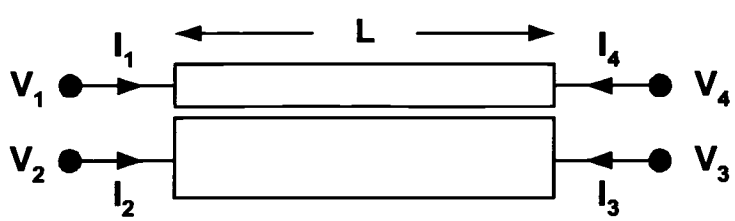

Figure 6.9 A general single section asymmetric coupled transmission line section

The transmission line equations representing the relations between voltage and current at the input and output illustrated in Figure 6.9 can be expressed as follows.

$$-\frac{dV_1}{dz} = z_1 I_1 + z_m I_2 \tag{6.12}$$

$$-\frac{dV_2}{dz} = z_2 I_2 + z_m I_1 \tag{6.13}$$

$$-\frac{dI_1}{dz} = y_1 V_1 + y_m V_2 \tag{6.14}$$

$$-\frac{dI_2}{dz} = y_2 V_2 + y_m V_1 \tag{6.15}$$

The general solutions to the coupled transmission line equations for voltages and currents are given as

$$V_1 = c_1 e^{-\gamma_c z} + c_2 e^{\gamma_c z} + c_3 e^{-\gamma_\pi z} + c_4 e^{\gamma_\pi z} \tag{6.16}$$

$$V_2 = c_1 R_c e^{-\gamma_c z} + c_2 R_c e^{\gamma_c z} + c_3 R_\pi e^{-\gamma_\pi z} + c_4 R_\pi e^{\gamma_\pi z} \tag{6.17}$$

$$I_1 = c_1 Y_{c1} e^{-\gamma_c z} - c_2 Y_{c1} e^{\gamma_c z} + c_3 Y_{\pi 1} e^{-\gamma_\pi z} - c_4 Y_{\pi 1} e^{\gamma_\pi z} \tag{6.18}$$

$$I_2 = c_1 R_c Y_{c1} e^{-\gamma_c z} - c_2 R_c Y_{c1} e^{\gamma_c z} + c_3 R_\pi Y_{\pi 1} e^{-\gamma_\pi z} - c_4 R_\pi Y_{\pi 1} e^{\gamma_\pi z} \tag{6.19}$$

where the *c's* are unknown coefficients.

From the equations above, voltages and current at ports 3 or 4 can be found by setting $z=L$, The corresponding voltage and current expressions in terms of the unknown coefficient vector *[c]* become

$$\begin{bmatrix} V_1 \\ V_2 \\ V_3 \\ V_4 \end{bmatrix} = \begin{bmatrix} 1 & 1 & 1 & 1 \\ R_c & R_c & R_\pi & R_\pi \\ R_c e^{-\gamma_c L} & R_c e^{\gamma_c L} & R_\pi e^{-\gamma_\pi L} & R_\pi e^{\gamma_\pi L} \\ e^{-\gamma_c L} & e^{\gamma_c L} & e^{-\gamma_\pi L} & e^{\gamma_\pi L} \end{bmatrix} \begin{bmatrix} c_1 \\ c_2 \\ c_3 \\ c_4 \end{bmatrix} \tag{6.20}$$

$$\begin{bmatrix} I_1 \\ I_2 \\ -I_3 \\ -I_4 \end{bmatrix} = \begin{bmatrix} Y_{c1} & -Y_{c1} & Y_{\pi 1} & -Y_{\pi 1} \\ R_c Y_{c2} & -R_c Y_{c2} & R_\pi Y_{\pi 2} & -R_\pi Y_{\pi 2} \\ R_c Y_{c2} e^{-\gamma_c L} & -R_c Y_{c2} e^{\gamma_c L} & R_\pi Y_{\pi 2} e^{-\gamma_\pi L} & -R_\pi Y_{\pi 2} e^{\gamma_\pi L} \\ Y_{c1} e^{-\gamma_c L} & -Y_{c1} e^{\gamma_c L} & Y_{\pi 1} e^{-\gamma_\pi L} & -Y_{\pi 1} e^{\gamma_\pi L} \end{bmatrix} \begin{bmatrix} c_1 \\ c_2 \\ c_3 \\ c_4 \end{bmatrix} \quad (6.21)$$

Thus, the relationship between currents and voltages at all 4 ports can be written as

$$\begin{bmatrix} \begin{pmatrix} V_1 \\ V_2 \end{pmatrix} \\ \begin{pmatrix} I_1 \\ I_2 \end{pmatrix} \end{bmatrix} = \begin{bmatrix} [\mathbf{A}] & [\mathbf{B}] \\ [\mathbf{C}] & [\mathbf{D}] \end{bmatrix} \begin{bmatrix} \begin{pmatrix} V_4 \\ V_3 \end{pmatrix} \\ \begin{pmatrix} -I_4 \\ -I_3 \end{pmatrix} \end{bmatrix} \quad (6.22)$$

Also, these relationships can be applied to consecutively cascaded N section structures, and the corresponding matrix can be simplified as

$$\begin{bmatrix} [\mathbf{V_{in}}] \\ [\mathbf{I_{in}}] \end{bmatrix} = \prod_{i=1}^{N} \left(\begin{bmatrix} [\mathbf{A}] & [\mathbf{B}] \\ [\mathbf{C}] & [\mathbf{D}] \end{bmatrix}_i \right) \begin{bmatrix} [\mathbf{V_{out}}] \\ [\mathbf{I_{out}}] \end{bmatrix} \quad (6.23)$$

The transfer matrix can be converted to the corresponding impedance matrix as

$$[Z] = \begin{bmatrix} \mathbf{AC^{-1}} & \mathbf{AC^{-1}D - B} \\ \mathbf{C^{-1}} & \mathbf{C^{-1}D} \end{bmatrix} \quad (6.24)$$

From the impedance matrix, the scattering matrix is determined as

$$[S] = [Z + Z_o \cdot U]^{-1} [Z - Z_o \cdot U] \quad (6.25)$$

where $[Z_o]$ is the reference impedance given by the terminating impedances.

By applying this approach, the transmitted power can be found from the scattering matrix. As an example, an asymmetric coupler is analyzed in the spatial and wavelength domain using the normal mode approach. In this case, the normalized transmitted power in waveguide 2 is not *1.0* although the total electric length (i.e., $\theta_c L - \theta_\pi L$) is 180°.

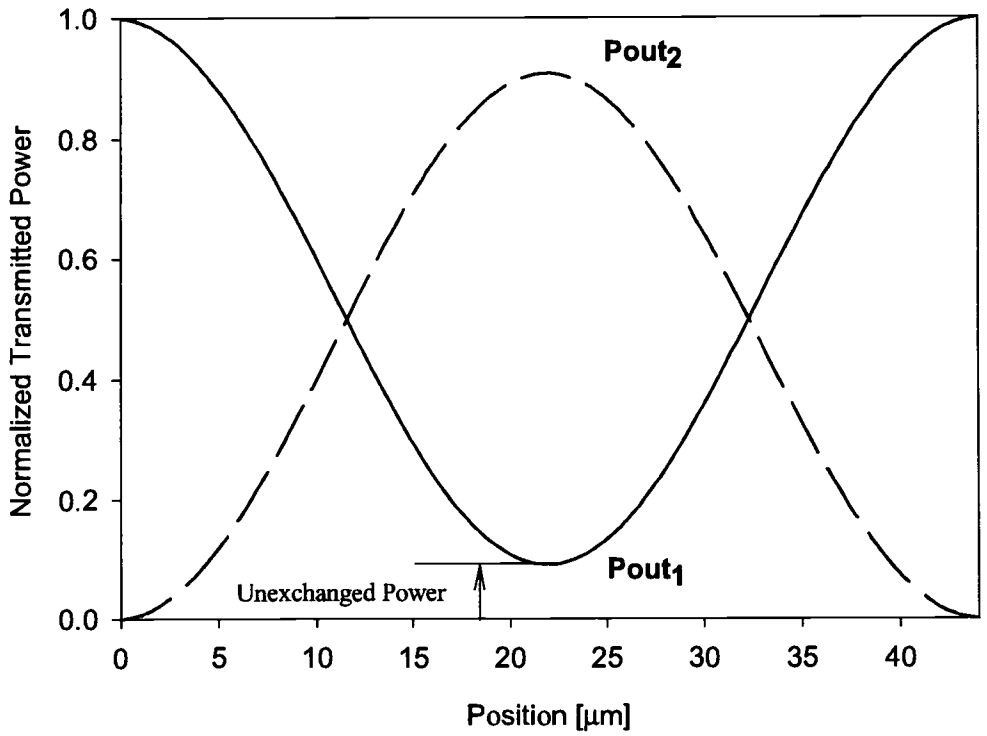

Figure 6.10 Normalized output power of an asymmetric coupler as a function of physical length (λo=*1.5μm, Lc=22.16μm, Rc=0.73,* $R\pi$=*-1.362*).

As seen in Figure 6.10, at the first 180° point (i.e., $z=Lc$), there exists a certain amount of untransferred power in waveguide 1, For 360° (i.e., $z=2Lc$), the total power is again in the initial waveguide, as at the 0° point.

Considering the effects of the coupling length, it is appropriate to set the electric length, $(\theta_c-\theta_\pi)L$, as multiple of 180° since the maximum power at the load sides (i.e., line 1 or 2) can be expected around at the center wavelength. In order to see the significance

of $n\pi$ lengths with odd n, the transmitted power of an asymmetric coupler ($Rc=0.7$) is investigated for different electrical lengths and plotted in Figure 6.11. As expected, significant changes in the wavelength response can be observed due to the unexchanged power as compared with symmetric coupler cases.

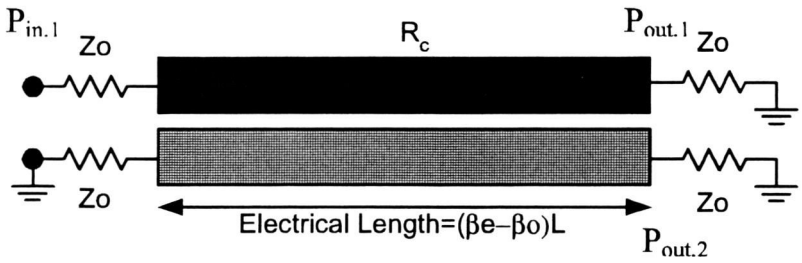

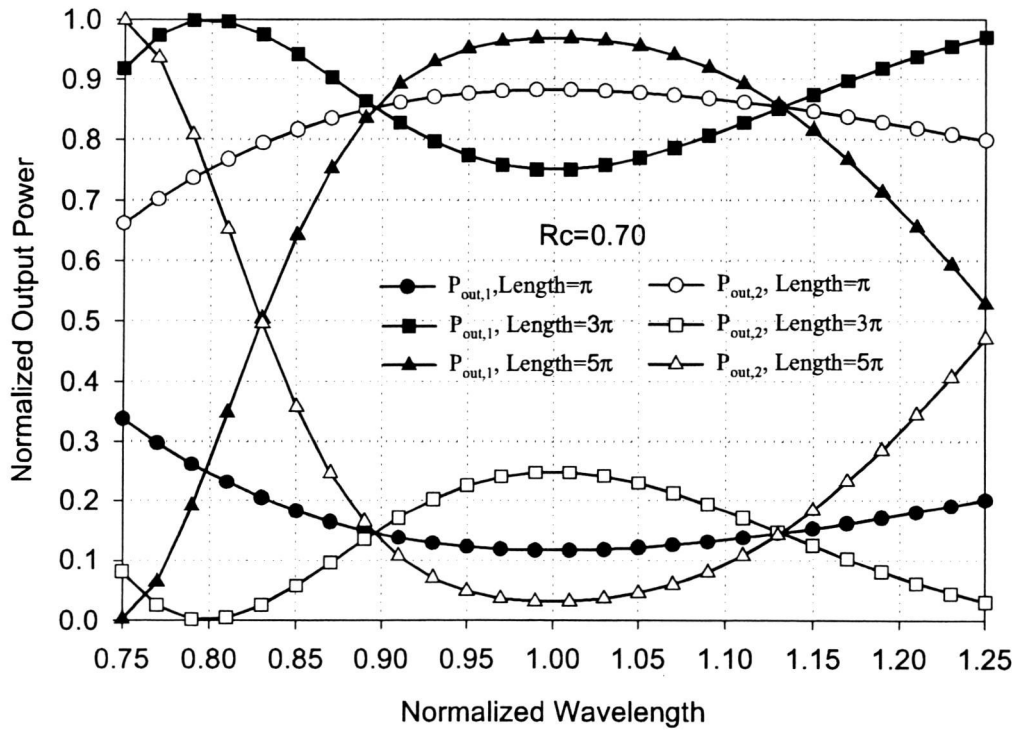

Figure 6.11 Normalized output power of a single section asymmetric coupler (Rc=0.7) as a function of normalized wavelength and total electrical length

6.4 Transfer Matrix Approach for Multisection Asymmetric Couplers

The approach described above can be utilized to characterize cascaded multi-section couplers. The transfer matrix approach is commonly used to characterize symmetric optical couplers due to its simplicity. It is desirable to extend the transfer matrix to arbitrary asymmetric coupled line structures to simplify the analysis of general cascaded asymmetric coupled waveguide structures. In this section, the new transfer matrix for general optical coupler is rigorously derived based on the normal mode approach.

In order to derive the transfer matrix, a single section coupled line is considered first. In [18], the impedance matrix for general coupled transmission lines is given as follows:

$$\begin{bmatrix} V_1 \\ V_2 \\ V_3 \\ V_4 \end{bmatrix} = \begin{bmatrix} Z_{11} & Z_{12} & Z_{13} & Z_{14} \\ Z_{21} & Z_{22} & Z_{23} & Z_{24} \\ Z_{31} & Z_{32} & Z_{33} & Z_{34} \\ Z_{41} & Z_{42} & Z_{43} & Z_{44} \end{bmatrix} \begin{bmatrix} I_1 \\ I_2 \\ I_3 \\ I_4 \end{bmatrix} \tag{6.26}$$

Here, each element is given as

$$Z_{11} = Z_{44} = \frac{Z_c Coth(\gamma_c L)}{1 - R_c/R_\pi} + \frac{Z_\pi Coth(\gamma_\pi L)}{1 - R_\pi/R_c} \tag{6.27}$$

$$Z_{12} = Z_{21} = Z_{34} = Z_{43} = \frac{Z_c R_c Coth(\gamma_c L)}{1 - R_c/R_\pi} + \frac{Z_\pi R_\pi Coth(\gamma_\pi L)}{1 - R_\pi/R_c} \tag{6.28}$$

$$Z_{13} = Z_{31} = Z_{24} = Z_{42} = \frac{Z_c R_c}{(1 - R_c/R_\pi) Sinh(\gamma_c L)} + \frac{Z_\pi R_\pi}{(1 - R_\pi/R_c) Sinh(\gamma_\pi L)} \tag{6.29}$$

$$Z_{14} = Z_{41} = \frac{Z_c}{(1 - R_c/R_\pi) Sinh(\gamma_c L)} + \frac{Z_\pi}{(1 - R_\pi/R_c) Sinh(\gamma_\pi L)} \tag{6.30}$$

$$Z_{22} = Z_{33} = -\frac{Z_c R_c^2 Coth(\gamma_c L)}{1 - R_c/R_\pi} - \frac{Z_\pi R_\pi^2 Coth(\gamma_\pi L)}{1 - R_\pi/R_c} \tag{6.31}$$

$$Z_{23} = Z_{32} = \frac{Z_c R_c^2}{(1 - R_c/R_\pi) Sinh(\gamma_c L)} + \frac{Z_\pi R_\pi^2}{(1 - R_\pi/R_c) Sinh(\gamma_\pi L)} \tag{6.32}$$

with

$$\gamma_c = j\beta_c \text{ and } \gamma_\pi = j\beta_\pi .$$

In order to simplify the approach, it is assumed that each coupled section is terminated with Z_o (i.e., $\sqrt{Z_c Z_\pi} = Z = Z_o$). Thus, there are no reflections at the input. This assumption is directly applied to the multiple section coupler considering that for TE modes in optical waveguides

$$\sqrt{Z_{c,i} Z_{\pi,i}} \approx \sqrt{Z_{c,i+1} Z_{\pi,i+1}} \approx \sqrt{Z_{c,i-1} Z_{\pi,i-1}} \tag{6.33}$$

and

$$Z_{c,i} \approx Z_{\pi,i} \approx Z_i \tag{6.34}$$

Thus, the transfer matrix equations are derived using the following assumptions.

$$Z = \sqrt{Z_c Z_\pi} = Z_o \text{ for a single section coupler} \tag{6.35}$$

$$\sqrt{Z_{c,i} Z_{\pi,i}} = Z_i \approx Z_{i+1} = \sqrt{Z_{c,i+1} Z_{\pi,i+1}} \text{ for a multiple section coupler} \tag{6.36}$$

Using these assumptions, the diagonal elements of the scattering matrix can be readily found as 0.

$$S_{11} = S_{22} = S_{33} = S_{44} = 0 \tag{6.37}$$

Also, S_{12}, S_{21}, S_{34}, S_{43} are all near-end transmission coefficients, and are also 0 since the reflection coefficients of c and π modes are all 0 based on the assumptions described above. That is,

$$\Gamma_m = \frac{j\cdot\left(\frac{Z_m}{Z}-\frac{Z}{Z_m}\right)\cdot\sin(\beta_m L)}{2\cdot\cos(\beta_m L)+j\cdot\left(\frac{Z_m}{Z}+\frac{Z}{Z_m}\right)\cdot\sin(\beta_m L)} \approx 0 \qquad (6.38)$$

where

$$\sqrt{Z_c Z_\pi} = Z \text{ and } m \text{ is } c \text{ or } \pi.$$

In order to verify the results, the set of linear equations is solved in the following manner. Since the diagonal elements are already known to be zero, the linear equations

$$[Z+Z_o\cdot U][S]=[Z-Z_o\cdot U] \qquad (6.39)$$

become

$$\begin{bmatrix} Z_{11}+Z_o & Z_{12} & Z_{13} & Z_{14} \\ Z_{12} & Z_{22}+Z_o & Z_{23} & Z_{13} \\ Z_{13} & Z_{23} & Z_{22}+Z_o & Z_{12} \\ Z_{14} & Z_{13} & Z_{12} & Z_{11}+Z_o \end{bmatrix} \begin{bmatrix} 0 & S_{12} & S_{13} & S_{14} \\ S_{21} & 0 & S_{23} & S_{24} \\ S_{31} & S_{32} & 0 & S_{34} \\ S_{41} & S_{42} & S_{43} & 0 \end{bmatrix}$$

$$= \begin{bmatrix} Z_{11}-Z_o & Z_{12} & Z_{13} & Z_{14} \\ Z_{12} & Z_{22}-Z_o & Z_{23} & Z_{13} \\ Z_{13} & Z_{23} & Z_{22}-Z_o & Z_{12} \\ Z_{14} & Z_{13} & Z_{12} & Z_{11}-Z_o \end{bmatrix}. \qquad (6.40)$$

By manipulating the elements, all unknown parameters can be represented in terms of $(Z-Z_o)^2$.

$$S_{21} = \frac{(Z_{22}+Z_o)Z_{12}Z_{14} + (Z_{11}-Z_o)(Z_{23}Z_{12} - Z_{13}Z_{22} + Z_{13}Z_o) + Z_{13}^3 - Z_{13}Z_{12}^2 - Z_{23}Z_{13}Z_{14}}{(Z_{22}+Z_o)(Z_{14}Z_{22} + Z_{14}Z_o - Z_{13}Z_{12}) + Z_{23}(Z_{12}^2 + Z_{13}^2 - Z_{13}Z_{12} - Z_{23}Z_{14}) - Z_{13}Z_{12}}$$

$$= (Z^2 - Z_o^2)\cdot F_{21}(Z, Z_o, \theta_c, \theta_\pi) \qquad (6.41)$$

$$S_{12} = (Z^2 - Z_o^2)\cdot F_{12}(Z, Z_o, \theta_c, \theta_\pi) \qquad (6.42)$$

$$S_{43} = (Z^2 - Z_o^2)\cdot F_{43}(Z, Z_o, \theta_c, \theta_\pi) \qquad (6.43)$$

$$S_{34} = (Z^2 - Z_o^2)\cdot F_{34}(Z, Z_o, \theta_c, \theta_\pi) \qquad (6.44)$$

Since the terminated impedance Zo is set as the characteristic impedance of the coupler section, $S_{12} = S_{21} = S_{34} = S_{43} = 0$ can be readily obtained from the equations above. Thus, the remaining matrix elements are obtained by solving

$$[Z + Z_o \cdot U][S] = \begin{bmatrix} Z_{11}+Z_o & Z_{12} & Z_{13} & Z_{14} \\ Z_{12} & Z_{22}+Z_o & Z_{23} & Z_{13} \\ Z_{13} & Z_{23} & Z_{22}+Z_o & Z_{12} \\ Z_{14} & Z_{13} & Z_{12} & Z_{11}+Z_o \end{bmatrix} \begin{bmatrix} 0 & 0 & S_{13} & S_{14} \\ 0 & 0 & S_{23} & S_{24} \\ S_{31} & S_{32} & 0 & 0 \\ S_{41} & S_{42} & 0 & 0 \end{bmatrix}$$

$$= \begin{bmatrix} Z_{11}-Z_o & Z_{12} & Z_{13} & Z_{14} \\ Z_{12} & Z_{22}-Z_o & Z_{23} & Z_{13} \\ Z_{13} & Z_{23} & Z_{22}-Z_o & Z_{12} \\ Z_{14} & Z_{13} & Z_{12} & Z_{11}-Z_o \end{bmatrix}. \qquad (6.45)$$

The unknown scattering parameters can be found in terms of electrical line lengths and voltage ratio R_c using the impedance relations obtained from the equation above.

$$S_{31} = \frac{Z_{14}Z_{12} - Z_{13}(Z_{11}-Z_o)}{Z_{14}Z_{23} - Z_{13}^2} = \frac{-R_c}{R_c^2+1}(-\cos\theta_c + \cos\theta_\pi + j(\sin\theta_c - \sin\theta_\pi))$$

$$= -j \cdot \left(\frac{2R_c}{R_c^2 + 1} \right) \cdot \sin\phi \cdot e^{-j\theta} \qquad (6.46)$$

$$S_{13} = \frac{Z_{23}Z_{12} - Z_{13}(Z_{22} - Z_o)}{Z_{14}Z_{23} - Z_{13}^2} = \frac{R_c}{R_c^2 + 1}\left(\cos\theta_c - \cos\theta_\pi + j(-\sin\theta_c + \sin\theta_\pi)\right) = S_{31} \qquad (6.47)$$

$$S_{42} = \frac{Z_{12}Z_{23} - Z_{13}(Z_{22} - Z_o)}{Z_{14}Z_{23} - Z_{13}^2} = \frac{R_c}{R_c^2 + 1}\left(\cos\theta_c - \cos\theta_\pi + j(-\sin\theta_c + \sin\theta_\pi)\right) = S_{31} \qquad (6.48)$$

$$S_{24} = \frac{Z_{12}Z_{14} - Z_{13}(Z_{44} - Z_o)}{Z_{14}Z_{23} - Z_{13}^2} = \frac{R_c}{R_c^2 + 1}\left(\cos\theta_c - \cos\theta_\pi + j(-\sin\theta_c + \sin\theta_\pi)\right) = S_{31} \qquad (6.49)$$

$$S_{41} = \frac{-Z_{12}Z_{13} + Z_{23}(Z_{11} - Z_o)}{Z_{14}Z_{23} - Z_{13}^2} = \frac{-1}{R_c^2 + 1}\left(-\cos\theta_c - R_c^2\cos\theta_\pi + j\left(\sin\theta_c + R_c^2\sin\theta_\pi\right)\right)$$

$$= \left(\cos\phi - j \cdot \left(\frac{R_c^2 - 1}{R_c^2 + 1} \right) \cdot \sin\phi \right) \cdot e^{-j\theta} \qquad (6.50)$$

$$S_{14} = \frac{-Z_{12}Z_{13} + Z_{23}(Z_{44} - Z_o)}{Z_{14}Z_{23} - Z_{13}^2} = \frac{1}{R_c^2 + 1}\left(\cos\theta_c + R_c^2\cos\theta_\pi - j\left(\sin\theta_c + R_c^2\sin\theta_\pi\right)\right) = S_{41}$$

$$(6.51)$$

$$S_{32} = \frac{Z_{12}Z_{13} - Z_{23}(Z_{44} + Z_o)}{-(Z_{44} + Z_o)(Z_{22} + Z_o) + Z_{12}^2} = \frac{-1}{R_c^2 + 1}\left(-R_c^2\cos\theta_c + \cos\theta_\pi + j\left(R_c^2\sin\theta_c + \sin\theta_\pi\right)\right)$$

$$= \left(\cos\phi + j \cdot \left(\frac{R_c^2 - 1}{R_c^2 + 1} \right) \cdot \sin\phi \right) \cdot e^{-j\theta} \qquad (6.52)$$

$$S_{23} = \frac{Z_{13}Z_{12} - Z_{23}(Z_{11} + Z_o)}{-(Z_{11} + Z_o)(Z_{22} + Z_o) + Z_{12}^2} = \frac{-1}{R_c^2 + 1}\left(-R_c^2\cos\theta_c - \cos\theta_\pi + j\left(R_c^2\sin\theta_c + \sin\theta_\pi\right)\right)$$

$$= \left(\cos\phi + j \cdot \left(\frac{R_c^2 - 1}{R_c^2 + 1} \right) \cdot \sin\phi \right) \cdot e^{-j\theta} = S_{32} \qquad (6.53)$$

where

$$\phi = \frac{\theta_c - \theta_\pi}{2},\ \theta = \frac{\theta_c + \theta_\pi}{2} \text{ and } Z_c = Z_\pi = Z_o.$$

Here, the $e^{-j\theta}$ term representing a common phase difference between input and output ports can be omitted. Thus, the scattering matrix can be re-written in the following form.

$$S = \begin{bmatrix} 0 & 0 & S_{13} & S_{14} \\ 0 & 0 & S_{23} & S_{24} \\ S_{31} & S_{32} & 0 & 0 \\ S_{41} & S_{42} & 0 & 0 \end{bmatrix} = \begin{bmatrix} 0 & 0 & S_{31} & S_{41} \\ 0 & 0 & S_{41}^{*} & S_{31} \\ S_{31} & S_{41}^{*} & 0 & 0 \\ S_{41} & S_{31} & 0 & 0 \end{bmatrix} \tag{6.54}$$

Here, (•)* denotes the complex conjugate of (•). From the calculated scattering parameters, the transfer matrix is derived in order to determine the power transfer for the cascaded multisection coupler structure. Considering the relationship between the transmitted and reflected waves of the configuration depicted in Figure 6.12, the corresponding scattering matrix can be written as

$$\begin{bmatrix} b_1 \\ b_2 \\ b_3 \\ b_4 \end{bmatrix} = \begin{bmatrix} 0 & 0 & S_{31} & S_{41} \\ 0 & 0 & S_{41}^{*} & S_{31} \\ S_{31} & S_{41}^{*} & 0 & 0 \\ S_{41} & S_{31} & 0 & 0 \end{bmatrix} \begin{bmatrix} a_1 \\ a_2 \\ a_3 \\ a_4 \end{bmatrix} \tag{6.55}$$

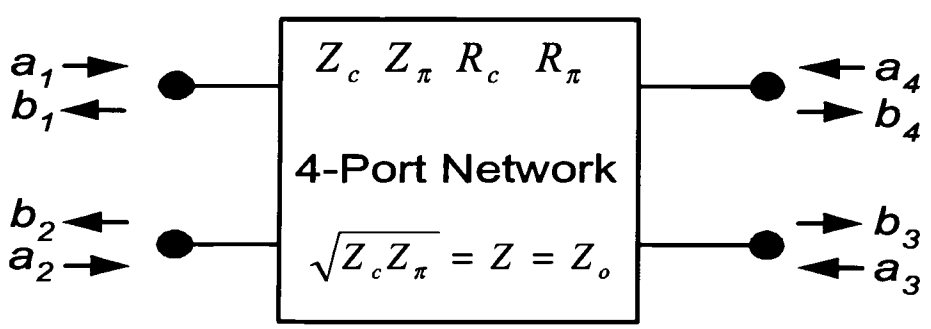

Figure 6.12 The relation between the reflected and transmitted waves at each port

Thus, the reflected and transmitted waves for both directions (i.e., backward and forward directions) can be formulated as follows

$$\begin{bmatrix} b_1 \\ b_2 \end{bmatrix} = \begin{bmatrix} S_{31} & S_{41} \\ S_{41}^* & S_{31} \end{bmatrix} \begin{bmatrix} a_3 \\ a_4 \end{bmatrix} \text{ or } \begin{bmatrix} b_1 \\ b_2 \end{bmatrix} = \begin{bmatrix} S_{41} & S_{31} \\ S_{31} & S_{41}^* \end{bmatrix} \begin{bmatrix} a_4 \\ a_3 \end{bmatrix} \text{ for backward direction} \quad (6.56)$$

$$\begin{bmatrix} b_3 \\ b_4 \end{bmatrix} = \begin{bmatrix} S_{31} & S_{41}^* \\ S_{41} & S_{31} \end{bmatrix} \begin{bmatrix} a_1 \\ a_2 \end{bmatrix} \text{ or } \begin{bmatrix} b_4 \\ b_3 \end{bmatrix} = \begin{bmatrix} S_{41} & S_{31} \\ S_{31} & S_{41}^* \end{bmatrix} \begin{bmatrix} a_1 \\ a_2 \end{bmatrix} \text{ for forward direction} \quad (6.57)$$

The transfer matrices for forward and backward direction become the same. Thus, the transfer matrix for asymmetric coupled structure shown in Figure 6.13 can be represented by a 2x2 matrix for the complex amplitudes of launched and transmitted lightwaves.

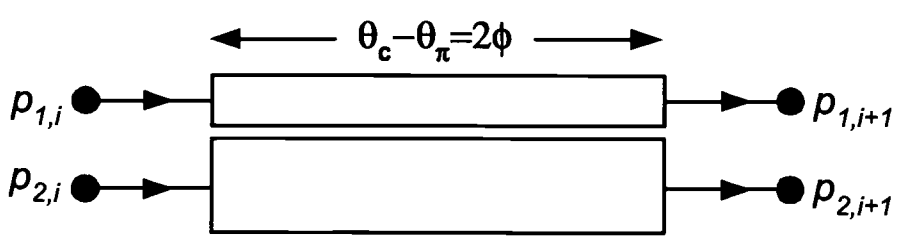

$$\begin{bmatrix} p_{1,i+1} \\ p_{2,i+1} \end{bmatrix} = \left[M_i^{Asym}\right] \begin{bmatrix} p_{1,i} \\ p_{2,i} \end{bmatrix}$$

$$\text{where } \left[M_i^{Asym}\right] = \begin{bmatrix} \cos\phi - j\cdot\left(\frac{R_c^2-1}{R_c^2+1}\right)\cdot\sin\phi & \frac{-2R_c}{R_c^2+1}\cdot j\sin\phi \\ \frac{-2R_c}{R_c^2+1}\cdot j\sin\phi & \cos\phi + j\cdot\left(\frac{R_c^2-1}{R_c^2+1}\right)\cdot\sin\phi \end{bmatrix} \quad (6.58)$$

Figure 6.13 General single section asymmetric coupled transmission line section represented by electrical length, and launched and received wave terms

The equations obtained here satisfy the power transmittance relations. That is,

$$|S_{31}|^2+|S_{41}|^2=\left|\frac{-2R_c}{R_c^2+1}\cdot j\sin\phi\right|^2+\left|\cos\phi-j\cdot\left(\frac{R_c^2-1}{R_c^2+1}\right)\cdot\sin\phi\right|^2=1 \qquad (6.59)$$

$$|S_{31}|^2+|S_{41}^*|^2=\left|\frac{-2R_c}{R_c^2+1}\cdot j\sin\phi\right|^2+\left|\cos\phi+j\cdot\left(\frac{R_c^2-1}{R_c^2+1}\right)\cdot\sin\phi\right|^2=1. \qquad (6.60)$$

Since the waveguide system is lossless, the transfer matrix form satisfies the $M^T M^* = U$ condition. The matrix changes into exactly the same form as in the symmetric case by setting *Rc=1.0*.

$$M^{Asym}\Big|_{R_c=1.0}=M^{Symm}=\begin{bmatrix}\cos\phi & -j\sin\phi\\ -j\sin\phi & \cos\phi\end{bmatrix} \qquad (6.61)$$

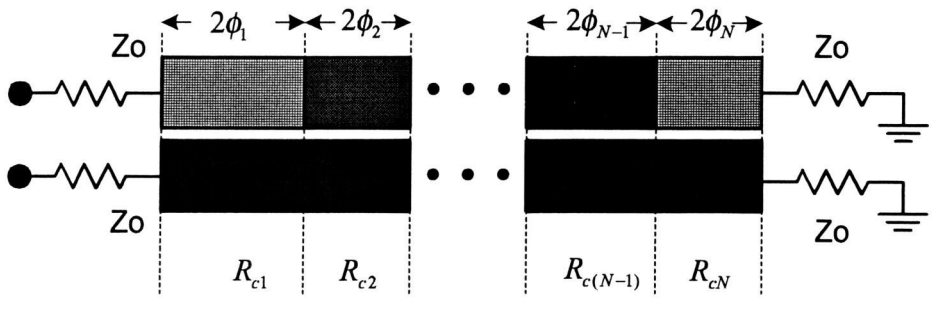

$$\overline{\mathbf{M}}^{Asym}=\prod_{i=1}^{N}\begin{bmatrix}\cos\phi_i-j\cdot k_{1,i}\cdot\sin\phi_i & -j\cdot k_{2,i}\cdot\sin\phi_i\\ -j\cdot k_{2,i}\cdot\sin\phi_i & \cos\phi_i+j\cdot k_{1,i}\cdot\sin\phi_i\end{bmatrix} \qquad (6.62)$$

where $k_{1,i}=\left(\frac{R_{c,i}^2-1}{R_{c,i}^2+1}\right)$, $k_{2,i}=\left(\frac{2R_{c,i}}{R_{c,i}^2+1}\right)$ and $\phi_i=\frac{\theta_{c,i}-\theta_{\pi,i}}{2}$

Figure 6.14 General multisection asymmetric directional coupler characterized by electrical lengths and the asymmetry factors, R_c's

The newly derived transfer matrix can be directly utilized to analyze cascaded asymmetric coupler sections using the same approach for symmetric structures. It can be seen from (6.58) that the asymmetry factor Rc not only affects the magnitude of the lightwave amplitude but also the phase. Thus, Rc can be used as a design parameter to alter the wavelength-dependence of cascaded optical waveguide couplers.

6.5 Basic Optical Interferometric Structure

A coupled waveguide filter can be achieved by the alternately cascading coupled and uncoupled waveguide sections. That is, the uncoupled sections acting as optical interferometer structures establish the phase differences between the propagating lightwaves in each waveguide path, while the coupled sections enable the interference of the different lightwaves. In the configuration shown in Figure 6.1, uncoupled sections with different electrical lengths are used to generate the lightwaves having a desired relative phase difference. As stated in the previous section, this configuration requires waveguide bends.

Based on the transfer matrix form for an asymmetric coupled waveguide structure, an interferometric structure can be developed yielding similar characteristics since the asymmetric section inherently produces different phase differences depending on parameter Rc. As represented in equation (6.62), it is anticipated that the asymmetry factor, Rc, not just determines the phase difference in each section, but also determines the degree of the coupling. In addition, the entire structure is continuously coupled from input to output ports. Hence, as the first step, it is desirable to consider the effect of the asymmetry factor Rc to accomplish the desired interferometric structure. In this section, the relationships between the launched and transmitted lightwave powers for the cascaded structures are investigated in terms of Rc.

An interferometer can be implemented using the basic concept of the asymmetric multisection coupler. Considering the basic properties of the optical coupler, the structure should meet the following criteria. First, each asymmetric coupler should have 180° of length to achieve the maximum power output at the center wavelength as stated in early

section. Second, the total length also should be a multiple of 180° even though the structure is composed of an arbitrary combination of symmetric and asymmetric coupler sections. In Figure 6.15, an appropriate structure satisfying these conditions in order for the structure to work as an interferometer is illustrated.

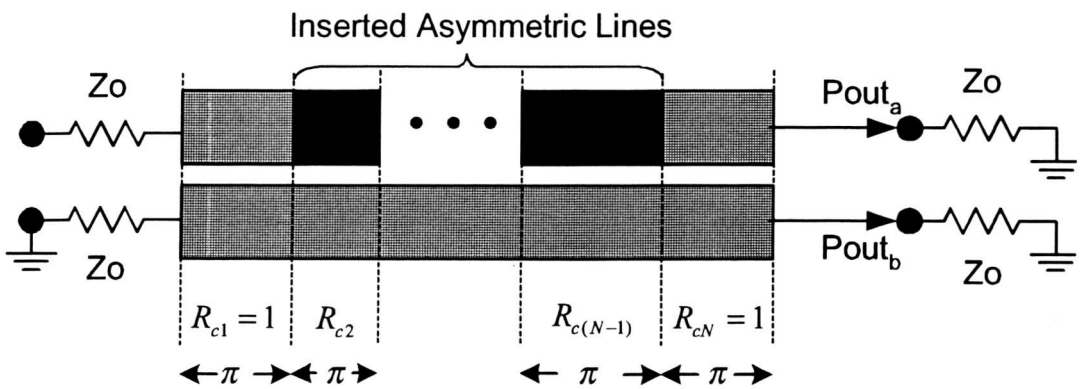

Figure 6.15 Multisection asymmetric optical coupler as an interferometer

Although the structure looks similar to a Mach-Zehnder Interferometer, the power transmitting mechanism is totally different since no uncoupled sections are involved. On the contrary, similar phase changes can be expected due to the interference at the asymmetric sections. As predicted in the previous section, the amount of interference at the asymmetric sections can be readily controlled by changing the R_c values. Changing R_c can be achieved by changes in the asymmetric medium configuration.

In order to investigate the effects of *Rc* in the frequency domain, a seven-section coupler with inserted three identical asymmetric couplers is considered as a function of R_c and normalized frequency, as shown in Figure 6`.16. In this structure, the four symmetric coupler sections are used for narrowing the bandwidth since they do not affect the phase difference. As R_c decreases, the power output of line *a* increases and it becomes the active line when Rc=0.6. Meanwhile, line *b* loses all the power.

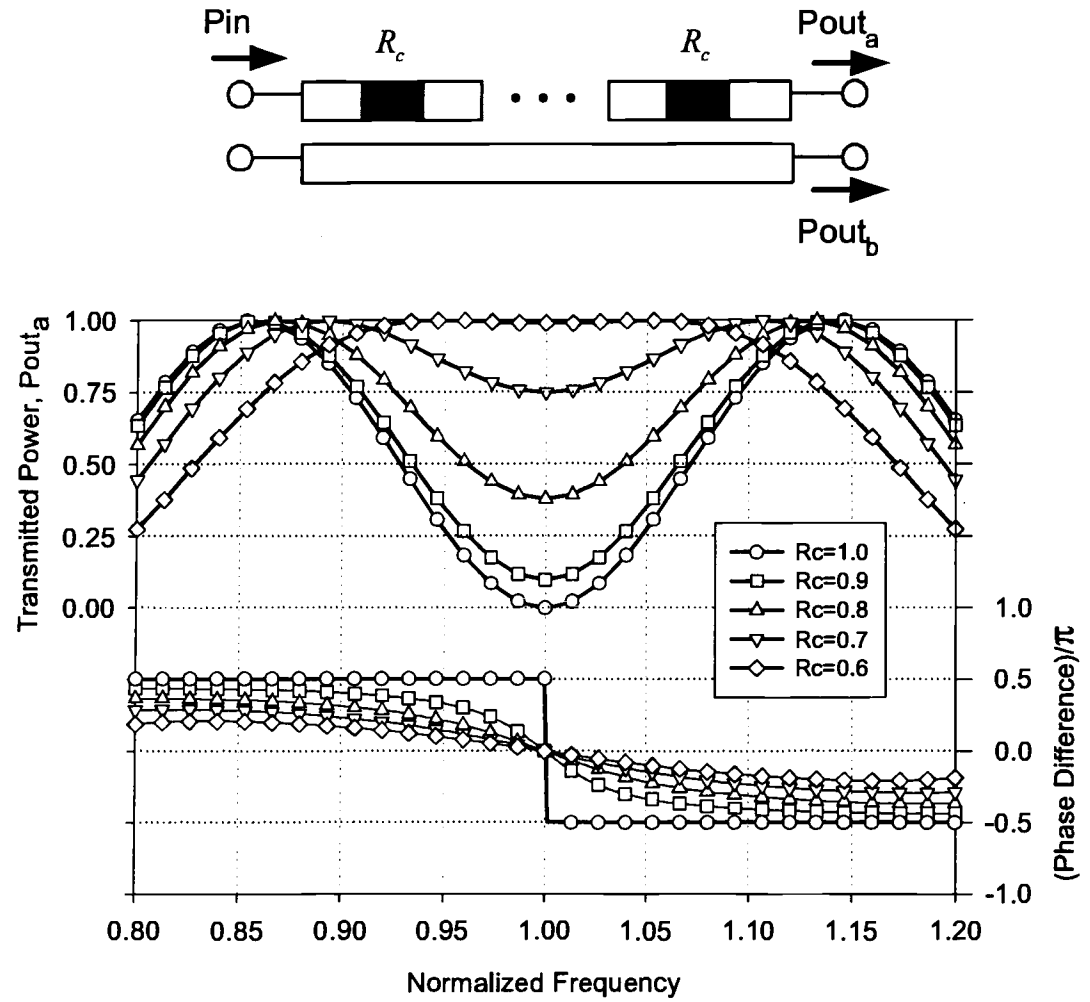

Figure 6.16 Normalized power $P_{out,a}$ and phase difference ($\angle p_{out,a}$-$\angle p_{out,b}$) of cascaded 7 asymmetric coupler sections (length of each section = $(\beta_e-\beta_o)\cdot L=(\beta_c-\beta_\pi)\cdot L=\pi$, $R_{c,2,4,6}=Rc$, $R_{c,1,3,5,7}=1.0$)

It should be noted that the same amount of phase appears as leading and lagging terms compared to the symmetric case since the two diagonal terms in the transfer matrix are complex conjugate. Also, this results in changes of bandwidth and ripples around the center frequency. This phase change ($\angle p_{out,a}$-$\angle p_{out,b}$) can be clearly observed when the structure in Figure 6.17 is considered.

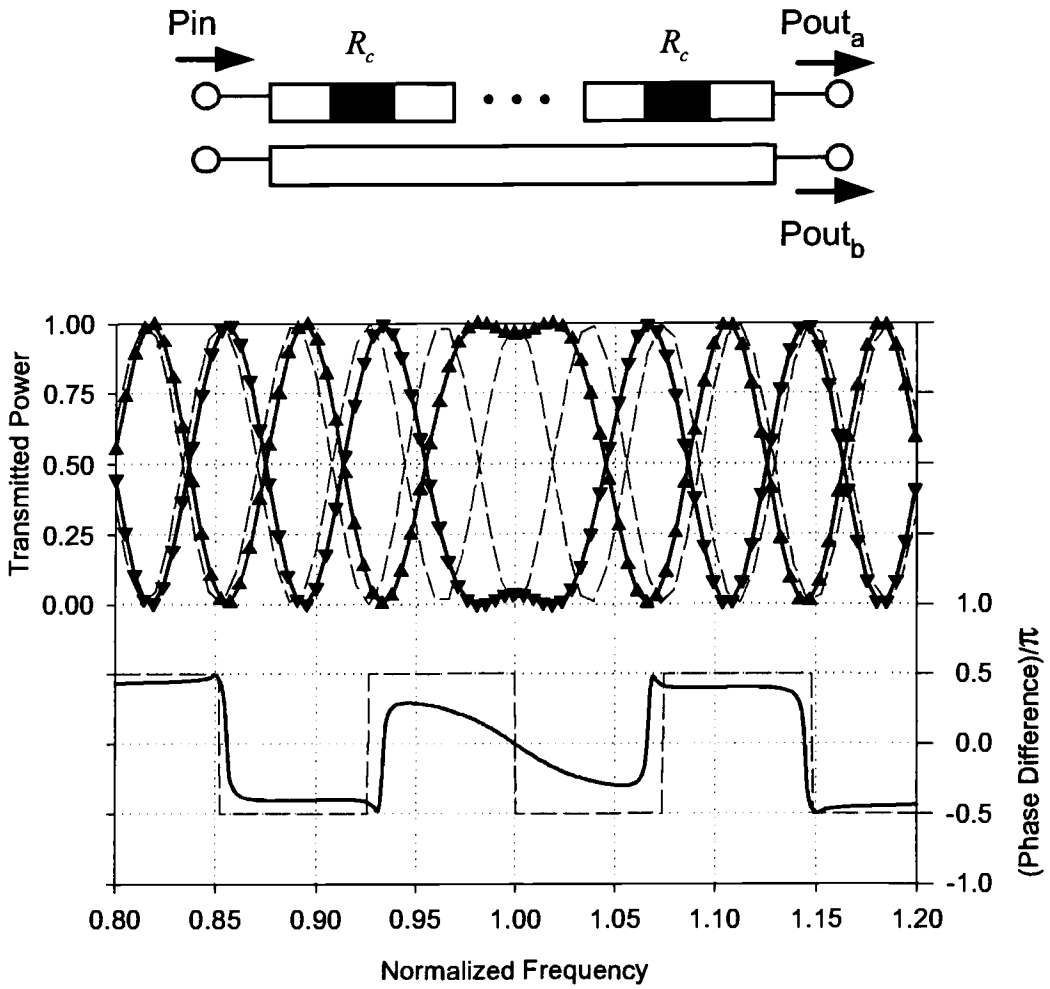

Figure 6.17 Frequency response and phase difference between the lines of 27 cascaded asymmetric coupler sections compared with symmetric coupler structure shown in Figure 6.6 (length of each section = $(\beta_e-\beta_o)\cdot L=(\beta_c-\beta_\pi)\cdot L=\pi$, $R_{c,2,4,\ldots,26}=0.9$, $R_{c,1,3,\ldots,27}=1.0$)

In this case, the response of the interferometer with 27 sections of alternately cascaded symmetric and asymmetric coupler sections with fixed values of Rc are compared with that of 27 symmetric coupler sections.

In order to quantify the phase difference between the two lines and the ripple at the center wavelength, the basic structure, shown in Figure 6.18, composed of cascaded symmetric couplers with $(\beta_e-\beta_o)\cdot l=\pi/2$ and one asymmetric coupler with $(\beta_c-\beta_\pi)\cdot L=\pi$ is considered.

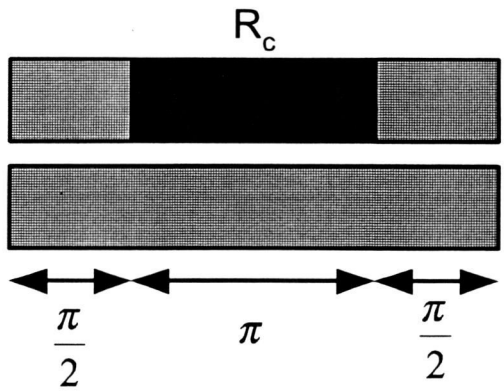

Figure 6.18 Basic interferometric coupler structure

At each section, the transfer matrix can be represented in a simplified form. The asymmetric coupler section becomes

$$\left[M^{Asym}\right]_{\phi=\frac{\theta_c-\theta_\pi}{2}=\frac{\pi}{2}} = \begin{bmatrix} -j\cdot\left(\frac{R_c^2-1}{R_c^2+1}\right) & -j\cdot\left(\frac{2R_c}{R_c^2+1}\right) \\ -j\cdot\left(\frac{2R_c}{R_c^2+1}\right) & j\cdot\left(\frac{R_c^2-1}{R_c^2+1}\right) \end{bmatrix} \tag{6.63}$$

Also, each of the attached symmetric coupler sections becomes

$$\left[M^{Symm}\right]_{\phi=\frac{\theta_e-\theta_o}{2}=\frac{\pi}{4}} = \begin{bmatrix} \frac{\sqrt{2}}{2} & -j\frac{\sqrt{2}}{2} \\ -j\frac{\sqrt{2}}{2} & \frac{\sqrt{2}}{2} \end{bmatrix} \tag{6.64}$$

By multiplying the matrix terms, the transfer matrix M_B for the basic structure can be simplified as

$$M_B = \begin{bmatrix} -\left(\frac{2R_c}{R_c^2+1}\right) - j\cdot\left(\frac{R_c^2-1}{R_c^2+1}\right) & 0 \\ 0 & -\left(\frac{2R_c}{R_c^2+1}\right) + j\cdot\left(\frac{R_c^2-1}{R_c^2+1}\right) \end{bmatrix}$$

$$= \begin{bmatrix} e^{j\varphi} & 0 \\ 0 & e^{-j\varphi} \end{bmatrix} \qquad (6.65)$$

$$\text{where } \varphi = \tan^{-1}\left(\frac{R_c^2-1}{2R_c}\right)$$

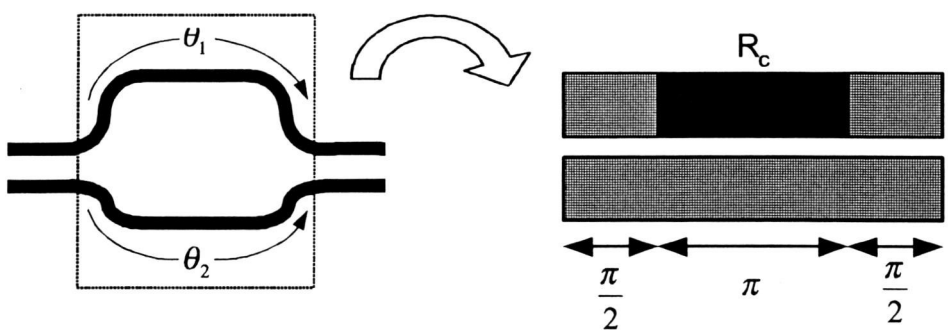

$$M_{Uncoupled} = \begin{bmatrix} e^{j\frac{\Delta\theta}{2}} & 0 \\ 0 & e^{-j\frac{\Delta\theta}{2}} \end{bmatrix} \qquad M_{Block} = \begin{bmatrix} e^{j\varphi} & 0 \\ 0 & e^{-j\varphi} \end{bmatrix}$$

Figure 6.19 Conventional and asymmetric coupler interferometric structures and corresponding transfer matrix expressions.

Figure 6.19 shows the proposed interferometric structure and corresponding transfer matrix form is shown together with the conventional structure. As seen, the phase difference terms in the diagonal elements generated by the asymmetry factor Rc play a similar role as the length difference in the conventional structure.

Since the basic interferometer block is expressed as shown in the equation (6.3), the general multisection coupler structure shown in Figure 6.20 can be characterized using this equation. The total transfer matrix for a general structure composed of m blocks of M_B shown in Figure 6.20 can be represented as

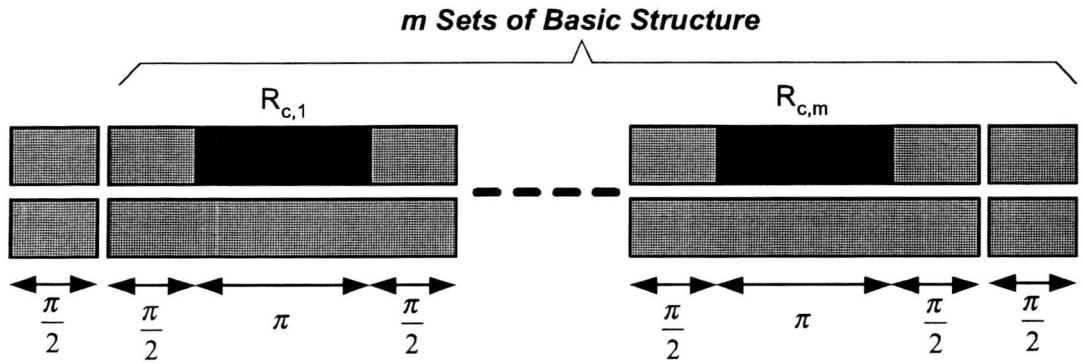

Figure 6.20 A general multisection directional coupler composed of m blocks of basic structure

$$\mathbf{M}_{f=f_o} = \begin{bmatrix} \frac{\sqrt{2}}{2} & -j\frac{\sqrt{2}}{2} \\ -j\frac{\sqrt{2}}{2} & \frac{\sqrt{2}}{2} \end{bmatrix} \begin{bmatrix} e^{j\left(\sum_{i=1}^{m}\varphi_i\right)} & 0 \\ 0 & e^{-j\left(\sum_{i=1}^{m}\varphi_i\right)} \end{bmatrix} \begin{bmatrix} \frac{\sqrt{2}}{2} & -j\frac{\sqrt{2}}{2} \\ -j\frac{\sqrt{2}}{2} & \frac{\sqrt{2}}{2} \end{bmatrix} \tag{6.66}$$

If we simplify the matrix form (6.66), the final expression becomes

$$\mathbf{M}_{f=f_o} = \begin{bmatrix} j\cdot\sin\left(\sum_{i=1}^{m}\varphi_i\right) & -j\cdot\cos\left(\sum_{i=1}^{m}\varphi_i\right) \\ -j\cdot\cos\left(\sum_{i=1}^{m}\varphi_i\right) & -j\cdot\sin\left(\sum_{i=1}^{m}\varphi_i\right) \end{bmatrix} \tag{6.67}$$

where

$$\varphi_i = \tan^{-1}\left(\frac{R_{c,i}^2 - 1}{2R_{c,i}}\right).$$

Here, two symmetric sections at the front and end of the structure with $\pi/2$ length are attached to select the power output port. That is, the total length of the structure needs to be $n\pi$ and the desired power can be expected at the through port if n is odd.

By calculating the transfer matrix for the given structure, the normalized output lightwave power in each line is determined from the equations as follows.

$$P_{out,1} = \left| j \cdot \sin\left(\sum_{i=1}^{m} \varphi_i\right)\right|^2 = \sin^2\left(\sum_{i=1}^{m} \varphi_i\right) \quad (6.68)$$

$$P_{out,2} = \left| -j \cdot \cos\left(\sum_{i=1}^{m} \varphi_i\right)\right|^2 = \cos^2\left(\sum_{i=1}^{m} \varphi_i\right) = 1 - \sin^2\left(\sum_{i=1}^{m} \varphi_i\right) \quad (6.69)$$

For example, the ripple at the center wavelength shown in Figure 6.17 can be obtained as $P_{out,1}=0.958$ and $P_{out,2}=0.042$ since $m=13$ and $R_{c,1}= \cdots =R_{c,m}=0.9$.

Using the equations provided in this section, the proposed structure is readily utilized as filter with desired output power at each line for the given wavelength. Also, the power at the receiving end has wider pass band properties than the symmetric coupler cases, as shown in Figure 6.17.

The bandpass characteristics achieved by using the concept of multisection asymmetric couplers are similar to the conventional Mach-Zehnder interferometer structure. However, the design procedure requires more careful investigation of the properties of a multi-section asymmetric coupler since it provides continuous coupling along the line. Thus, adjusting the pass band characteristics is different from that of conventional structure and expected to be more limited. In order for the multisection asymmetric coupler to act as a bandpass filter, equations (6.68~6.69) representing the transmitted power at the through port and coupled port can be utilized. Fundamentally, the pass band is confined by the total electrical length, $n\pi$, of the structure, and the ripple can be adjusted by the Rc profile.

6.6 Conclusion

In this chapter, a new closed-form transfer matrix expression for a general optical asymmetric directional coupler has been developed based on the normal mode approach. The 2x2 transfer matrix relates the complex input and output wave amplitudes as a function of electrical length and asymmetry parameter Rc. It has been shown that a single section of an asymmetric waveguide section embedded in symmetric waveguide sections, all of appropriate lengths, can produce a similar phase difference as that obtained by uncoupled waveguides of unequal lengths employed in conventional Mach-Zehnder interferometer structures. As an advantage, the asymmetric coupled interferometric structure does not require any waveguide bends and can be directly implemented in planar technology.

To illustrate the potential of the general asymmetric cascaded coupled waveguide structure as an optical filter, the wavelength-dependent properties of a multisection waveguide structure consisting of cascaded symmetric and asymmetric coupled waveguide sections have been examined. It has been demonstrated that the asymmetry parameter Rc can be used to effectively alter the wavelength-dependent characteristics of multisection coupled waveguide structures, thus making cascaded asymmetric waveguide coupler structures a viable alternative approach for a class of optical filters.

7 SUMMARY AND SUGGESTIONS FOR FURTHER RESEARCH

In this thesis a class of planar microwave and opto-electronic structures has been studied based on a rigorous field theoretic analysis approach. In the first part of the thesis a new quasi-static approach was developed to efficiently characterize single and multiple coupled interconnects on silicon substrate. It was shown that for substrates with large conductivity, such as for heavily doped CMOS substrates, the longitudinal currents in the substrate significantly affect the distributed series inductance and series resistance of the interconnect due to the substrate skin-effect. The new quasi-magnetostatic spectral domain formulation proposed in this thesis includes the longitudinal currents and accurately computes the frequency-dependent distributed series inductance and resistance parameters over a wide range of substrate conductivities. The method was further extended to multiple coupled single and multi-level interconnect structures with ground plane and multiple coupled co-planar stripline structures without ground plane. The finite conductor thickness was taken into account in terms of a stacked conductor model. The new quasi-static approach was validated by comparison with results obtained with a full-wave spectral domain method and the commercial planar full-wave electromagnetic field solver Momentum, as well as published simulation and measurement data.

In the second part of this thesis, coupled planar optical interconnect structures were investigated based on a rigorous field theoretic analysis combined with an application of the normal mode theory for coupled transmission lines. Similar to coupled transmission lines, a new transfer matrix description for a general optical directional coupler was presented. Based on this transfer matrix formulation, the wavelength-dependent characteristics of multi-section optical filters consisting of general cascaded asymmetric optical directional coupler sections were investigated. It was shown that by varying the asymmetry factors of the cascaded coupled waveguide sections, optical wavelength filters with different passband properties can be achieved In particular, a filter structure consisting of alternately cascaded symmetric and asymmetric coupled waveguide sections was investigated.

Future research work in the area of on-chip interconnect modeling should include the modeling of three-dimensional layout of interconnect lines including crossing lines. Also, the conductor loss should be included in the modeling procedure in a more rigorous way. This includes the skin-effect as well as proximity effects in the conducting strips. Furthermore, a more efficient integration algorithm with high accuracy needs to be developed since the integration procedure consumes most of the computation time of the quasi-static spectral domain methods. Especially, the entire computing time significantly increases if the number of conductor increases due to the required basis functions for accurate calculations.

In the work on optical waveguide couplers and filters, the passband characteristics for general asymmetric cascaded couplers should be analyzed in more detail. Furthermore, a design procedure including design equations for various optical filter responses should be developed.

BIBLIOGRAPHY

1. *P. E. Allen, D. R. Holberg, "CMOS Analog Circuit Design," Sauders College Publishing, 1987.*

2. *Intel Developer, "Changing the PC Platform for Another 20 Years," http://developer.intel.com/solutions/archive/issue2/focus.htm , Dec. 1994.*

3. *D. Herrel, "Power to the Package," IEEE Spectrum, pp. 46 ~ 53. July 1999.*

4. *H. Hasegawa, et al, "Properties of Microstrip Line on Si-SiO2 system," IEEE Trans. On MTT, Vol. MTT-19, pp. 869 ~ 881, Nov. 1971.*

5. *T. Itoh, "Numerical Techniques for Microwave and Millimeter-Wave Passive Structures," John Wiley & Sons, pp. 334 ~ 380, 1989.*

6. *J. Gilb, C.A. Balanis, "MIS Slow-Wave Structures over a Wide Range of Parameters," IEEE Trans. On MTT, Vol. MTT-40, pp. 2148~2154, Dec. 1992.*

7. *C. Scott, "The Spectral Domain Method in Electromagnetics," Artech House, 1989.*

8. *N. Ida, "Numerical Modeling for Electromagnetic Non-Destructive Evaluation," Chapman & Hall, 1995.*

9. *R. C. Booton Jr., "Computational Methods for Electromagnetics and Microwaves," John Wiley & Sons, 1992.*

10. *A. Ishimaru, "Electromagnetic Wave Propagation, Radiation, and Scattering," Prentice Hall, 1991.*

11. *H. J. Lee, "Computational Methods for the Quasi-TEM Characteristics of Fundamental MIC Planar Structures," Ph.D. Thesis, Oregon State University, 1983.*

12. *F. Mesa, et al, "On the Quasi-TEM and Full-Wave Approaches Applied to Coplanar Multistrip on Lossy Dielectric Layered Media," IEEE Trans. On MTT, Vol. MTT-37, pp. 484~491, Mar. 1989.*

13. *S.Y. Poh, et. al, "Approximate Formulas for Line Capacitance and Characteristic Impedance of Microstrip Line," IEEE Trans. On MTT, Vol. MTT-29, pp. 135~142. Feb. 1981.*

14. *T. Kitazawa, "Variational Method for Multiconductor Coupled Striplines with Stratified Anisotropic Media," IEEE Trans. On MTT, Vol. MTT-37, pp. 484~491. Mar. 1989.*

15. *C.W. Wei, et. al, "Multiconductor Transmission Lines in Multilayered Dielectric Media," IEEE Trans. On MTT, Vol. MTT-32, pp. 439~449. Apr. 1984.*

16. G. Plaza, et. al, "Quick Computation of [C],[L],[G], and [R] Matrices of Multiconductor and Multilayered Transmission Systems," IEEE Trans. On MTT, Vol. MTT-43, pp. 1623~1626. Jul. 1995.

17. A. Tripathi, Y.C. Hahm, A. Weisshaar and V.K. Tripathi, "A Quasi-TEM Spectral Domain Approach for Calculating Distributed Inductance and Resistance of Microstrip on Si-SiO_2 Substrate," Electronics Letter, Vol. 34, No. 13, pp. 1330 ~ 1331, Jun. 1998.

18. V.K. Tripathi, "Asymmetric Coupled Transmission Lines in an Inhomogeneous Medium," IEEE Trans. On MTT, Vol. MTT-23, pp. 734~739, Sep. 1975.

19. V.K. Tripathi, "On the Analysis of Symmetrical Three-line Microstrip Circuits," IEEE Trans. On MTT, Vol. MTT-25, pp. 726~729, Sep. 1977.

20. R.T. Kollipara and V.K. Tripathi, "Quasi-TEM Spectral Domain Technique for Multiconductor Structures with Rectangular and Trapizoidal Conductor Cross Sections," IEEE Microwave and Optical Tech. Letters, Vol. 3, No. 1, pp. 4~6, 1990.

21. J.T. Kuo, "Accurate Quasi-TEM Spectral Domain Analysis of Single and Multiple Coupled Microstrip Lines of Arbitrary Metallization Thickness," IEEE Trans. On MTT, Vol. MTT-43, pp. 1881~1888, Aug. 1995.

22. J.T. Kuo, T. Itoh, "Hybrid-Mode Computation of Propagation and Attenuation Characteristics of Parallel Coupled Microstrips with Finite Metallization Thickness," IEEE Trans. On MTT, Vol. MTT-45, pp. 274~280, Feb. 1997.

23. W. Heinrich, "Full-wave Analysis of Conductor Losses on MMIC Transmission Lines," IEEE Trans. On MTT, Vol. MTT-38, No. 10, pp. 1468~1472, Oct. 1990.

24. R. D. Lutz, Y. Hahm, A. Weisshaar, V. K. Tripathi, A. Grzegorek, W. McFarland, and J. Meyer, "Modeling of Spiral Inductors on Lossy Substrates for RFIC Applications," IEEE, MTT-S, pp. 1855-1858, 1998.

25. R. D. Lutz, Y. Hahm, A. Weisshaar, V. K. Tripathi, A. Grzegorek, W. McFarland, and J. Meyer, "Modeling of Spiral Inductors on Lossy Substrates for RFIC Applications," 1998 IEEE Radio Frequency Integrated Circuits Symposium Digest of Papers, pp. 313-316, 1998.

26. J.Zheng, A.Tripathi, Y.-C.Hahm, T.Ishii, A.Weisshaar, and V.K.Tripathi, "CAD-Oriented Equivalent Circuit Modeling of On-Chip Interconnects in CMOS Technology," IEEE 7th Topical Meeting on Electrical Performance of Electronic Packaging (EPEP'98), pp.227-230, Oct. 1998.

27. S.-J. Fang, et. al, "Analysis of Asymmetric Coplanar Waveguide with Conductor Backing," IEEE Trans. On MTT, Vol. MTT-47, No. 2, pp. 238~240, Feb. 1999.

28. *E. Drake, et al, "Improved Quasi-TEM Spectral Domain Analysis of Boxed Coplanar Multiconductor Microstrip Lines," IEEE Trans. On MTT, Vol. MTT-41, No. 2, pp. 260~267, Feb. 1993.*

29. *A.K. Bhattacharyya, "Electromagnetic Fields in Multilayered Structures, Theory and Applications," Artech House, 1994.*

30. *D.K. Cheng, "Field and Wave Electronagnetics," 2nd ed. Addision-Wesley, 1989.*

31. *Y.R. Kwon, et al, "Quasi-TEM Analysis of "Slow-Wave" Mode Propagation on Coplanar Microstructure MIS Transmission Lines," IEEE Trans. On MTT, Vol. MTT-35, No. 6, pp. 545~551, Jun. 1987.*

32. *V. Milanovic', et. al, "Characterization of Broad-Band Transmission for Coplanar Waveguides on CMOS Silicon Substrates," IEEE Trans. On MTT, Vol. MTT-46, pp. 632~640, May. 1998.*

33. *J.E. Midwinter, "Digital Optics, Smart Interconnect or Optical Logic?" Phys. Tech., Vol. 19, No. 3, pp. 101~108, May. 1988.*

34. *M.R. Feldman, et. al., "Comparison between Optical and Electrical Interconnects Based on Power and Speed Considerations," Appl., Opt., Vol. 27, No. 9, pp. 1742 ~ 1751, May. 1998.*

35. *C.H. Henry, et. al, "Solution of the Scalar Wave Equation for Arbitrary Shaped Dielectric Waveguides by Two-Dimensional Fourier Analysis," Journal of Lightwave Tech., Vol. 7, No. 2, pp. 308 ~ 313, Feb. 1989.*

36. *Y.P Li, et. al, "Silica-based Optical Integrated Circuits," IEE Proc-Optoelectron., Vol. 143, No. 5, pp. 263 ~ 280, Oct. 1996.*

37. *T. Rozzi and M. Mongiardo, "Open Electromagnetic Waveguides," Rhort Run Press, 1997.*

38. *A. Weisshaar, "Impedance Boundary Method of Moments for Accurate and Efficient Analysis of Planar Graded-Index Optical Waveguides," Journal of Lightwave Tech., Vol. 12, No. 11, pp. 1943 ~ 1951, Nov. 1994.*

39. *K.A Remley, A. Weisshaar, "Impedance Boundary Method of Moments with Extended Boundary Conditions," Journal of Lightwave Tech., Vol. 13, No. 12, pp. 2372~2377, Dec. 1995.*

40. *H. Chang, "Analysis of Linear and Nonlinear Coupled Dielectric Waveguide," Ph.D. Thesis, Oregon State University, 1993.*

41. *S. Lim, "Design, Fabrication, and Testing of Inhomogeneous Dielectrics," Ph.D. Thesis, Oregon State University, 1993.*

42. *A. Thelen, "Design of Optical Interference Coating," McGraw-Hill, 1989.*

43. *K.J. Kuhn, "Laser Engineering," Prentice-Hall, 1998.*

44. *M.J. Maron, et. al., "Numerical Analysis, A Practical Approach," 3rd ed. Wadsworth,1991*

45. *W.H. Press, et. al., "Numerical Recipes in C," Cambridge Univ. Press, 1998.*

46. *G.J. Borse, "Numerical Methods with Matlab, A Resource for Science and Engineers," PWS Publishing Company, 1997.*

47. *K.E. Atkinson, "An Introduction to Numerical Analysis," 2nd ed. John Wiley & Sons, 1989.*

48. *C.F. Gerald, et. al., "Applied Numerical Analysis," 4th ed.. Addison-Wesley, 1989.*

49. *S.S.M Wong, "Computational Methods in Physics & Engineering," Prentice Hall, 1992.*

50. *P.A. Rizzi, "Microwave Engineering, Passive Circuits," Prentice-Hall, 1988.*

51. *R. D Lutz, Y.C. Hahm, A. Weisshaar and V. K. Tripathi, "Modeling and Analysis of Spiral Inductors for RFICs", IEEE MTT-s '99 Int'l Microwave Symp. Digest. pp. 43~46, June 1999.*

52. *J. Zheng, Y.C. Hahm, A. Weisshaar and V.K. Tripathi. "CAD-Oriented Equivalent Circuit Modeling of On-Chip Interconnects for RF Integrated Circuits in CMOS Technology", IEEE MTT-s '99 Int'l Microwave Symp. Digest. pp. 35~38, June 1999.*

53. *H. Toshiyoshi, et. al, "Design and Analysis of Micromechanical Tunable Interferometers for WDM Free-Space Optical Interconnection," IEEE Journal of Lightwave Tech., Vol.17, No. 1, Jan. 1999.*

54. *D.M. Pozar, "Microwave Engineering," Addison-Wesley, 1990.*

55. *R.E Collin, "Foundations for Microwave Engineering," 2nd ed. McGraw-Hill Int'l.,1992.*

56. *K. Jinguji and M. Kawachi, "Synthesis of Coherent Two-Port Lattice-From Optical Delay-Line Circuit," Journal of Lightwave Tech., Vol. 13, No. 1, Jan. 1995.*

57. *B. J. Luff, et. al, "Integrated Optical Mach-Zehnder Biosensor," Journal of Lightwave Tech., Vol. 16, No. 4, Apr. 1998.*

58. *J. Kobayashi, et. al, "Directional Couplers Using Fluorinated Polymide Waveguides," Journal of Lightwave Tech., Vol. 16, No. 4, Apr. 1998.*

59. *M. H. Hu, et. al, "An Integrated Two-Stage Cascaded Mach-Zehnder Device in GaAs," Journal of Lightwave Tech., Vol. 16, No. 8, Aug. 1998.*

60. *H. Bulthuis, "Simulation of a Directional Coupler Optical Filter," BBV application Note, Aug. 1997.*

61. *R. Marz, "Integrated Optics, Design and Modeling," Artech, 1994.*

62. *B. Scaife, "Principles of Dielectrics," Clarendon Press-Oxford, 1989.*

63. *T.-C. Mu, et. al, "Characteristics of Multiconductor, Asymmetric, Slow-Wave Microstrip Transmission Lines," IEEE Trans. On MTT, Vol. MTT-34, No. 12, pp. 1471~1477, Dec. 1986.*

64. *T. Itoh, "Spectral Domain Immitance Approach for Dispersion Characteristics of Generalized Printed Transmission Lines," IEEE Trans. On MTT, Vol. MTT-28, No. 7, pp. 733~736, Jul. 1980.*

65. *V. K. Tripathi, et. al, "Spectral-Domain Computation of Characteristic Impedances and Multiport Paramaters of Multiple Coupled Microstrip Lines," IEEE Trans. On MTT, Vol. MTT-37, No. 1, pp. 215~221, Jan. 1989.*

66. *J.P.K. Gilb, A. Balanis, "Asymmetric, Multi-Conductor Low-Coupling Structures for High-Speed, High-Density Digital Interconnects," IEEE Trans. On MTT, Vol. MTT-39, No. 12, pp. 2100~2106, Dec. 1991.*

67. *J. Zheng, Y.-C. Hahm, A. Weisshaar and V.K. Tripathi, "Equivalent Circuit Modeling of Single and Coupled On-Chip Interconnects on Lossy Silicon Substrate," 8th Topical Meeting on Electrical Performance of Electronics Packaging (EPEP '99), San Diego, CA, 1999.*

68. *G. Sundburg, R. D. Lutz, Y.C. Hahm, R.K. Settaluri, J. Zheng, A. Weissharr and V.K. Tripathi, "Modeling of General Non-Uniform On-Chip Interconnect Structures," 32nd International Symp. on Microelectronics (IMAPS'99),Chicago, IL, Oct. 1999.*

69. *Takato, N., et. al, " Silica-basedintegrated optic Mach-Zehnder multi/demultiplexer family with channel spacing of 0.01-250nm," IEEE Journal of Selected Areas Commun., 1990, Vol. 8, pp. 1120~1127.*

70. *H.A. Wheeler, "Transmission-Line Properties of a Strip Line Between Parallel Planes." 1978 Trans. on MTT, Vol. 26, No. 11, pp. 866~876, Nov. 1978.*

71. *E. Groteluschen, L.S. Dutta, and S. Zagge, "Full-wave Analysis and Analytical Formulas for the Line Parameters of Transmission Lines on Semiconductor Substrates", Integration, the VLSI Journal, Vol. 16, pp. 33~58, 1993.*

72. *J-K Wee, et. al, " Modeling the substrate effect in interconnect line characteristics of high speed VLSI circuits," IEEE Trans. On MTT, Vol. MTT-46, No. 10, pp. 1436~1443, Oct. 1998.*

73. *D.F. Williams, "Metal-Insulator-Semiconductor Transmission Lines," IEEE Trans. On MTT, Vol. MTT-47, pp. 176~181, Feb. 1999.*

APPENDICES

1. Fourier Transformation Table

$f(t)=\frac{1}{2\pi}\int_{-\infty}^{\infty}F(\alpha)e^{j\omega t}d\omega$	$F(\alpha)=\int_{-\infty}^{\infty}f(t)e^{-j\omega t}dt$
$\delta(t)$	1
$f(at)$	$\frac{1}{\lvert a\rvert}F\left(\frac{\alpha}{a}\right)$
$f(t-t_o)$	$F(\alpha)e^{-j\alpha t_o}$
$f^*(t)$	$F^*(-\alpha)$
$\frac{d^n}{dt^n}f(t)$	$(j\alpha)^n F(\alpha)$
$(-jt)^n f(t)$	$\frac{d^n}{d\alpha^n}F(\alpha)$
$\int_{-\infty}^{\infty}f_1(\tau)f_2(t-\tau)d\tau$	$F_1(\alpha)F_2(\alpha)$
$\int_{-\infty}^{\infty}f(t+\tau)f^*(\tau)d\tau$	$\lvert F(\alpha)\rvert^2$
$\int_{-\infty}^{\infty}\lvert f(t)\rvert^2 dt=\frac{1}{2\pi}\int_{-\infty}^{\infty}\lvert F(\alpha)\rvert^2 d\alpha$	
$\sum_{n=-\infty}^{\infty}f(t+nT)=\frac{1}{T}\sum_{n=-\infty}^{\infty}F\left(\frac{2\pi n}{T}\right)e^{j2\pi nt/T}$	
$J_n(t)$	$\begin{cases}\frac{2\cdot Cos(n\cdot Arc\sin(\alpha))}{\sqrt{1-\alpha^2}} & n:even \quad \lvert\alpha\rvert<1\\ -\frac{2j\cdot Sin(n\cdot Arc\sin(\alpha))}{\sqrt{1-\alpha^2}} & n:odd \quad \lvert\alpha\rvert<1\\ 0 & \lvert\alpha\rvert<1\end{cases}$
$\frac{T_n(t)}{\sqrt{1-t^2}}$	$\pi(-j)^n J_n(\alpha)$
$\sqrt{1-t^2}U_{n-1}(t)$	$n\pi(-j)^{n+1}\frac{J_n(\alpha)}{\alpha}$
$C-\frac{1}{\pi}\ln\lvert t\rvert$	$\frac{1}{\alpha}$

2. Properties Of Bessel Function Of The 1st Kind Of Order N

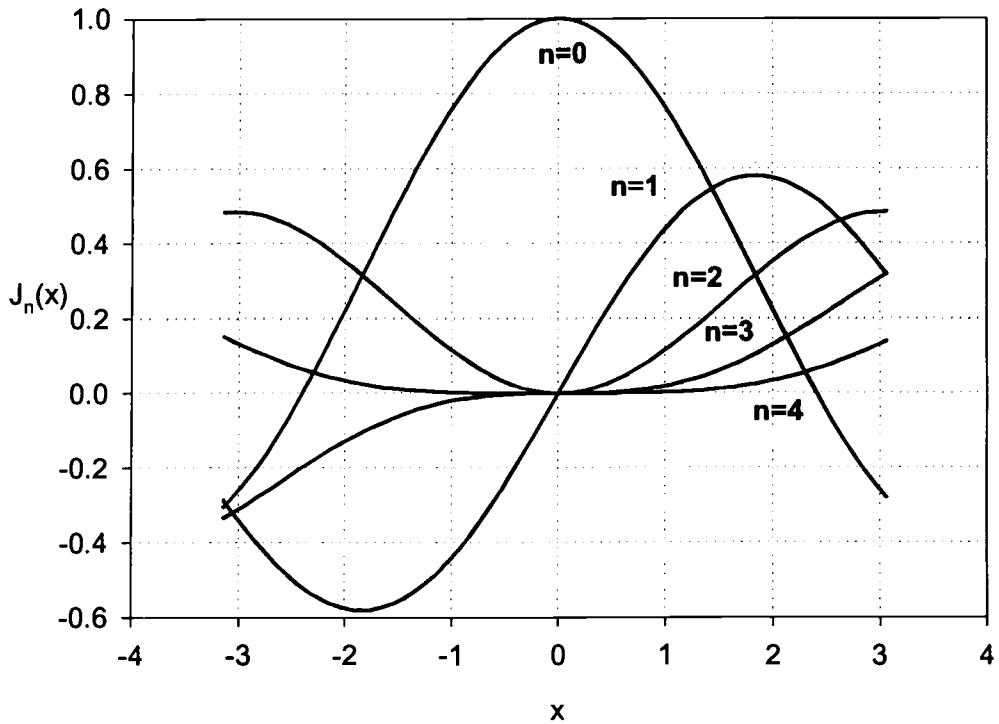

$$x^2y'' + xy' + (x^2 - n^2)y = 0 \quad n \geq 0 \tag{A. 1}$$

$$J_0(x) = \frac{1}{\pi}\int_0^{\pi} Cos(x \cdot Sin\theta)d\theta \tag{A. 2}$$

$$J_{n+1}(x) = \frac{2n}{x}J_n(x) - J_{n-1}(x) \tag{A. 3}$$

$$J_{-n}(x) = (-1)^n J_n(x) \tag{A. 4}$$

$$J_n(x) \approx \sqrt{\frac{2}{\pi x}}Cos\left(x - \frac{n\pi}{2} - \frac{\pi}{4}\right) \text{ where, } x \text{ is large} \tag{A. 5}$$

$$J_n(x) \approx \sqrt{\frac{1}{2\pi n}}\left(\frac{ex}{2n}\right)^n \text{ where, } n \text{ is large} \tag{A. 6}$$

3. Properties of Chebyshev Polynomials

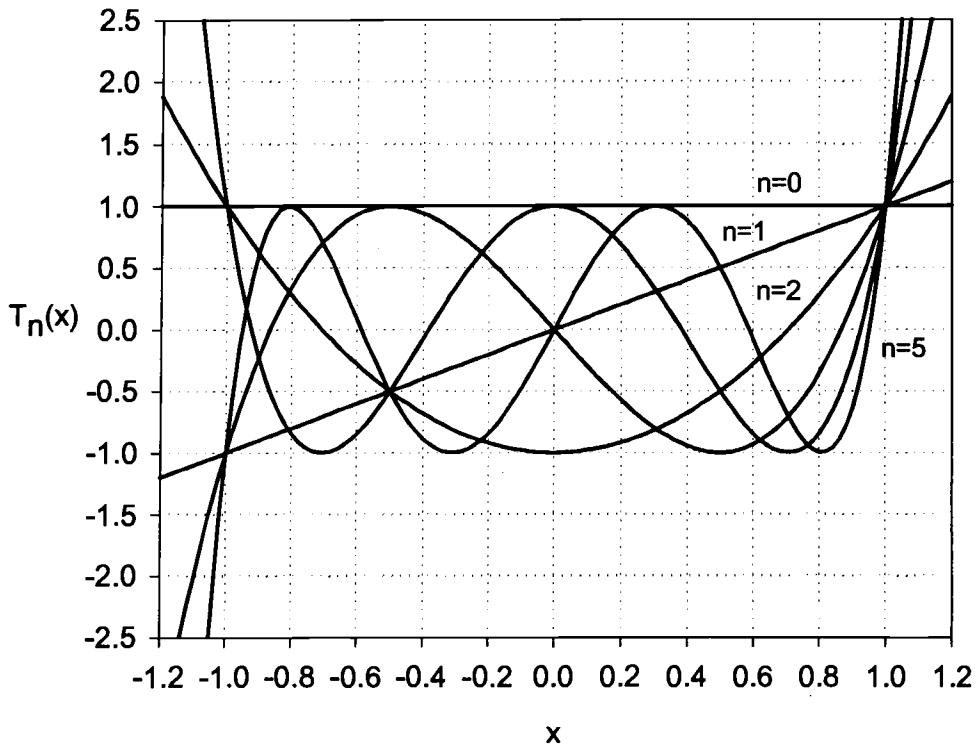

$$(1-x^2)y''-xy'+n^2y=0 \text{ where, } n=0,1,2,.. \tag{A. 7}$$

$$T_n(x)=Cos\left(n\cdot Cos^{-1}x\right) \tag{A. 8}$$

$$T_0(x)=1 \text{ and } T_n(1)=1 \tag{A. 9}$$

$$T_n(-x)=(-1)^n T_n(x) \tag{A. 10}$$

$$\int_{-1}^{1}\frac{T_m(x)T_n(x)}{\sqrt{1-x^2}}dx=0 \text{ where, } m\neq n \tag{A. 11}$$

$$\int_{-1}^{1}\frac{T_n{}^2(x)}{\sqrt{1-x^2}}dx=\begin{cases}\pi & if \quad n=0\\ \pi/2 & if \quad n\neq 0\end{cases} \tag{A. 12}$$

4. Properties of Legendre Polynomials

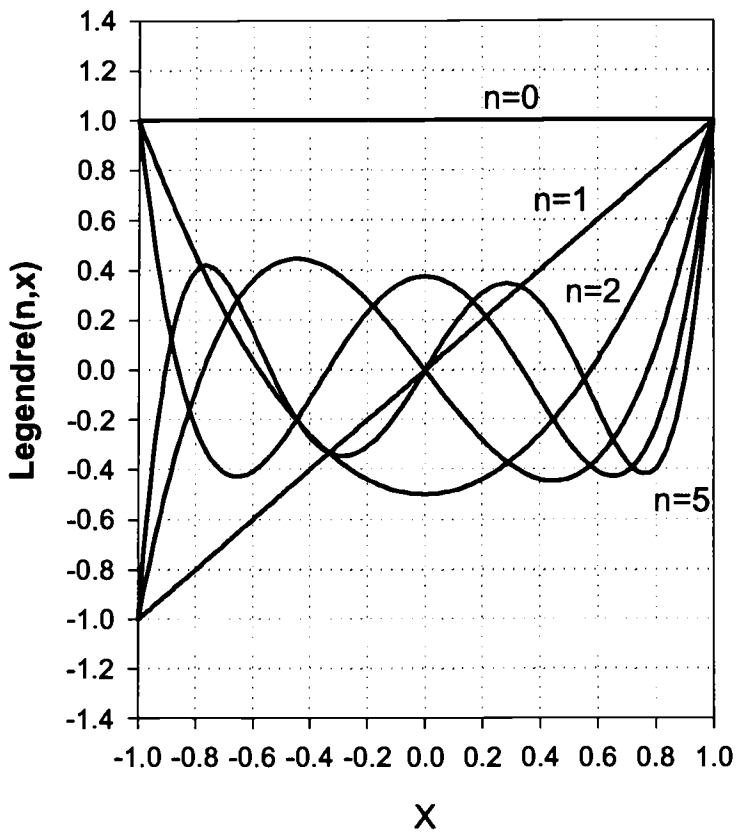

$$(1-x^2)y''-2xy'+n(n+1)y=0 \qquad \text{(A. 13)}$$

$$P_n(x)=\frac{1}{2^n n!}\frac{d^n}{dx^n}\left(x^2-1\right)^n \qquad \text{(A. 14)}$$

$$P_0(x)=1 \text{ and } P_n(1)=1 \qquad \text{(A. 15)}$$

$$\int_{-1}^{1} P_m(x)P_n(x)dx=1 \text{ where, } m\neq n \qquad \text{(A. 16)}$$

$$\int_{-1}^{1} P_n{}^2(x)dx=\frac{2}{2n+1} \qquad \text{(A. 17)}$$

$$P'_{n+1}(x)-P'_{n-1}(x)=(2n+1)P_n(x) \qquad \text{(A. 18)}$$

5. *The Conductivity of Commonly Used Metal and Other Dielectric Material[55]*

Material	σ[S/m]
Silver	6.12×10^7
Copper	5.80×10^7
Gold	4.10×10^7
Aluminum	3.54×10^7
Brass	1.50×10^7
Nickel	1.15×10^7
Iron	1.04×10^7
Bronze	1.00×10^7
Stainless Steel	0.11×10^7
Nichrome	0.09×10^7

freq=3.0GHz

Material	ε_r	tan δ
Air	1.0006	-
Alumina	9.6	0.0001
Glass	4~7	0.001~0.006
Mica	5.4	0.0003
Polystyrene	2.55	0.0003
Quartz	3.8	0.00006
Rexolite-1422	2.54	0.0005
Styrofoam	1.03	0.0001
Teflon	2.1	0.00015
Titanium Dioxide	96	0.001
Boron Nitride	5.12	
Silicon(Si)	11.7~12.9	0.001~0.003
Germanium(Ge)	16	
Gallium Arsenide (GaAs)	12.9	0.0005~0.001
Alumina	9.6~10.1	0.0005~0.002
Sapphire	9.4	0.0002
Beryllium Oxide	6.7	0.001~0.002

6. Full-wave Spectral Domain Method [5~8]

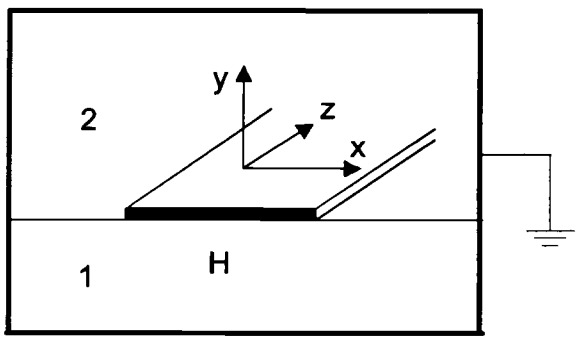

The wave propagating mode of this structure can be represented by superposition of TE and TM modes corresponding to two potential functions.

$$\begin{aligned}\mathbf{E} &= \mathbf{E}^e + \mathbf{E}^h \\ \mathbf{H} &= \mathbf{H}^e + \mathbf{H}^h\end{aligned} \tag{A. 19}$$

where

$$\begin{cases}\mathbf{E}^h = -j\omega\mu\nabla\times(\hat{\mathbf{k}}\psi^h e^{-\gamma z}) \\ \mathbf{H}^e = -j\omega\mu\nabla\times(\hat{\mathbf{k}}\psi^e e^{-\gamma z})\end{cases} \tag{A. 20}$$

Here, $\hat{\mathbf{k}}\psi^h e^{\gamma z}$ is the magnetic Hertzian potential and $\hat{\mathbf{k}}\psi^e e^{\gamma z}$ is the electric Herztian potential.

From Maxwell's equation, the time-varying wave equation in terms of both potentials are given as

$$\begin{aligned}\nabla\times\mathbf{H}^h &= j\omega\varepsilon\mathbf{E}^h \\ \nabla\times\mathbf{H}^e &= j\omega\varepsilon\mathbf{E}^e\end{aligned} \longrightarrow \begin{aligned}\nabla^2\psi^h + (\omega^2\mu\varepsilon - \beta^2)\psi^h &= 0 \\ \nabla^2\psi^e + (\omega^2\mu\varepsilon - \beta^2)\psi^e &= 0\end{aligned} \tag{A. 21}$$

where $\gamma = \pm j\beta = \pm j(\beta' + j\beta'')$ is unknown.

The wave equation for the specific structure shown above changes as follows. Since the media along the x axis are the same, this axis is changed into the spectral domain, α.

$$J_n(x) \approx \sqrt{\frac{2}{\pi x}} Cos\left(x - \frac{n\pi}{2} - \frac{\pi}{4}\right) \tag{A. 22}$$

$$\frac{d^2}{dy^2}\tilde{\psi}^e + (\omega^2\mu\varepsilon - \beta^2 - \alpha^2)\tilde{\psi}^e = 0 \tag{A. 23}$$

At $y=H$, the boundary conditions in terms of the tangential field components and current distribution are given as

$$\begin{aligned}
&\tilde{E}_{z1}(\alpha, H) = \tilde{E}_{z2}(\alpha, H) \\
&\tilde{E}_{x1}(\alpha, H) = \tilde{E}_{x2}(\alpha, H) \\
&\tilde{H}_{z1}(\alpha, H) - \tilde{H}_{z2}(\alpha, H) = -\tilde{J}_x(\alpha) \\
&\tilde{H}_{x1}(\alpha, H) - \tilde{H}_{x2}(\alpha, H) = \tilde{J}_z(\alpha)
\end{aligned} \tag{A. 24}$$

Here, $\tilde{E}_{xi}$ and $\tilde{G}_{\phi}(\alpha)$ are determined from the normal field component, $\tilde{E}_{zi}$ and $\tilde{H}_{zi}$ using the relations

$$\begin{aligned}
&-j\omega\mu\tilde{H}_x - j\beta\tilde{E}_y = \partial\tilde{E}_z / \partial y \\
&-j\omega\mu\tilde{H}_y + j\beta\tilde{E}_x = -\partial\tilde{E}_z / \partial x \\
&j\omega\varepsilon\tilde{E}_x - j\beta\tilde{H}_y = \partial\tilde{H}_z / \partial y \\
&j\omega\varepsilon\tilde{E}_y + j\beta\tilde{H}_x = \partial\tilde{H}_z / \partial x
\end{aligned} \tag{A. 25}$$

and

$$\begin{aligned}
\tilde{H}_z &= (\omega^2\mu\varepsilon - \beta^2)\psi^h e^{\gamma z} \\
\tilde{E}_z &= (\omega^2\mu\varepsilon - \beta^2)\psi^e e^{\gamma z}
\end{aligned} \tag{A. 26}$$

Thus, all the field distributions can be expressed in terms of tangential current components. If we derive the relations between the tangential electric fields and tangential current components, we obtain

$$\begin{bmatrix} \tilde{E}_{z2}(\alpha,\beta) \\ \tilde{E}_{x2}(\alpha,\beta) \end{bmatrix} = \begin{bmatrix} \tilde{Z}_{zz}(\alpha,\beta) & \tilde{Z}_{zx}(\alpha,\beta) \\ \tilde{Z}_{xz}(\alpha,\beta) & \tilde{Z}_{xx}(\alpha,\beta) \end{bmatrix} \begin{bmatrix} \tilde{J}_{z}(\alpha,\beta) \\ \tilde{J}_{x}(\alpha,\beta) \end{bmatrix} \tag{A. 27}$$

The impedance matrix is changed into the following equation after a coordinate transformation in which the actual tangential current direction is divided into x and y components.

$$\begin{bmatrix} \tilde{E}_{z2}(\alpha,\beta) \\ \tilde{E}_{x2}(\alpha,\beta) \end{bmatrix} = \frac{1}{\alpha^2+\beta^2} \begin{bmatrix} \tilde{Z}^e\alpha^2+\tilde{Z}^h\beta^2 & (\tilde{Z}^e-\tilde{Z}^h)\alpha\beta \\ (\tilde{Z}^e-\tilde{Z}^h)\alpha\beta & \tilde{Z}^e\beta^2+\tilde{Z}^h\alpha^2 \end{bmatrix} \begin{bmatrix} \tilde{J}_{z}(\alpha,\beta) \\ \tilde{J}_{x}(\alpha,\beta) \end{bmatrix} \tag{A. 28}$$

where,

$$\tilde{Z}_e = \frac{\dfrac{\gamma_1}{j\omega\varepsilon_{c1}}\dfrac{\gamma_2}{j\omega\varepsilon_{c2}}}{\dfrac{\gamma_1}{j\omega\varepsilon_{c1}}\coth(\gamma_2 H_2)+\dfrac{\gamma_2}{j\omega\varepsilon_{c2}}\coth(\gamma_1 H_1)} \tag{A. 29}$$

$$\tilde{Z}_h = \frac{1}{\dfrac{j\omega\mu_1}{\gamma_1}\coth(\gamma_1 H_1)+\dfrac{j\omega\mu_1}{\gamma_2}\coth(\gamma_2 H_2)} \tag{A. 30}$$

and

$$\gamma_i^{\,2} = \omega^2\mu_i\varepsilon_i - \beta^2 - \alpha^2$$

The input impedance for the full-wave Green's function used in the previous equation can be obtained from the transmission line approach. That is,

$$\tilde{Z}_{in} = \tilde{Z}_{oi} \frac{\tilde{Z}_L \coth(\gamma_i H_i) + \tilde{Z}_{oi}}{\tilde{Z}_{oi} \coth(\gamma_i H_i) + \tilde{Z}_L} \tag{A. 31}$$

where

$$Z_{oi} = \begin{cases} \dfrac{\gamma_i}{j\omega\varepsilon_{ci}} & for\, \tilde{Z}_e \\ \dfrac{j\omega\mu_i}{\gamma_i} & for\, \tilde{Z}_h \end{cases} .$$

In Galerkin's procedure, the inner product of these functions and basis functions, which approximate the unknown tangential current components, leads to the linear set of equations given as

$$\begin{bmatrix} & \\ \mathbf{K} & \\ & \end{bmatrix} \begin{bmatrix} \mathbf{c} \\ - \\ \mathbf{d} \end{bmatrix} = \begin{bmatrix} \mathbf{0} \end{bmatrix} \tag{A. 32}$$

where

$$\begin{bmatrix} & \\ \mathbf{K} & \\ & \end{bmatrix} = \begin{bmatrix} \int_\alpha \tilde{J}_{zk}(\alpha)\tilde{Z}_{zz}(\alpha)\sum_{m=1}^{N} c_m \tilde{J}_{zm}(\alpha)d\alpha & \int_\alpha \tilde{J}_{zk}(\alpha)\tilde{Z}_{zx}(\alpha)\sum_{m=1}^{M} d_m \tilde{J}_{xm}(\alpha)d\alpha \\ \int_\alpha \tilde{J}_{zl}(\alpha)\tilde{Z}_{xz}(\alpha)\sum_{m=1}^{N} c_m \tilde{J}_{zm}(\alpha)d\alpha & \int_\alpha \tilde{J}_{xl}(\alpha)\tilde{Z}_{xx}(\alpha)\sum_{m=1}^{M} d_m \tilde{J}_{xm}(\alpha)d\alpha \end{bmatrix} \tag{A. 33}$$

$$\begin{aligned} \tilde{J}_z &= \sum_{n=1}^{N} c_n \tilde{J}_{zn}(\alpha) \\ \tilde{J}_x &= \sum_{m=1}^{M} d_m \tilde{J}_{xm}(\alpha) \end{aligned} \tag{A. 34}$$

K: (N+M) x (N+M) matrix, k=1~N, l=1~M

In order to find the non-trivial solutions to this system of equations, a root-seeking procedure is carried to solve

$$Det[\mathbf{K}(\beta)]=0 \quad \text{where, } \beta=\beta'-j\beta'' \tag{A. 35}$$

Also, the basis functions for the current distributions used in this procedure are given as follows. For the single line case,

$$J_{zn}(x)=\frac{\cos\left[\dfrac{2(n-1)\pi x}{W}\right]}{\sqrt{1-\left(\dfrac{2x}{W}\right)^2}} \tag{A. 36}$$

and

$$J_{xm}(x)=\frac{\sin\left[\dfrac{2n\pi x}{W}\right]}{\sqrt{1-\left(\dfrac{2x}{W}\right)^2}} \tag{A. 37}$$

Similarly, the basis function for symmetric coupled line can be represented as follows.

$$\tilde{J}_{z\begin{cases}even\\odd\end{cases}}=\sum_{m=1}^{N}c_m\tilde{J}_{zm}(\alpha)\begin{cases}\cos\left(\dfrac{W+S}{2}\alpha\right)\\ \sin\left(\dfrac{W+S}{2}\alpha\right)\end{cases} \tag{A. 38}$$

and

$$\tilde{J}_{x\begin{cases}even\\odd\end{cases}}=\sum_{m=1}^{N}d_m\tilde{J}_{xm}(\alpha)\begin{cases}\cos\left(\dfrac{W+S}{2}\alpha\right)\\ \sin\left(\dfrac{W+S}{2}\alpha\right)\end{cases} \tag{A. 39}$$

Once the propagation constant is obtained, the corresponding currents and field distributions can be calculated. Then, the characteristic impedance can be calculated using Poynting theorem associated with the field distributions.

- Example

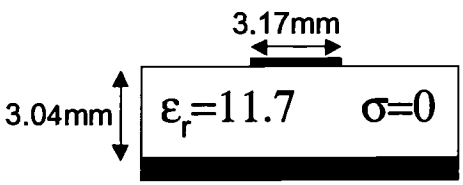

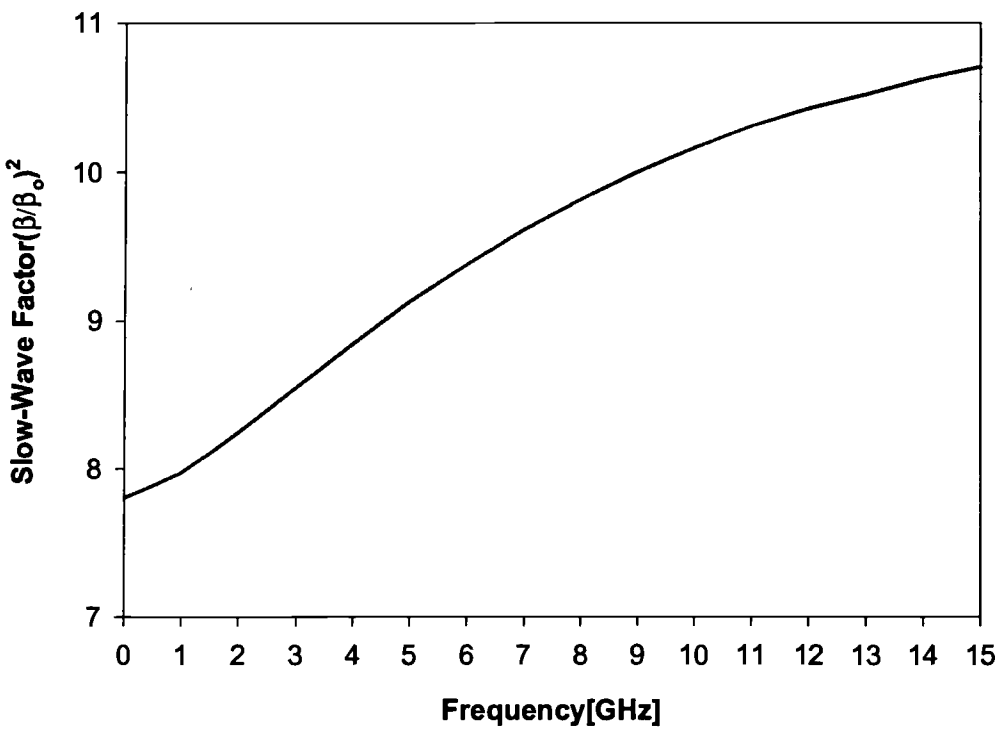

7. Muller's Method for Root Finding in Complex Plane Used in Full-Wave SDM [44]

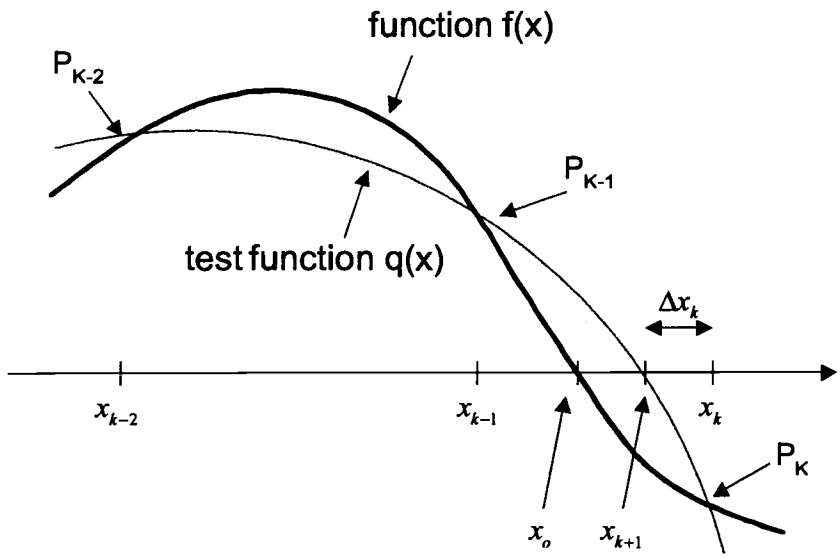

For a given function *f(x)*, an approximating 2nd order test function *q(x)* is employed with unknown coefficients.

$$q(x) = a(x - x_k)^2 + b(x - x_k) + c \tag{A. 40}$$

Each unknown coefficient of this test function can be approximated by interpolating three arbitrarily chosen points, x_{k-1}, x_k and x_{k+1}.

$$a = \frac{\dfrac{\Delta y_{k-1}}{\Delta x_{k-1}} - \dfrac{\Delta y_{k-2}}{\Delta x_{k-2}}}{\Delta x_{k-1} + \Delta x_{k-2}}, \quad b = a\Delta x_{k-1} + \frac{\Delta y_{k-1}}{\Delta x_{k-1}} \quad \text{and} \quad c = y_k \tag{A. 41}$$

where $\Delta x_{k-2} = x_{k-1} - x_{k-2}$, $\Delta x_{k-1} = x_k - x_{k-1}$, $\Delta y_{k-2} = y_{k-1} - y_{k-2}$, $\Delta y_{k-1} = y_k - y_{k-1}$ and $q(x_k) = y_k$, $q(x_{k-1}) = y_{k-1}$, $q(x_{k-2}) = y_{k-2}$.

By re-writing the test function,

$$q(x) = a(x - x_k)^2 + b(x - x_k) + c \rightarrow q(x) = a(\Delta x)^2 + b(\Delta x) + c \qquad \text{(A. 42)}$$

where $\Delta x = x - x_k$.

To make $q(x)=0$, Δx is given as

$$\Delta x = \frac{-b \pm \sqrt{b^2 - 4ac}}{2a} \qquad \text{(A. 43)}$$

Since this guess is not the root of the function, the next guess can be obtained from the following relations so that it approaches the root.

$$x_{k+1} = x_k + \Delta x_k . \qquad \text{(A. 44)}$$

8. Derivation of Equation for Vector Magnetic Potential

The time varying electric and magnetic fields can be represented by Maxwell's equations.

$$\nabla \times \mathbf{E} = -\frac{d}{dt}\mathbf{B} \qquad \text{(A. 45)}$$

$$\nabla \times \mathbf{H} = \mathbf{J} \qquad \text{(A. 46)}$$

In equation (A.46), the current term is composed of the displacement and conduction current. Also, the conduction current consists of source and conduction currents due to magnetic induction. Thus, the current term can be represented as follows.

$$\mathbf{J} = \varepsilon \frac{d}{dt}\mathbf{E} + \mathbf{J}_{C,induced} + \mathbf{J}_{C,source} \qquad \text{(A. 47)}$$

In addition, the magnetic field and the magnetic vector potential have the following relation.

$$\nabla \times \mathbf{A} = \mathbf{B} \tag{A. 48}$$

If equation (A.48) is inserted into (A.45), the following relation between the electric field and magnetic vector potential can be readily derived.

$$\nabla \times \mathbf{E} = -\frac{d}{dt}\mathbf{B} = -\frac{d}{dt}(\nabla \times \mathbf{A})$$

$$\therefore \mathbf{E} = -\frac{d}{dt}\mathbf{A} \tag{A. 49}$$

Also, equation (A.49) can be represented as follows.

$$\nabla \times \mathbf{H} = \frac{1}{\mu}\nabla \times (\nabla \times \mathbf{A}) = -\frac{1}{\mu}\nabla^2 \mathbf{A}$$

$$= \varepsilon \frac{d}{dt}\mathbf{E} + \sigma \mathbf{E} + \mathbf{J}_{C,source}$$

$$= -\varepsilon \frac{d^2}{dt^2}\mathbf{A} - \sigma \frac{d}{dt}\mathbf{A} + \mathbf{J}_{C,source} \tag{A. 50}$$

Since the field is quasi-magnetostatic, the first term (displacement current) can be ignored. Thus,

$$\frac{1}{\mu}\nabla^2 \mathbf{A} = \sigma \frac{d}{dt}\mathbf{A} - \mathbf{J}_{C,source} \tag{A. 51}$$

Finally, the equation can be re-written in the following form.

$$\nabla^2 \mathbf{A} - j\omega\mu\sigma\mathbf{A} = -\mu \mathbf{J}_{C,source} \tag{A. 52}$$

9. The Singularity Extraction Technique[50]

The singularity extraction technique facilitates numerical computation of a complex line integral if the integrand has a pole located at an infinitesimal distance from the integration path. An integral with a singular point is expressed as

$$I = \int_{z_1}^{z_2} \frac{f(z)}{(z - z_o)} dz \tag{A. 53}$$

where *f(z)* is analytic everywhere on the path of integration.

If z_o is the singular point located at an infinitesimal distance from the integration, the equation above can be re-written as

$$I = \int_{z_1}^{z_2} \frac{f(z)}{(z - z_o)} dz = \int_{z_1}^{z_2} \frac{f(z) - f(z_o)}{(z - z_o)} dz + f(z_o) \int_{z_1}^{z_2} \frac{1}{(z - z_o)} dz = I_R + I_S \tag{A. 54}$$

The first integration I_R has no singularity at z=zo and the second integration can be expressed by the following closed form equation.

$$I_S = f(z_o) \int_{z_1}^{z_2} \frac{1}{(z - z_o)} dz = f(z_o)[\ln(z_2 - z_o) - \ln(z_1 - z_o)]. \tag{A. 55}$$

Similarly, the following equation was used for the structure without ground plane.

$$I_S = f(z_o) \int_{z_1}^{z_2} \frac{1}{(z - z_o)} dz \Rightarrow \frac{1}{\varepsilon_{c0} + \varepsilon_{cb}} \int \frac{1}{|\alpha|} d\alpha \tag{A. 56}$$

10. Matrix Reduction of Equivalent Inductance for G-S-G Structure

The 3×3 inductance matrix for any 3 line configuration is given as

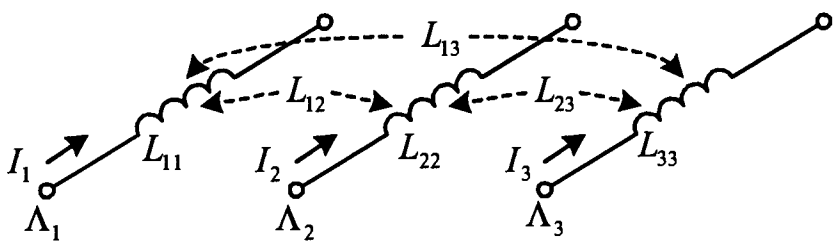

$$\begin{bmatrix}\Lambda_1\\ \Lambda_2\\ \Lambda_3\end{bmatrix}=\begin{bmatrix}L_{1,1} & L_{1,2} & L_{1,3}\\ L_{2,1} & L_{2,2} & L_{2,3}\\ L_{3,1} & L_{3,2} & L_{3,3}\end{bmatrix}\begin{bmatrix}I_1\\ I_2\\ I_3\end{bmatrix} \tag{A. 57}$$

For the G-S-G configuration, the magnetic potentials at port 1 and 3 are the same and the current of each input port has following relation.

$$I_2=-(I_1+I_3) \text{ and } \Lambda_1=\Lambda_3=\Lambda_0 \tag{A. 58}$$

The current ratio I_1 to I_3 can be readily found from the following equations.

$$\begin{aligned}\Lambda_1-\Lambda_3=0&=(L_{1,1}-L_{3,1})I_1+(L_{1,2}-L_{3,2})I_2+(L_{1,3}-L_{3,3})I_3\\ &=(L_{1,1}-L_{3,1}-L_{1,2}+L_{3,2})I_1+(L_{1,3}-L_{3,3}-L_{1,2}+L_{3,2})I_3\end{aligned}$$

$$\therefore I_1=\frac{(-L_{1,3}+L_{3,3}+L_{1,2}-L_{3,2})}{(L_{1,1}-L_{3,1}-L_{1,2}+L_{3,2})}I_3=\Delta\cdot I_3 \tag{A. 59}$$

$$\text{where } \Delta=\frac{(-L_{1,3}+L_{3,3}+L_{1,2}-L_{3,2})}{(L_{1,1}-L_{3,1}-L_{1,2}+L_{3,2})}$$

If we set the equivalent current flowing at the referenced port as I_0, all currents can be represented by this term.

$$I_1 = \frac{I_0}{(1+\Delta)}, \quad -I_2 = I_0 \qquad \text{(A. 60)}$$

$$\text{and} \quad I_3 = \frac{\Delta I_0}{(1+\Delta)}$$

By re-writing the 3×3 inductance matrix using the relations above,

$$2\Lambda_2 - (\Lambda_1 + \Lambda_3) = 2\Lambda_2 - 2\Lambda_0 = 2\Lambda_2'$$

$$2\Lambda_2' = \frac{2L_{2,1} - L_{1,1} - L_{3,1} + \Delta(2L_{2,3} - L_{1,3} - L_{3,3})}{1+\Delta} I_0 + (2L_{2,2} - L_{1,2} - L_{3,2}) I_2$$

$$\Lambda_2' = \frac{L_{1,1} + L_{3,1} - 2L_{2,1} + \Delta(L_{1,3} + L_{3,3} - 2L_{2,3}) + (1+\Delta)(2L_{2,2} - L_{1,2} - L_{3,2})}{2(1+\Delta)} \cdot I_2 \qquad \text{(A. 61)}$$

Finally, the equivalent inductance and resistance for the following circuit generated representing the G-S-G configuration becomes

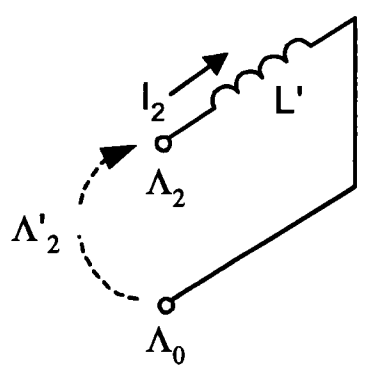

$$L' = \mathrm{Re}\left(\frac{L_{1,1} + L_{3,1} - 2L_{2,1} + \Delta(L_{1,3} + L_{3,3} - 2L_{2,3}) + (1+\Delta)(2L_{2,2} - L_{1,2} - L_{3,2})}{2(1+\Delta)} \right) \qquad \text{(A. 62)}$$

and $R' = -\omega \cdot \mathrm{Im}(L')$.

11. Derivation of ϕ-, A-Oriented Green's Function Matrix for 2 Level Metallization

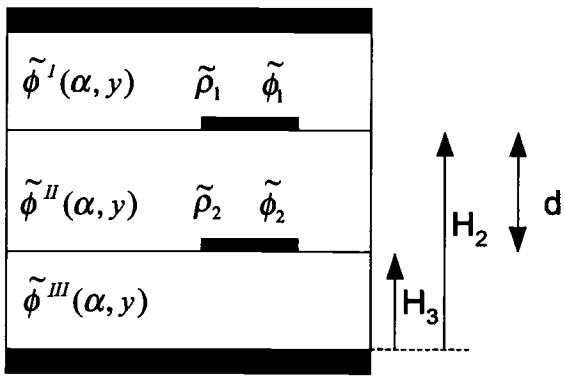

The electric potential function with unknown coefficients in each layer can be obtained as the solutions to the wave equation. The potential function in the three layers are given as

$$\tilde{\phi}^{I}(\alpha,y) = Ae^{-|\alpha|(y-H_2)} \tag{A. 63}$$

$$\tilde{\phi}^{II}(\alpha,y) = B\cdot Cosh(|\alpha|(y-H_3)) + C\cdot Sinh(|\alpha|(y-H_3)) \tag{A. 64}$$

$$\tilde{\phi}^{III}(\alpha,y) = D\cdot Cosh(|\alpha|y) + E\cdot Sinh(|\alpha|y) = E\cdot Sinh(|\alpha|y) \tag{A. 65}$$

At the interfaces the potential functions must be continuous, and the corresponding unknown coefficients C and E become

$$\tilde{\phi}^{I}(\alpha,H_2) = \tilde{\phi}^{II}(\alpha,H_2) \longrightarrow C = \frac{A - B\cdot Cosh(|\alpha|d)}{Sinh(|\alpha|d)} \tag{A. 66}$$

$$\tilde{\phi}^{II}(\alpha,H_3) = \tilde{\phi}^{III}(\alpha,H_3) \longrightarrow E = \frac{B}{Sinh(|\alpha|H_3)} \tag{A. 67}$$

conditions. For the 1st

$$\tilde{\rho}_1 = D_{n2} - D_{n1} = \alpha\left(\varepsilon_2 B \cdot Sinh(|\alpha|d) + \varepsilon_2 C \cdot Cosh(|\alpha|d) + \varepsilon_1 A\right)$$

$$= \alpha\left(\varepsilon_2 B \cdot Sinh(|\alpha|d) + \varepsilon_2 \frac{A - B \cdot Cosh(|\alpha|d)}{Sinh(|\alpha|d)} \cdot Cosh(|\alpha|d) + \varepsilon_1 A\right)$$

$$= \alpha\left(A\left[\varepsilon_1 + \varepsilon_2 \cdot Coth(|\alpha|d)\right] - B\varepsilon_2 \frac{1}{Sinh(|\alpha|d)}\right). \qquad \text{(A. 68)}$$

Similarly, the charges on the 2nd conductor become

$$\tilde{\rho}_2 = D_{n3} - D_{n2} = \alpha\left(\varepsilon_3 E \cdot Cosh(|\alpha|H_3) - \varepsilon_2 C\right)$$

$$= \alpha\left(\varepsilon_3 B \cdot Coth(|\alpha|H_3) - \varepsilon_2 \frac{A - B \cdot Cosh(|\alpha|d)}{Sinh(|\alpha|d)}\right)$$

$$= \alpha\left(-\varepsilon_2 A \frac{1}{Sinh(|\alpha|d)} + B \cdot \left[\varepsilon_3 \cdot Coth(|\alpha|H_3) + \varepsilon_2 \cdot Coth(|\alpha|d)\right]\right). \qquad \text{(A. 69)}$$

The matrix form expression in terms of the unknown coefficients A and B is

$$\begin{bmatrix} \tilde{\rho}_1 \\ \tilde{\rho}_2 \end{bmatrix} = \begin{bmatrix} \varepsilon_1 + \varepsilon_2 \cdot Coth(|\alpha|d) & -\dfrac{\varepsilon_2}{Sinh(|\alpha|d)} \\ -\dfrac{\varepsilon_2}{Sinh(|\alpha|d)} & \varepsilon_3 \cdot Coth(|\alpha|H_3) + \varepsilon_2 \cdot Coth(|\alpha|d) \end{bmatrix} \begin{bmatrix} A \\ B \end{bmatrix}. \qquad \text{(A. 70)}$$

The unknown coefficient vector can be replaced by the corresponding potentials applied to the conductors using the following relations

$$\tilde{\phi}^I(\alpha, y)\Big|_{y=H_2} = A = \tilde{\phi}_1 \qquad \text{(A. 71)}$$

$$\tilde{\phi}^{II}(\alpha,y)\Big|_{y=H_3} = B = \tilde{\phi}_2 \tag{A. 72}$$

Finally, the admittance and Green's function matrices are found as

$$\begin{bmatrix}\tilde{\rho}_1\\ \tilde{\rho}_2\end{bmatrix} = \varepsilon_o \begin{bmatrix} \varepsilon_{r1}+\varepsilon_{r2}\cdot Coth(|\alpha|d) & -\dfrac{\varepsilon_{r2}}{Sinh(|\alpha|d)} \\ -\dfrac{\varepsilon_{r2}}{Sinh(|\alpha|d)} & \varepsilon_{r3}\cdot Coth(|\alpha|H_3)+\varepsilon_{r2}\cdot Coth(|\alpha|d) \end{bmatrix} \begin{bmatrix}\tilde{\phi}_1\\ \tilde{\phi}_2\end{bmatrix} \tag{A. 73}$$

$$\downarrow$$

$$\begin{bmatrix}\tilde{\phi}_1\\ \tilde{\phi}_2\end{bmatrix} = \frac{1}{\varepsilon_o}\left[\tilde{\mathbf{G}}^{o}\right] \begin{bmatrix}\tilde{\rho}_1\\ \tilde{\rho}_2\end{bmatrix} \tag{A. 74}$$

Similarly, the magnetic potential in each medium is given as

$$\tilde{A}_z^{\,I}(\alpha,y) = Ae^{-\alpha_1(y-H_2)} \tag{A. 75}$$

$$\tilde{A}_z^{\,II}(\alpha,y) = B\cdot Cosh(\alpha_2(y-H_3)) + C\cdot Sinh(\alpha_2(y-H_3)) \tag{A. 76}$$

$$\tilde{A}_z^{\,III}(\alpha,y) = D\cdot Cosh(\alpha_3 y) + E\cdot Sinh(\alpha_3 y) = E\cdot Sinh(\alpha_3 y) \tag{A. 77}$$

The boundary conditions at each of the interfaces where the conducting strips are present are

$$\tilde{J}_{z1}(\alpha,y=H_2) = \left[\frac{1}{\mu_2}\frac{d\tilde{A}_{z2}(\alpha,y)}{dy} - \frac{1}{\mu_1}\frac{d\tilde{A}_{z1}(\alpha,y)}{dy}\right]_{y=H_2} \tag{A. 78}$$

$$\tilde{J}_{z2}(\alpha,y=H_3) = \left[\frac{1}{\mu_3}\frac{d\tilde{A}_{z3}(\alpha,y)}{dy} - \frac{1}{\mu_2}\frac{d\tilde{A}_{z2}(\alpha,y)}{dy}\right]_{y=H_3}. \tag{A. 79}$$

From the equations above, the following matrix equation is readily derived.

$$\begin{bmatrix} \tilde{J}_{z1} \\ \tilde{J}_{z2} \end{bmatrix} = \frac{1}{\mu_o} \begin{bmatrix} \alpha_1 + \alpha_2 \cdot Coth(\alpha_2 d) & -\dfrac{\alpha_2}{Sinh(\alpha_2 d)} \\ -\dfrac{\alpha_2}{Sinh(\alpha_2 d)} & \alpha_3 \cdot Coth(\alpha_3 H_3) + \alpha_2 \cdot Coth(\alpha_2 d) \end{bmatrix} \begin{bmatrix} \tilde{A}_{z1} \\ \tilde{A}_{z2} \end{bmatrix} \quad \text{(A. 80)}$$

12. Derivation of ϕ-Oriented Green's Function Matrix Including Non-Metallization Interface

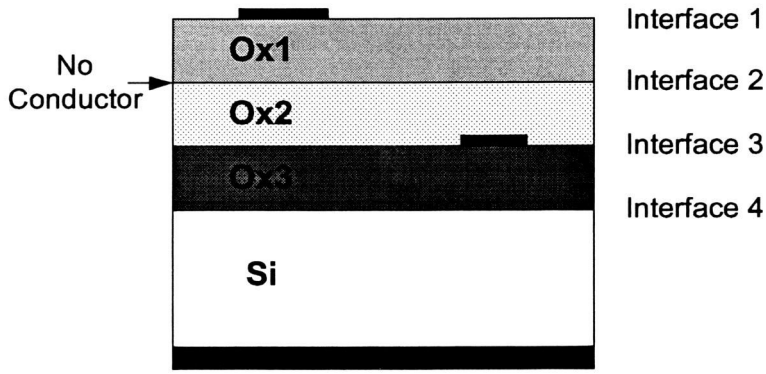

Assuming there is a conductor at the interface 2 of the figure, the normal admittance matrix for 3-level metallization is given by

$$\begin{bmatrix} \tilde{\rho}_1 \\ \tilde{\rho}_2 \\ \tilde{\rho}_3 \end{bmatrix} = \begin{bmatrix} \tilde{Y}_{1,1} & \tilde{Y}_{1,2} & 0 \\ \tilde{Y}_{2,1} & \tilde{Y}_{2,2} & \tilde{Y}_{2,3} \\ 0 & \tilde{Y}_{3,2} & \tilde{Y}_{3,3} \end{bmatrix} \begin{bmatrix} \tilde{\phi}_1 \\ \tilde{\phi}_2 \\ \tilde{\phi}_3 \end{bmatrix} \quad \text{(A. 81)}$$

Since there is no conductor at the interface 2, charge on the 2nd virtual conductor is 0. Besides, the potential at this interface does not annihilate.

$$\tilde{\rho}_2 = 0 \text{, then } \tilde{\phi}_2 = -\frac{\tilde{Y}_{2,1}}{\tilde{Y}_{2,2}} \tilde{\phi}_1 - \frac{\tilde{Y}_{2,3}}{\tilde{Y}_{2,2}} \tilde{\phi}_3 \quad \text{(A. 82)}$$

By re-writing this relation, the final admittance matrix becomes

$$\begin{bmatrix} \tilde{\rho}_1 \\ \tilde{\rho}_3 \end{bmatrix} = \begin{bmatrix} \tilde{Y}_{1,1} - \dfrac{\tilde{Y}_{2,1}^{\,2}}{\tilde{Y}_{2,2}} & -\dfrac{\tilde{Y}_{2,1}\tilde{Y}_{2,3}}{\tilde{Y}_{2,2}} \\ -\dfrac{\tilde{Y}_{2,1}\tilde{Y}_{2,3}}{\tilde{Y}_{2,2}} & \tilde{Y}_{3,3} - \dfrac{\tilde{Y}_{2,3}^{\,2}}{\tilde{Y}_{2,2}} \end{bmatrix} \begin{bmatrix} \tilde{\phi}_1 \\ \tilde{\phi}_3 \end{bmatrix} \tag{A. 83}$$

Using the similar approach, Green's matrices for other structures are readily obtained.

13. Line Parameter Extraction from Scattering or Impedance Matrix

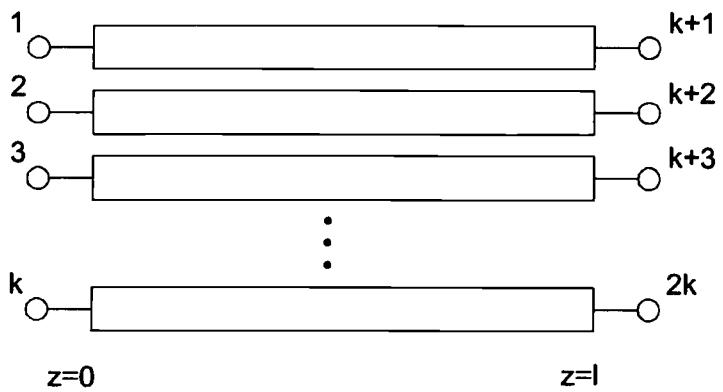

Multiple coupled transmission line system shown in the figure has the following voltage and current relations.

$$\begin{bmatrix} \mathbf{I}(z=0) \\ -\mathbf{I}(z=l) \end{bmatrix} = \begin{bmatrix} \mathbf{Y}_{11} & \mathbf{Y}_{12} \\ \mathbf{Y}_{21} & \mathbf{Y}_{22} \end{bmatrix} \begin{bmatrix} \mathbf{V}(z=0) \\ \mathbf{V}(z=l) \end{bmatrix} \tag{A. 84}$$

$$\begin{bmatrix} \mathbf{V}(z=0) \\ \mathbf{V}(z=l) \end{bmatrix} = \begin{bmatrix} \mathbf{Z}_{11} & \mathbf{Z}_{12} \\ \mathbf{Z}_{21} & \mathbf{Z}_{22} \end{bmatrix} \begin{bmatrix} \mathbf{I}(z=0) \\ -\mathbf{I}(z=l) \end{bmatrix} \tag{A. 85}$$

These linear equations can be re-established by the following form.

$$\begin{bmatrix} \mathbf{V}(z=0) \\ \mathbf{I}(z=0) \end{bmatrix} = \begin{bmatrix} Cosh([\gamma]l) & Cosh([\gamma]l)\mathbf{Z}_{\mathbf{W}} \\ \mathbf{Y}_{\mathbf{W}}Cosh([\gamma]l) & \mathbf{Y}_{\mathbf{W}}Cosh([\gamma]l)\mathbf{Z}_{\mathbf{W}} \end{bmatrix} \begin{bmatrix} \mathbf{V}(z=l) \\ \mathbf{I}(z=l) \end{bmatrix} \quad \text{(A. 86)}$$

In order to calculate the propagation constant, series and shunt distributed equivalent components per unit length, the procedures are

$$\mathbf{T} = eigenvector(\mathbf{Z}_{11}\mathbf{Y}_{11}) \quad \text{(A. 87)}$$

$$\mathbf{D} = eigenvalue(\mathbf{Z}_{11}\mathbf{Y}_{11}) \quad \text{(A. 88)}$$

where $\mathbf{Z}_{11}\mathbf{Y}_{11} = \mathbf{T} \cdot [Coth([\gamma]l)]_{diag}^{\ 2} \cdot \mathbf{T}^{-1}$, and $Coth([\gamma]l) = \sqrt{\mathbf{D}_{diag}}$.

From the equations above, propagations constants, immittance and impedance matrix can be represented as follows.

$$[\gamma] = ArcCoth(Coth([\gamma]l))/l = ArcCoth\left(\sqrt{\mathbf{D}_{diag}}\right)/l \quad \text{(A. 89)}$$

$$\mathbf{Y}_{\mathbf{W}} = \mathbf{Y}_{11}\left[\mathbf{T} \cdot Coth([\gamma]l) \cdot \mathbf{T}^{-1}\right]^{-1} \quad \text{(A. 90)}$$

$$\mathbf{Z} = \left[\mathbf{T} \cdot Coth([\gamma]l) \cdot \mathbf{T}^{-1}\right] \cdot \mathbf{Z}_{\mathbf{W}} \quad \text{(A. 91)}$$

where

$Y=Y_WT[\gamma]T^{-1}$ and $Z_W=Y_W^{-1}$.

Finally, the scattering matrix can be obtained from the linear equation as follows.

$$\mathbf{S} = (\mathbf{Z}+\mathbf{U})^{-1}(\mathbf{Z}-\mathbf{U}) \quad \text{(A. 92)}$$

14. Impedance Boundary Method of Moment(IBMOM) [38,39]

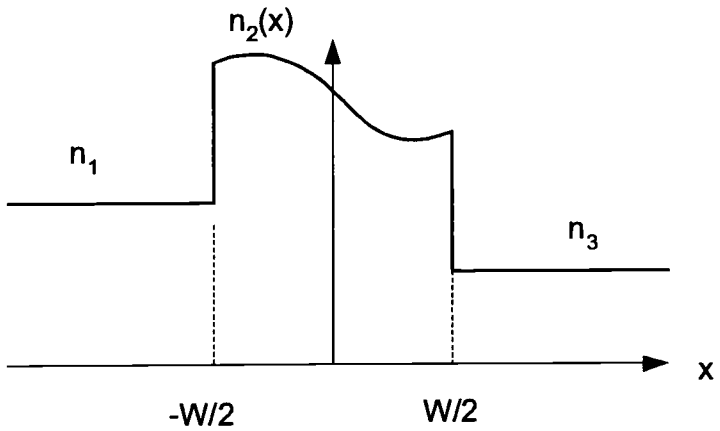

The Basis functions both for TE and TM modes for the dielectric waveguide structure are set as

$$\psi(x) = \sum_n a_n P_n(x) \quad if \quad -1 \le x \le 1 \tag{A. 93}$$

where

$$P_n(x): \text{Legendre Polynomial } P_n(x) = \frac{1}{2^n n!} \cdot \frac{d^n}{dx^n}\left(x^2 - 1\right)^n$$

By normalizing the position of interfaces, wave equation changes into

$$\left[\frac{4}{W^2}\frac{d^2}{dx^2} + k_o^2 n(x)^2 - \beta^2\right]\psi(x) = 0 \tag{A. 94}$$

In Galerkin's procedure, this equation associated with the boundary conditions is re-written by the inner product with basis functions. Finally, the wave equation is transformed into the following form.

$$\left[\beta^2 \boldsymbol{A} + \boldsymbol{B} + k_1 \boldsymbol{C} + k_3 \boldsymbol{D} - k_o^2 \boldsymbol{E}\right]\boldsymbol{a} = \boldsymbol{0} \quad \text{for TE mode} \tag{A. 95}$$

$$\left[\beta^2 \overline{\boldsymbol{A}} + \overline{\boldsymbol{B}} + k_1 \overline{\boldsymbol{C}} + k_3 \overline{\boldsymbol{D}} - k_o^2 \overline{\boldsymbol{E}}\right]\boldsymbol{a} = \boldsymbol{0} \quad \text{for TM mode} \tag{A. 96}$$

where

$$A_{i,j} = \int_{-1}^{1} P_i(x) P_j(x) dx, \qquad \overline{A}_{i,j} = \int_{-1}^{1} \frac{1}{n^2(x)} P_i(x) P_j(x) dx$$

$$B_{i,j} = \frac{4}{W^2} \int_{-1}^{1} P_i'(x) P_j'(x) dx, \qquad \overline{B}_{i,j} = \frac{4}{W^2} \int_{-1}^{1} \frac{1}{n^2(x)} P_i'(x) P_j'(x) dx$$

$$C_{i,j} = \frac{2}{W} P_i(-1) P_j(-1), \qquad \overline{C}_{i,j} = \frac{2}{n_1^2 W} P_i(-1) P_j(-1)$$

$$D_{i,j} = \frac{2}{W} P_i(1) P_j(1), \qquad \overline{D}_{i,j} = \frac{2}{n_3^2 W} P_i(1) P_j(1)$$

$$E_{i,j} = \int_{-1}^{1} n^2(x) P_i(x) P_j(x) dx, \qquad \overline{E}_{i,j} = \int_{-1}^{1} P_i(x) P_j(x) dx$$

In order for the system equation to have non-trivial solutions, root-finding procedures are carried out using the following equations.

For TE mode,

$$det\left[\boldsymbol{B} - k_o^2 \boldsymbol{E} - k_o \sqrt{n_{eff} - n_3^2}\, \boldsymbol{D} + k_o \sqrt{n_{eff} - n_1^2}\, \boldsymbol{C} + n_{eff}^2 k_o^2 \boldsymbol{A}\right] = det\left[\boldsymbol{M}(n_{eff}, \lambda_o)\right] = 0 \tag{A. 97}$$

Also, for TM mode,

$$det\left[\overline{\boldsymbol{B}} - k_o^2 \overline{\boldsymbol{E}} - k_o \sqrt{n_{eff} - n_3^2}\, \overline{\boldsymbol{D}} + k_o \sqrt{n_{eff} - n_1^2}\, \overline{\boldsymbol{C}} + n_{eff}^2 k_o^2 \overline{\boldsymbol{A}}\right] = det\left[\overline{\boldsymbol{M}}(n_{eff}, \lambda_o)\right] = 0 \tag{A. 98}$$